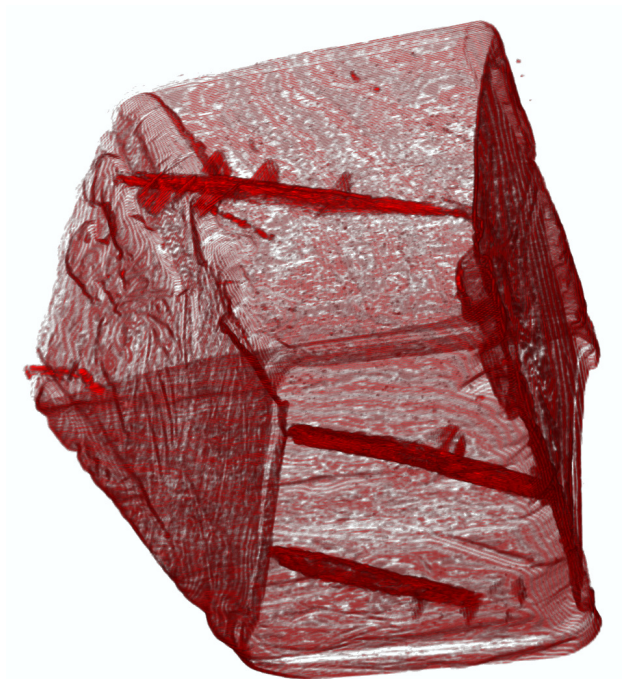Magne Syljuåsen

Experimental Investigations of the Thermomechanical Properties of Norwegian Quick Clay

Master's thesis in Geotechnology
Supervisor: Randi Kalskin Ramstad
Co-supervisor: Rao Martand Singh

June 2021

Master's thesis

NTNU
Norwegian University of
Science and Technology

Magne Syljuåsen

Experimental Investigations of the Thermomechanical Properties of Norwegian Quick Clay

Master's thesis in Geotechnology
Supervisor: Randi Kalskin Ramstad
Co-supervisor: Rao Martand Singh
June 2021

Norwegian University of Science and Technology
Faculty of Engineering
Department of Geoscience and Petroleum

NTNU
Norwegian University of
Science and Technology

Abstract

This master's thesis presents the results of experimental investigations carried out to study the effect of increased temperature on Norwegian quick clay in relation to ground source heat technology. Increased ground temperature can for example be caused by operation of a high temperature borehole thermal energy system (BTES), where excess heat is injected into an underground structure of wells with the purpose of heating the surrounding ground (creating a thermal reservoir). Thermomechanical properties of quick clay were investigated in a temperature-modified triaxial cell, and 3D images of small rectangular quick clay specimen before and after heating were obtained by micro-CT scanning. As far as the author knows, thermomechanical research on this clay type has not been previously published.

The triaxial testing temperatures were 23 and 45 °C with varying consolidation, drainage and stress level conditions. The temperature was controlled by wrapping the triaxial apparatus with a self-produced heating sleeve made of a bucket, immersion circulator, tarpaulin and water. Quick clay was found to exhibit excess volume changes and pore pressures in drained and undrained consolidation heating tests from 23 to 45 °C. This reflects on the occurrence of a thermal consolidation phenomenon which makes the specimen more compact. The compaction led to an increased peak shear strength which was measured in consecutive undrained shearing tests at 45 °C. Additionally, temperature elevated shearing at 45 °C induced a more ductile mechanical behavior. The critical state line was independent of temperature. More tests are needed to clarify the behavior of effective cohesion c' and effective frictional angle ϕ'. Overall, the results of the triaxial tests show good correlation with previous experimental research on other saturated clay types.

Temperature-induced crack generation was clearly observed by micro-CT scans of the same quick clay specimen both before and after heating to 105 °C. Pre-existing cracks were expanded and new cracks were created. New cracks had similar orientation as the pre-existing cracks. However, a differ in shape was observed, in which the new temperature-induced cracks had minor protrusions perpendicular to the main crack direction. The observed crack generation and expansion is likely caused by the temperature-induced excess pore pressure which was measured in the triaxial tests.

Sammendrag

Denne masteroppgaven presenterer resultatene av eksperimentelle undersøkelser for å studere effekten av økt temperatur på norsk kvikkleire. Økt temperatur kan for eksempel være forårsaket av drift av et høytemperatur termisk energilager (BTES) der energi tilføres brønner for å lage et termisk reservoar. Kvikkleire sine termomekaniske egenskaper ble studert i temperaturkontrollert trekasiell apparatur. Små rektangulære prøvestykker ble mikro-CT skannet før og etter oppvarming for å studere de strukturelle forskjellene. Det er ikke publisert tidligere termomekanisk forskning på denne leirtypen.

Temperaturene for treksiell testing var 23 og 45 °C. Temperaturen ble kontrollert ved å pakke inn den treksielle apparaturen med en egenprodusert oppvarmingshylse laget av en bøtte, en Sous Vide sirkulator, presenning og vann. Ved drenert og udrenert oppvarming fra 23 til 45 °C, ble det påvist en økt volumetrisk deformasjon og økt poretrykk. Dette gjenspeiler et termisk konsolideringsfenomen som gjør at kvikkleire blir mer kompakt. Kompaksjonen fører til en økt skjærstyrke som ble målt i påfølgende udrenere skjærtester ved 45 °C. I tillegg gjorde økt temperatur at kvikkleire fikk en mer duktil mekanisk oppførsel. Den kritiske tilstandslinjen (Critical state line) var uavhengig av temperatur. Det er nødvendig med flere forsøk for å karakterisere temperatureffekten på effektiv kohesjon c' og effektiv friksjonvinkel ϕ'. Resultatene fra de treaksiale testene viser generelt et godt samsvar med tidligere eksperimentelle undersøkelser på andre leirtyper.

Mikro-CT skanninger ble utført på små rektangulære prøvestykker oppvarmet til 23, 70 og 105 °C. Økt temperatur forårsaket tydelige sprekker som ble observert ved å skanne den samme kvikkleireprøven både før og etter oppvarming. De nye sprekkene hadde samme orientering som sprekkene som eksisterte før oppvarming, men med små sprekker vinkelrett på hovedsprekkeretningen. Den observerte sprekkdannelsen som følge av økt temperatur er sannsynligvis forårsaket av det økte poretrykket som ble målt i de treaksielle testene.

Preface

This master's thesis is written during the spring semester of 2021 as the final part of the master's programme in Geotechnology at the Department of Geoscience and Petroleum at the Norwegian University of Science and Technology (NTNU).

First and foremost I wish to express my gratitude to my supervisors, Associate Prof. Randi Kalskin Ramstad and Prof. Rao Martand Singh for their professional guidance and rewarding discussions. I would also like to thank staff engineers Katharina Scheidl, Ole Tore Buset, Espen Andersen and Karl Ivar Volden Kvisvik for technical support on the laboratory investigations.

Finally, I would like to express my appreciation to my girlfriend, my close friends and my family for continuous support during my studies.

Contents

List of Figures

List of Tables

List of Symbols and Abbreviations

Roman letters

a	Attraction
A_0	Initial specimen area
A_a	Specimen area during consolidation
A_s	Specimen area during shearing
c	Falling cone constant
c'	Effective cohesion
c_u	Undrained shear strength
c_{ur}	Undrained remoulded shear strength
e	Void ratio
e_0	Initial void ratio
E	Young's modulus
E_{50}	Young's modulus at 50 % of peak shear strength
g	Gravitational acceleration constant = 9.81 m/s^2
I_L	Liquidity index
I_P	Plasticity index
K'_0	Effective at rest coefficient
M	Slope of critical state line
n	Porosity
p'	Effective mean stress
P	Vertical required load
q	Deviatoric stress
S_t	Sensitivity
S_r	Degree of saturation
T	Temperature

T_0	Initial temperature
T_s	Temperature of specimen
ΔT	Change in temperature
u	Pore pressure
u_0	Initial pore pressure
Δu	Excess pore pressure
V_0	Initial specimen volume
V_w	Volume of pore water
V_s	Volume of solids
ΔV	Volume of drained pore water
ΔV_0	Volume of drained pore water of a metallic specimen
ΔV_{corr}	Corrected volume of drained pore water
w	Water content
w_L	Liquid limit
w_P	Plasticity limit
w_S	Shrinkage limit
z	Depth below surface terrain

Greek letters

α	Thermal expansion coefficient
α_w	Thermal expansion coefficient of water
α_s	Thermal expansion coefficient of solid particles
β	Falling cone tip angle
γ	Unit weight of soil

γ_a	Average unit weight of soil	σ_2	Intermediate principal stress
γ_s	Unit weight of solids	σ_3	Minimum principal stress
γ_w	Unit weight of water	τ	Shear stress
ε_a	Axial strain	ϕ'	Effective frictional angle
ε_{a_f}	Axial strain at failure	ϕ'_{cs}	Effective frictional angle at critical state
ε_v	Volumetric strain		
ε_v^T	Thermal volumetric strain	λ, Γ	CSL constants
ν	Specific volume	**Abbreviations**	
ρ	Density	BTES	Borehole Thermal Energy Storage
ρ_a	Average density		
ρ_s	Density of solid particles	CT	Computer Tomography
σ	Total stress	CAU_C	Consolidated Anisotropic Undrained Compression
σ_a	Axial confining stress		
σ_c	Cell pressure	CIU_C	Consolidated Isotropic Undrained Compression
σ_p	Preconsolidation pressure	CSL	Critical state line
σ_r	Radial confining stress	DD	Dødens dal
σ'	Effective stress	IJM	ImageJ Macro Language
σ'_h	Effective horizontal stress	NC	Normally Consolidated
σ'_n	Effective normal stress	NTNU	Norwegian University of Science and Technology
σ'_v	Effective vertical stress	OC	Overconsolidated
σ_1	Maximum principal stress	OCR	Overconsolidation ratio
		R.T.	Room temperature

Chapter 1

Introduction

1.1 Background

The increased use of ground source heat extraction and energy storage systems in Norway have raised questions on how such installations affect the surrounding ground. Quick clay areas are of special concern in light of the disastrous quick clay landslide in Gjerdrum, Norway in December 2020. This thesis investigates how the mechanical properties of Norwegian quick clay are affected by an increase in temperature. Increased ground temperature can for example be caused by operation of a high temperature borehole thermal energy system (BTES), where excess heat is injected into an underground structure of wells with the purpose of heating the surrounding ground (creating a thermal reservoir). The first Norwegian high temperature BTES was recently built with planned temperatures up to 50 - 60 °C (Ramstad et al., 2017). With increasing focus on global climate and environmental challenges, such systems are expected to be even more important in the future. For safe design of BTES in quick clay areas, it is crucial to estimate the respective thermomechanical properties. Understanding the thermomechanical behavior of quick clay can also be important in other engineering applications such as radioactive waste disposal, burying high-voltage cables, pavement engineering and landfill cover systems (Wang et al., 2020).

As far as the author knows, no previous research on the thermomechanical behavior of Norwegian quick clay have been published. In contrast, the thermomechanical behavior of other saturated clays have been widely studied since the initial research efforts by Campanella & Mitchell (1968); Plum & Esrig (1969). A large number of experimental studies have examined the effect of temperature on natural and artificial clays up to 100 °C, mostly in relation to radioactive waste disposal applications (e.g. Houston et al., 1985; Baldi et al., 1988; Hueckel & Pellegrini, 1991; Towhata et al., 1993; Del Olmo et al., 1996; Graham et al., 2001; Cekerevac & Laloui, 2004; Abuel-Naga, 2006). These studies exhibited that an increase in temperature affects the volume change, shear strength, pore pressure and stiffness. The methodologies of these studies can be addressed to the experimental investigations of Norwegian quick clay. Moreover, newer thermomechanical research have been concentrated on developing various constitutive models in the context of elastoplasticity and critical state theory based on experimental results (e.g. Abuel-Naga, 2006; Laloui & François, 2009; Yao & Zhou, 2013; Wang et al., 2016; Xiong et al., 2016; Ashrafi & Hamidi, 2020; Cheng et al., 2020).

1.2 Aim

The overall goal of this master's thesis work is to obtain knowledge on how increased temperature affects the thermomechanical properties of Norwegian quick clay. Only the effects of temperatures up to the boiling point of water (100 °C) are studied for practical relevance to engineering applications. More specifically, this comprises how the following properties change with elevated temperatures:

- Volumetric deformation ε_v

- Pore pressure u

- Shear strength τ, effective cohesion c' and effective frictional angle ϕ'

- Critical state line (CSL) inclination M

- Stress-strain behavior

- Young's modulus E

1.3 Objectives

To achieve the goal of this master's thesis, the following actions need to be taken:

- Develop and construct a temperature-modified triaxial cell

- Carry out drained and undrained heating consolidation tests for investigation of thermally-induced volumetric deformation and pore pressure

- Conduct undrained and drained shearing at various temperatures for measurement of shear strength τ, effective cohesion c', effective frictional angle ϕ', CSL inclination M, Young's modulus E and stress-strain behavior

- Perform micro-CT scans before and after heating to visualize the temperature effect on the internal structural changes

1.4 Outline

This master's thesis is organized into three parts:

I **A literature review** of previous research on the thermomechanical behavior of saturated clays and the material properties of quick clay. The thermomechanical literature concerns other saturated clays since there are no previously published investigations on quick clay. Saturated clays with properties close to quick clay, such as the Bangkok clay, are emphasized.

II **Methodology** of the conducted experimental research. This comprises detailed procedure descriptions of temperature-modified triaxial testing, micro-CT scans and index tests.

III **Results** of the laboratory investigations. This includes graphical presentations of the change in properties during triaxial testing, 3D images of quick clay before/after heating and the outcome of index tests. Ultimately, the results are discussed in light of the findings from the literature review.

Part I

Literature review

Chapter 2

Quick clay

This chapter presents a description of the formation and geotechnical definition of Norwegian quick clay. Quick clay is a sensitive marine clay which is found below the marine level (the present elevation of where the sea level was at end of the last ice age). The marine level varies between 0 and 222 meter above the present sea level.

2.1   Formation

About 20 000 years ago the Scandinavian peninsula was covered by a 3000 meter thick ice sheet (Bryhni & Hagen, 2020). When the ice started to melt, glacial rivers carried loose material away. The coarsest loose material (sand, gravel, rock and boulder) was deposited closest to the glacier while the finer material (silt and clay) was deposited farther away. Clay mineral particles ($< 2\,\mu m$) are too fine to sedimentate in running and steady water, and were thus carried in suspension all the way to the ocean.

Clay particles are always negatively charged because of isomorphic substitution in the lattice (e.g. $Si^{4+} \rightarrow Al^{3+}$) and pH dependent charges (Brattli, 2018). To compensate for this permanent negative charge, Na^+ ions in the saline water were drawn to the surface of the clay particles. This facilitated flocculation, in which clay particles stuck together in a stable card-house structure. When the floc became large enough, it sunk to the ocean floor and was deposited as marine clay.

As the ice melted, the ice sheet lost its weight, and post-glacial rebound started. Deposits of marine clay were lifted above the present sea level. In specific geological conditions, where fresh water flows through marine clay, Na^+ ions are washed out over time. The clay particle-bindings become weakened and forms a highly unstable structure. Such leached marine clay is called quick clay. The structural difference between marine clay and quick clay is illustrated in Figure 2.1. Overloading of quick clay can lead to a sudden collapse of the structure, whereas particles start to float in their own porewater.

(I) Marine clay with saline porewater: Large attractive forces between particle edges and planes. Small repulsive forces between particle planes. The structure is stable.

(II) Quick clay (Na$^+$-ions are washed out): Small attractive forces between particle edges and planes. Larger repulsive forces between particle planes. The structure is unstable.

FIGURE 2.1: Card-house structure of marine and quick clay.

2.2 Geotechnical definition

Clay refers to a naturally occuring sediment with at least 30 % grains < 2 µm. In Norway, quick clay is defined as a special type of marine clay with undrained remoulded shear strength c_{ur} < 0.5 kPa. Also, it is characterized with a sensitivity S_t higher than 50 and a salinity below 0.5 % (seawater has a salinity of 3.5 %). Sensitivity is the ratio between the undisturbed shear strength c_u and the remoulded shear strength c_{ur}. Figure 2.2 shows a typical stress-strain response curve of quick clay. At failure, it experiences a sudden loss of the ultimate undrained shear strength.
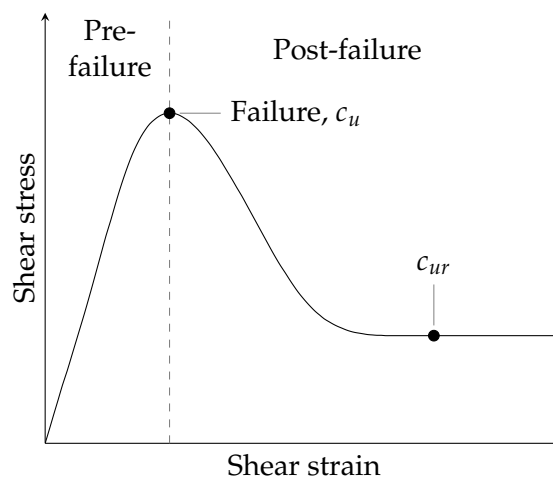
FIGURE 2.2: Stress-strain response of quick clay. c_u is the undisturbed shear strength and c_{ur} is the remoulded shear strength.

Similar to other soils, quick clay is a three-phase-material containing solid particles and voids filled with water or air. Quick clay becomes liquid after stirring meaning that the water content w > liquid limit w_L. The liquid limit is the water content at which the soil changes state from plastic to liquid.

Chapter 3

Thermomechanical behavior of saturated clay

Extensive laboratory investigations on the thermomechanical behavior of many clay types have been carried out by various researchers, but no previous investigations on quick clay have been published. Therefore, this chapter concerns other saturated clays, but with emphasis on clay types with properties close to quick clay such as the Bangkok clay. Understanding the thermomechanical behavior of clay is important in engineering applications such as ground source heat technology, radioactive waste disposal, burying high-voltage cables, pavement engineering and landfill cover systems (Wang et al., 2020).

3.1   Thermal consolidation

Like most natural materials, the main components in clay (solid particles and water) expand during heating (Li, 2019). The magnitude of this expansion can be deduced from the coefficient of thermal expansion α which is the volumetric strain taking place per degree change in temperature at a constant pressure. The thermal expansion coefficient for water α_w is much higher than the thermal expansion coefficient for solid particles α_s (see Table 3.1). Consequently, water expands more than solid particles which generates an excess pore pressure Δu. Similar to classical consolidation theory, the excess pore pressure facilitates pore water drainage as time elapses. Drainage reduces the pore pressure and parts of the excess total stress is transferred to the solid particles. Thus, the effective stress σ' is increased (Terzaghi's principle). The increase in effective stress compresses the clay skeleton. This compression is called thermal consolidation (Plum & Esrig, 1969). Also, a secondary thermal compression occurs due to rearrangement of the soil fabric because of weakened interparticle shearing resistance at elevated temperatures (Houston et al., 1985). This process does not require a water pressure gradient as a driving force.

	Thermal expansion coefficient [$\times 10^{-5}$ °C^{-1}]
Water	20.7
Solid particles	1.5 - 5.0

TABLE 3.1: Thermal expansion coefficients at 20 °C. Modified from Li (2019).

Because of the fact that thermal consolidation origins from a change in pore pressure, experimental laboratory research have been divided into two categories:

1. Drained tests where pore pressures can dissipate

2. Undrained tests where pore pressures can build up

Previous laboratory investigations have been carried out in temperature-modified oedometer or triaxial apparatus. Only the triaxial apparatus was used in this thesis method work. Figure 3.1 shows a schematic of the modified triaxial apparatus used by Cekerevac & Laloui (2004), where circulated hot water was used to control the temperature within the cell. In such apparatuses, complex mechanical/temperature loading paths in undrained/drained conditions can be carried out which facilitates measurements of the thermomechanical properties.
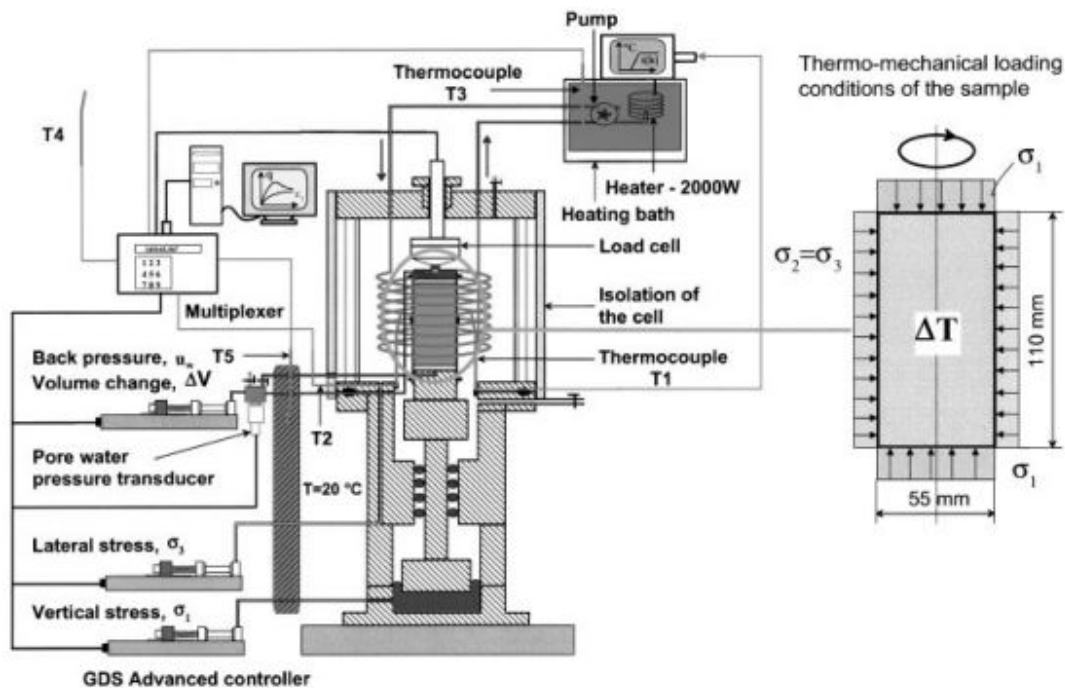
FIGURE 3.1: Temperature-controlled triaxial apparatus utilizing water which is heated and circulated by a bath heater. Thermocouples inside and outside the cell controls the temperature. Modified from Cekerevac & Laloui (2004).

Thermal strain ε_v^T is the volumetric deformation caused by temperature-induced pore pressures and can be measured in drained heating tests. Drained heating tests is carried out in modified temperature-controlled triaxial cells with open drainage lines. Heating rates should be low enough to avoid excess pore pressure development. In standard isothermal triaxial tests the volumetric deformation is calculated as $\varepsilon_v = \Delta V / V_0$ where ΔV is the volume of water expelled from the specimen through the drainage lines and V_0 is the specimen volume (NTNU Geotechnical division, 2017). However, this is no longer valid in thermal tests due to the thermal expansion of drainage system and clay specimen (Abuel-Naga, 2006).

In order to correct for thermal expansion of the drainage system, a calibration test can be conducted on a metallic specimen. In a such test, the metallic specimen is heated incrementally (with similar heating conditions as for the clay specimen) and the amount of water expelled is recorded as V_0. Campanella & Mitchell (1968)

8

showed that by subtracting the effect of thermal expansion of the two clay components (solid particles and water) from the total volume of drained pore water $\Delta V_{\mathrm{corr}} = \Delta V - \Delta V_0$, the thermal strain $\varepsilon_\mathrm{v}{}^\mathrm{T}$ becomes:

$$\varepsilon_\mathrm{v}{}^\mathrm{T} = \frac{\Delta V_{\mathrm{corr}} - (\alpha_w V_w + \alpha_s V_s)\Delta T}{V_0} \tag{3.1}$$

where α_w is the thermal coefficient of pore water, V_w is the volume of pore water, α_s is the thermal coefficient of solid particles, V_s is the volume of solid particles and V_0 is the specimen volume.

The effects on thermal strain $\varepsilon_\mathrm{v}{}^\mathrm{T}$ by plasticity, stress history and stress level is discussed in the following.

Effect of soil plasticity

Several researchers (Demars & Charles, 1982; Towhata et al., 1993; Robinet et al., 1996; Del Olmo et al., 1996; Graham et al., 2001; Laloui & Cekerevac, 2003; Abuel-Naga, 2006; Di Donna & Laloui, 2015) have addressed the amount of thermal strain $\varepsilon_\mathrm{v}{}^\mathrm{T}$ to the temperature-induced change in physico-chemical properties of clay. The physico-chemical properties depend on the clay lattice constitution, the chemical composition of the pore fluid and interlayer distance. It is thought that the clay plasticity index I_P can be used as an indicator to the intensity of the physico-chemical interactions upon heating. Figure 3.2 shows that the thermally-induced volume change increases as the clay plasticity increases.
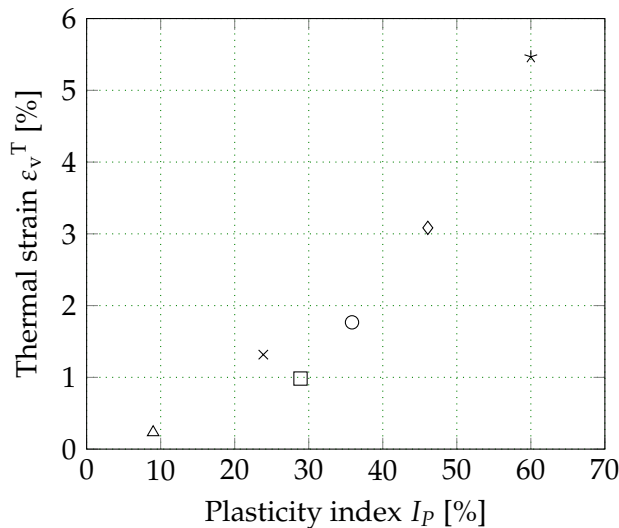
FIGURE 3.2: Plasticity index of soil and temperature induced volumetric strain of some normally consolidated clays reported in literature ($\Delta T \approx 70\,°C$ and $T_0 \approx 20\,°C$). Modified from Abuel-Naga (2006).

Effect of stress history

Plum & Esrig (1969) showed that the volume change of a specimen subjected to an increase in temperature is dependent on its overconsolidation ratio (OCR). OCR is the ratio between the preconsolidation pressure (maximum effective vertical overburden stress) σ_p and current effective stress σ'_v. Among others, Sultan et al. (2002) and Cekerevac & Laloui (2004) carried out temperature-controlled triaxial tests on Kaolin and Boom clay specimen subjected to thermal loads (22 - 90 °C and 22 - 100 °C) at different overconsolidation ratios. As seen in Figure 3.3, the thermal volumetric strain evolution is dependent on the stress history. Upon heating, normally consolidated (NC) specimen contracts, lightly overconsolidated specimen contracts less compared to NC specimen while the highly overconsolidated (OC) specimen expands. For overconsolidated specimen, the specific temperature where the deformation behavior changes from expansion to contraction is dependent on the OCR. The shape of the graphs show that thermal expansion is reversible and thermal contraction is irreversible (Sultan et al., 2002).
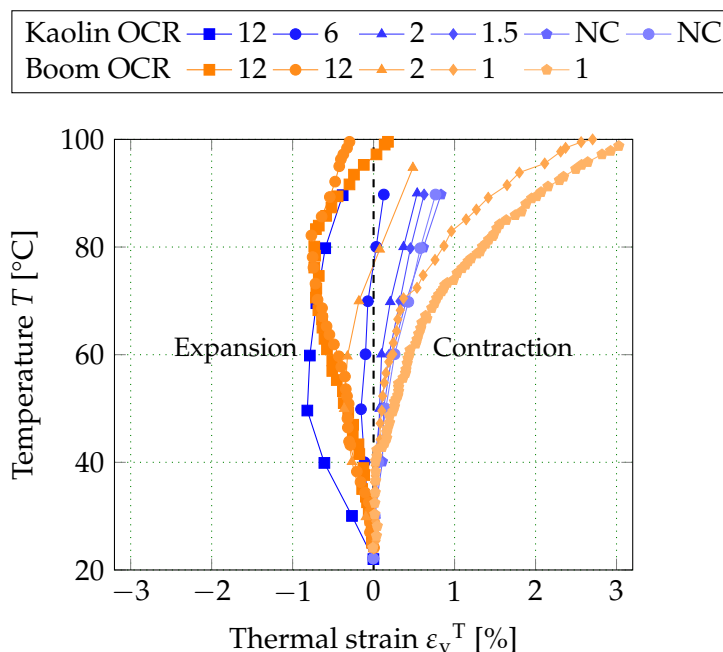
FIGURE 3.3: Thermal strain ε_v^T of Kaolin and Boom clay in drained heating tests with incremental thermal loads (22 - 90 °C and 22 - 100 °C) at different overconsolidation ratios (OCR). Modified from Sultan et al. (2002) and Cekerevac & Laloui (2004).

Effect of stress level

Towhata et al. (1993) studied the effect of stress level on the change in void ratio of normally consolidated clay in a temperature-controlled oedometer cell. Void ratio e is the ratio between volume of voids (open spaces) and volume of solids. Figure 3.4 shows that the thermal volume contraction of normally consolidated artificial MC clay specimen follows similar curves despite the difference in applied load. According to Towhata et al. (1993), the specimen loaded to 40 kPa was more vulnerable to volume contraction due to the low stress causing the specimen to behave similar to slurry.
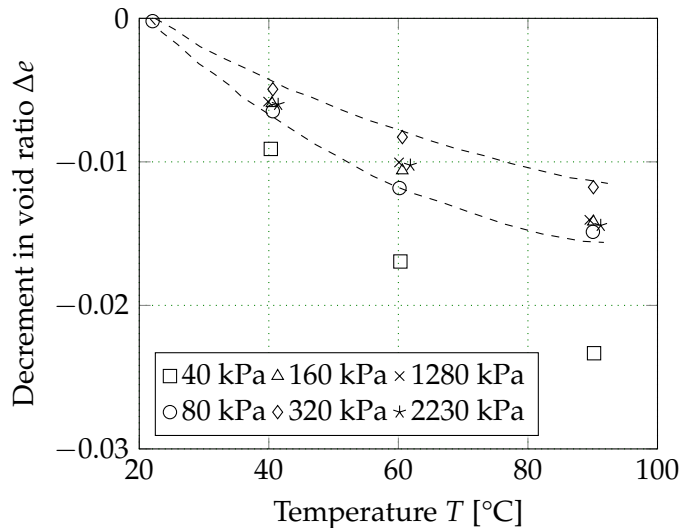
FIGURE 3.4: Decrement of void ratio due to heating of normally consolidated MC clay specimen. Modified from Towhata et al. (1993).

3.2 Pore pressure generation

As previously discussed, saturated clay develop excess pore pressures because of the differential expansion of pore water and clay solids. This phenomenon have been studied by many researchers (Campanella & Mitchell, 1968; Plum & Esrig, 1969; Houston et al., 1985; Burghignoli et al., 2000; Moritz & Gabrielsson, 2001; Abuel-Naga et al., 2007). Contrary to thermal strain measurements, pore pressure measurements demand closed drainage lines during incremental heating (undrained conditions). Figure 3.5 shows temperature-induced pore pressure changes for 10 clay specimen reported in literature.
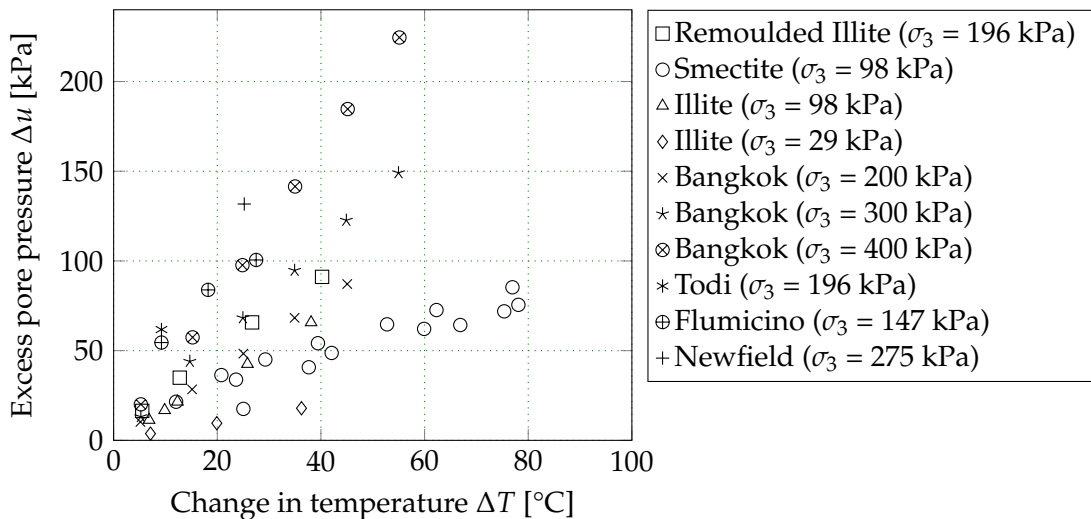
FIGURE 3.5: Effect of temperature change on the change in pore water pressure for soil specimen. See Appendix A, Table A.1 for index properties. Modified from Ghaaowd et al. (2015).

The excess pore pressure Δu increases with increased increment in temperature. However, similar clays subjected to different isotropic consolidation stress level show

11

unlike behavior. This indicates that pore pressure is dependent on the applied consolidation stress. According to Houston et al. (1985), the stiffness of the clay skeleton is expected to increase by an increased stress level which may affect the pore pressure generation.

3.3 Shear strength

Previous experimental research show dissimilar shear strength behavior with elevated temperatures. An increase in shear strength with increased temperatures was measured by Kuntiwattanakul et al. (1995); Cekerevac & Laloui (2004); Abuel-Naga (2006). Contrary, a reduction in shear strength with elevated temperatures was reported by Moritz (1995); Hueckel & Borsetto (1990); Ghahremannejad (2003). Also, there are studies reporting no temperature effect on shear strength (Towhata et al., 1993; Burghignoli et al., 2000; Graham et al., 2001; Cekerevac & Laloui, 2004).

Abuel-Naga (2006) investigated the undrained shear strength behavior of Bangkok clay. These results are emphasized since Bangkok clay is of marine origin and has properties close to quick clay. Figure 3.6 shows the results of undrained shearing in temperature elevated triaxial tests of isotropic normally consolidated Bangkok clay to 200 kPa. It is seen that the peak deviatoric stress increases with elevated temperature. When the temperature of normally consolidated clay is increased, more thermal consolidation occur which raises the peak shear strength. The measured pore pressures during undrained temperature-elevated shearing was lower with increased temperatures. This can be explained by the thermal consolidation phenomenon in which incremental drained heating to higher temperatures have led to more dissipation of pore pressure (higher degree of thermal consolidation) than for lower temperatures.
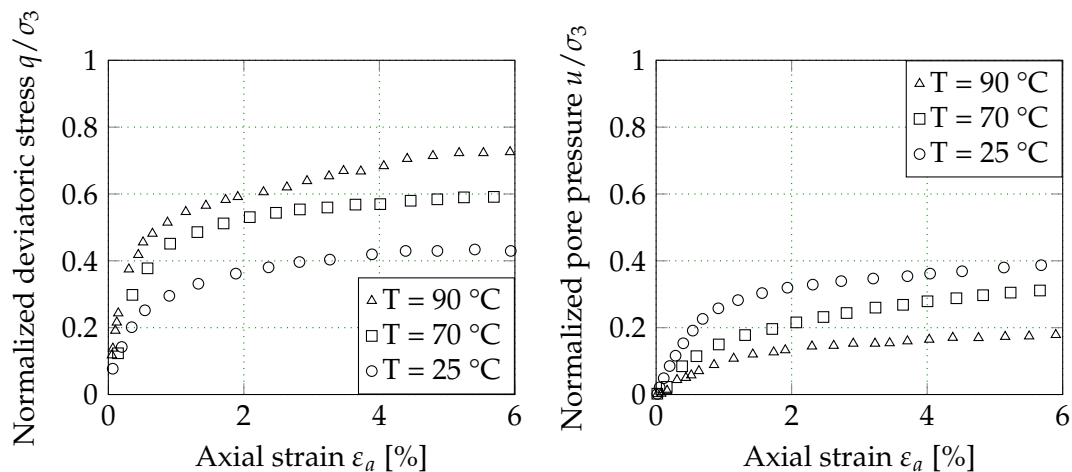
FIGURE 3.6: Undrained shearing of soft Bangkok clay at elevated temperatures. Modified from Abuel-Naga (2006).

The results of drained shearing tests on isotropic normally consolidated Bangkok clay to 300 kPa are shown in Figure 3.7. Similar to undrained test results, specimen sheared at higher temperatures gave higher peak deviatoric stress. At large strains, all curves diverge to the residual deviatoric stress which is independent of temperature. A residual deviatoric stress independency of temperature was also reported by Cekerevac & Laloui (2004); Trani et al. (2010). The shape of the stress-strain curves

indicate that specimen sheared at high temperatures show strain softening behavior, while the specimen at room temperature have stress hardening behavior.
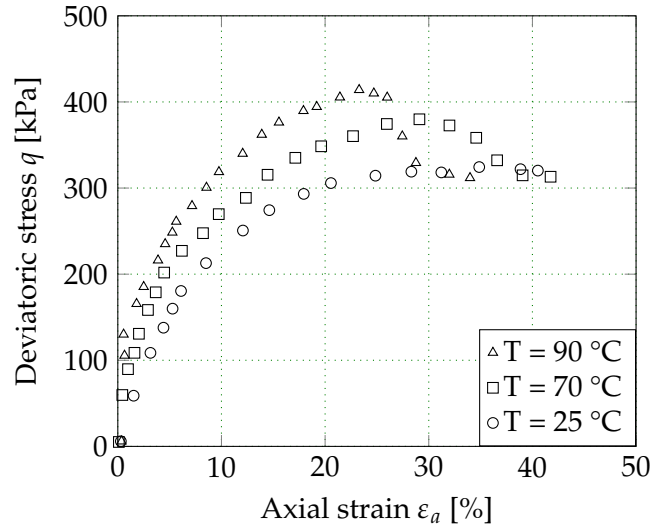
FIGURE 3.7: Drained shearing of soft Bangkok clay at elevated temperatures. Modified from Abuel-Naga (2006).

Critical state line (CSL)

The critical state concept is an idealization of the behavior of saturated clays in triaxial compression tests (Schofield & Wroth, 1968). It states that soils will come into a critical state, in which there is no change in mean effective stress $p' = \frac{1}{3}(\sigma_1' + 2\sigma_3')$, deviatoric stress $q = \sigma_1 - \sigma_3$ and specific volume $v = 1 + e$. Mathematically this is:

$$\frac{\partial p'}{\partial \varepsilon_s} = \frac{\partial q}{\partial \varepsilon_s} = \frac{\partial v}{\partial \varepsilon_s} = 0 \tag{3.2}$$

All critical states for a soil, form a unique line called the Critial State Line (CSL) defined by the following equations in the space (p', q, v):

$$q = Mp' \tag{3.3} \qquad\qquad v = \Gamma - \lambda \ln p' \tag{3.4}$$

where M, Γ and λ are soil constants.

The inclination of the critical state line M can be obtained from a $p' - q$ plot of undrained or drained triaxial test results. M can be related to the frictional angle at critical state ϕ_{cs}' by the following Equation (valid for compression tests):

$$M = \frac{6\sin\phi_{cs}'}{3 - \sin\phi_{cs}'} \tag{3.5}$$

Previous research have concluded that the slope of the critical state line M is temperature independent as shown in Figure 3.8 and 3.9. Cekerevac & Laloui (2004) suggested that the friction angle might be influenced by temperature change by plotting in the (p', v) space.
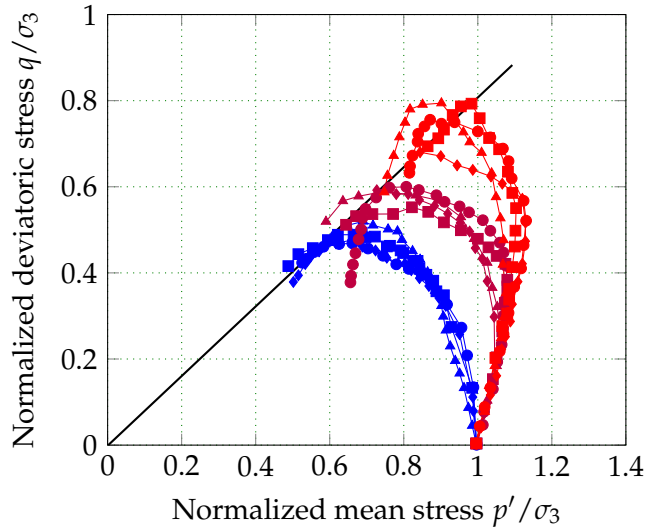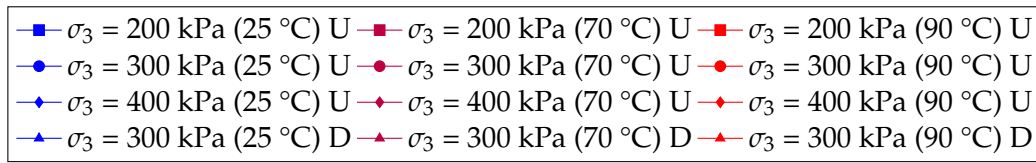
FIGURE 3.8: Normalized shear strength under different temperature. The critical state line (CSL) is shown in black. U = Undrained conditions and D = Drained conditions. Modified from Abuel-Naga (2006).
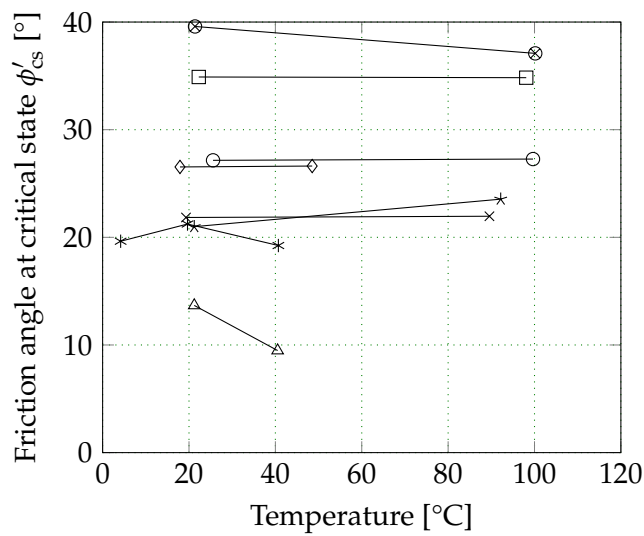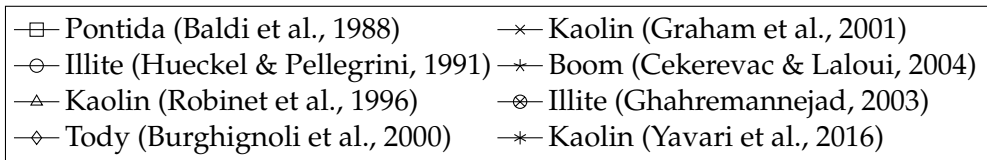
FIGURE 3.9: Change in frictional angle at critical state ϕ'_{cs} with temperature for some clay types reported in literature. Modified from (Wang et al., 2020).

14

Young's modulus

The Young's modulus E is a constant which expresses the stiffness of the clay. It can be derived from the linear part of stress-strain curves obtained in triaxial tests. A common approach is to measure the modulus at half of the peak shear strength. Previous research have shown that E is dependent on temperature (Kuntiwattanakul et al., 1995; Cekerevac & Laloui, 2004; Abuel-Naga, 2006). Abuel-Naga (2006) showed that the undrained Young's modulus increased as the temperature increased.

Part II

Methodology

Chapter 4

Sampling, subdivision and index testing

Detailed descriptions of the methodology of sampling, subdivision and index testing are given in this chapter. Quick clay sampling was carried out by the Geotechnical Division of NTNU using a modified Sherbrooke sampler. Sample subdivision and index testing was performed by the author at the NTNU soil mechanics laboratory.

4.1 Sampling

Quick clay samples were gathered using the mini-block sampler (see Figure 4.1) developed at the Geotechnical Division of NTNU (Emdal et al., 2016). The mini-block sampler is a modified Sherbrooke sampler, in which the main modification is a reduction of the outer diameter to 230 mm. This diameter makes it possible to carve out mini-block samples with a diameter of up to 160 mm. The maximum sample height is 300 mm, but the actual sample length is dependent on the soil strength. The mini-block sampler uses three cutting blades combined with water pressure to excavate an annulus around a block of the soil. Pressurized water exits through openings in the cutting blades which facilitates cutting and stabilizes the borehole wall. When the full length of the annulus is excavated, three horizontal torque spring activated bottom cutters are released by a drop weight.

| (I) | (II) |
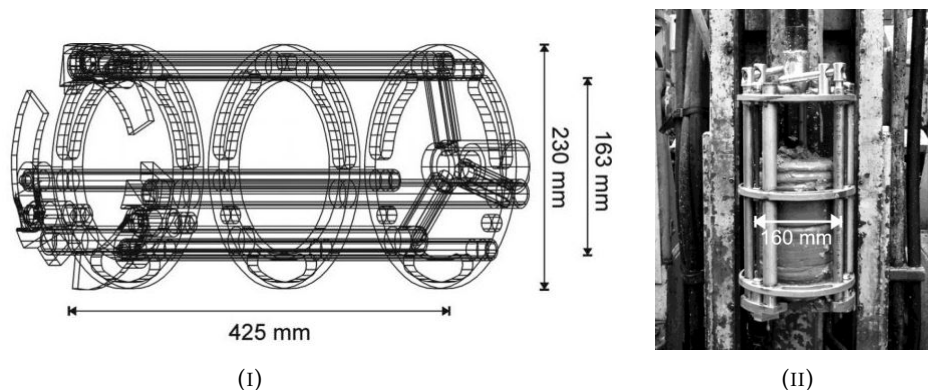
FIGURE 4.1: Mini-block sampler developed at NTNU. (I) Technical drawing of the sampler (rotated 90°). (II) Photo of the sampler in use. Modified from Emdal et al. (2016).

Once the sample is brought to the surface, it is placed on a custom made base. To prevent loss of moisture, it is quickly wrapped in layers of plastic foil and duct tape.

The custom made base containing the sample is put in a PVC tube filled with sty-rofoam balls for transportation. Samples are stored in a cold room at an average temperature of 5 °C at the NTNU soil mechanics laboratory.

(I)   (II)

FIGURE 4.2: Sample protection and transportation. (I) PVC tubes for transport. (II) Transport tube containing sample and styrofoam balls. Modified from (Emdal et al., 2016).

Mini-block samples from Dødens dal

The borehole for mini-block sampling was drilled in Dødens dal, Trondheim, in central Norway (see Figure 4.3 (I)). The drilling was performed by the Geotechnical Division of NTNU and the exact location of the borehole is not known to the author. Dødens dal is a valley located next to the NTNU Gløshaugen campus. The valley contains a football field, sandvolleyball courts and every second year the valley is transformed into a concert arena for the UKA culture festival. In 2011, it was planned to expand the sports facilities but the detection of quick clay combined with steep hillsides stopped it. As seen in the geological map of superficial deposits, in Figure 4.3 (II), the site consists of marine deposits.

(I)   (II)
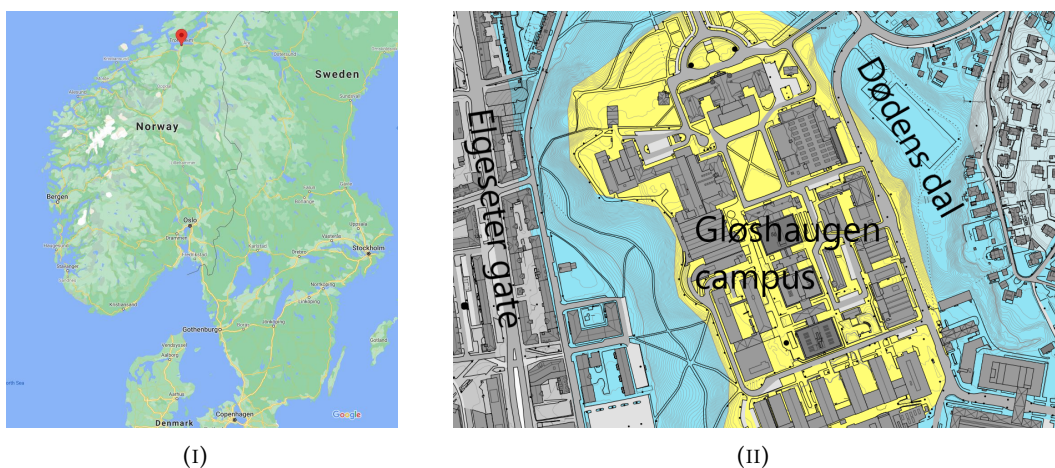
FIGURE 4.3: Maps of the site location. (I) The city of Trondheim located in central Norway. (II) Geological map of superficial deposits in the area surrounding the sampling site Dødens dal. Blue color represents marine deposits, while yellow color indicates fluvial deposits. Modified from Geological Survey of Norway (`https://geo.ngu.no/kart/losmasse/`).

4.2 Opening and subdivision

The mini-block samples were named chronologically according to the opening date and sample location ("DD" for Dødens dal). An overview of the sampling and storage properties is shown in Table 4.1.

TABLE 4.1: Overview of sampling and storage properties of the mini-block samples.

Sample ID	Depth [m]	Sampling date [dd.mm.yy]	Storage length [days]	Opening date [dd.mm.yy]	Storage Temperature [°C]
DD-1	7.45 - 7.80	27.02.2020	361	22.02.2021	5
DD-2	5.70 - 6.05	20.02.2020	417	12.04.2021	5
DD-3	6.40 - 6.75	27.02.2020	437	19.04.2021	5

To begin the opening and subdivision procedure, each sample was carried from the cold room to the laboratory, unpacked from the PVC tube and duct tape was removed by a knife. Then, the sample was placed in a trimming device and subdivided into cylindrical slices using a wire saw. A few drops of silicone were added to the top horizontal plane of the trimming device to reduce friction when the extracted slice was slid over. This process is shown in Figure 4.5. The appropriate height and amount of cylindrical slices were selected according to the two different subdivision schemes illustrated in Figure 4.4. DD-1 was subdivided as in Figure 4.4 (I) while DD-2 & DD-3 were subdivided as in Figure 4.4 (II).
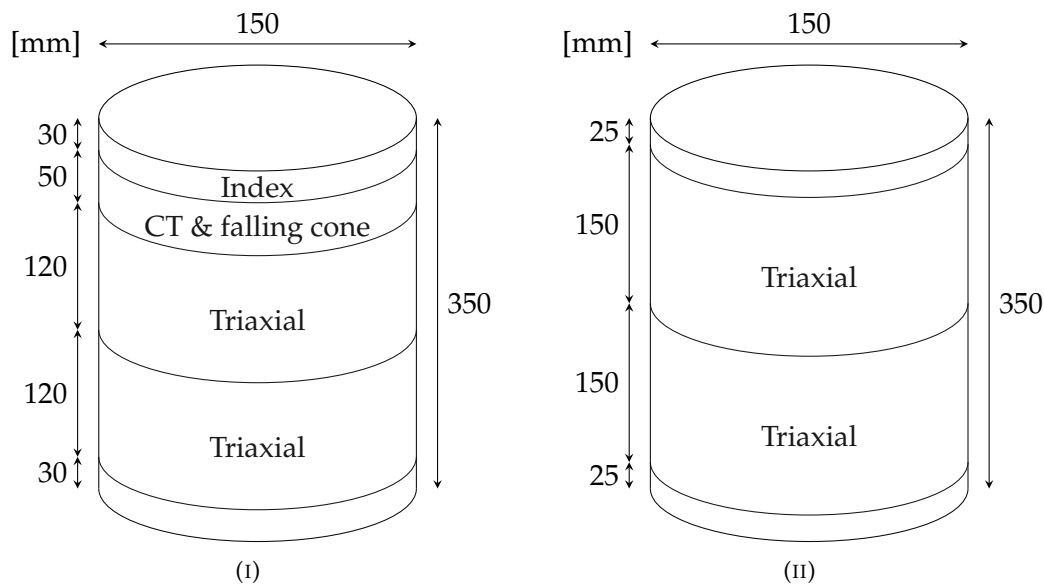
FIGURE 4.4: Subdivision schemes of mini-block sample DD-1 (I) and DD-2 & DD-3 (II).

The general clay characteristics were determined from the top part of DD-1. The slice for micro-CT scan (CT) & falling cone tests was further subdivided into four cubes as shown in Figure 4.6. Half of these cubes were used for falling cone tests, while the other half was dedicated to micro-CT specimen preparation.

(I) DD-2 before opening.   (II) Full view of DD-2.   (III) Trimming device.

(IV) Removal of the top cap.   (V) Cutting the bottom slice.   (VI) The extracted bottom slice.

FIGURE 4.5: General opening and trimming procedure of a mini-block sample into cylindrical slices.
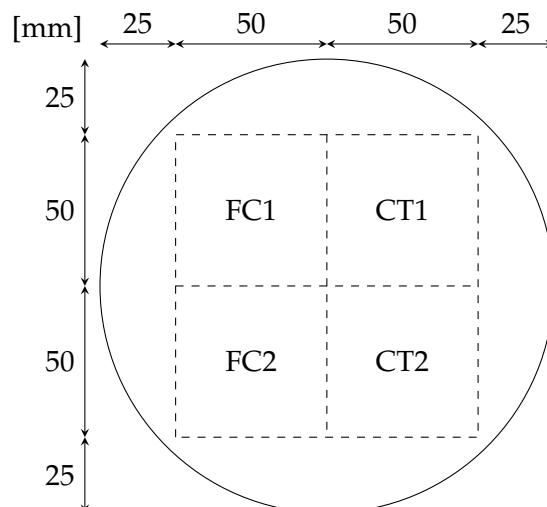
FIGURE 4.6: Subdivision of the slice for falling cone tests (FC1 and FC2) and micro-CT scan (CT1 and CT2). The slice was divided into four cubes with dimension $50 \times 50 \times 50$ mm^3.

The triaxial test slices were subdivided as shown in Figure 4.7. Each slice was divided into four quarter pieces and further trimmed down to a cylindrical triaxial specimen with diameter = 54 mm. Lastly, the ends were cut off in a crib so the sample height was 100 mm.

| (I) | (II) | (III) | (IV) |
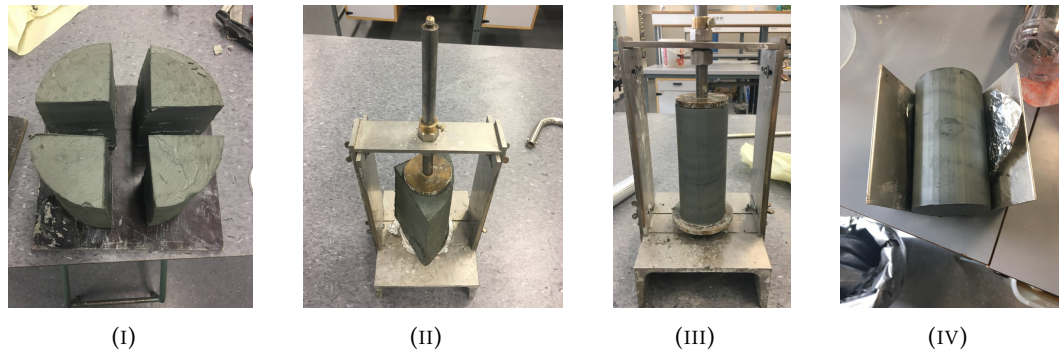
FIGURE 4.7: Triaxial specimen trimming. (I) Subdivision of a slice into four quarter pieces. (II) A quarter piece in the triaxial trimming device. (III) Excess material is cut off and the specimen achieves a diameter of 54 mm. (IV) The trimmed specimen is put in a crib and the ends are cut off so the height becomes 100 mm.

4.3 Index tests

Index tests were carried out on material from the top slice of DD-1 and the triaxial specimen. The Atterberg limits, grain size distribution, average density, grain density, salinity and water content were measured. A short description of the test procedures are explained in the following.

Density and water content

Average density

The average density ρ_a was determined by weighing parts of the mini-block samples with a known volume:

$$\rho_a = \frac{m_{sample}}{V_{sample}} \qquad [\text{g/cm}^3] \quad (4.1)$$

Accordingly, the average unit weight γ_a was achieved by multiplying with the gravitational constant $g = 9.81 \text{ m/s}^2$:

$$\gamma_a = \rho_a \cdot g \qquad [\text{kN/m}^3] \quad (4.2)$$

Grain density

The grain density ρ_s is the average density of solid particles in a soil:

$$\rho_s = \frac{m_{\text{solid particles}}}{V_{\text{solid particles}}} \qquad [\text{g/cm}^3] \quad (4.3)$$

Accordingly, the unit weight of solids γ_s is defined as:

$$\gamma_s = \rho_s \cdot g \qquad \text{[kN/m}^3\text{]} \quad (4.4)$$

A pycnometer with known weight and volume was used to determine the grain density ρ_s. First, the density of water $\rho_w = 1$ g/cm^3, the known pycnometer mass and volume was used to obtain the mass of the pycnometer filled with water. Then, the pycnometer was filled with clay material (dry mass > 25 g) and distilled water. Thereafter, the pycnometer containing the suspended material was put in a vacuum desiccator which removed air from the sample. Next, the air evacuated pycnometer containing clay suspension was re-filled with distilled water and its weight was recorded. Afterward, the suspension was poured in a cup for drying. Drying was performed according to ISO 17892-1:2014 and the dry weight was found. The grain density was calculated as:

$$\rho_s = \frac{m_{\text{dry sample}} \cdot \rho_{\text{water}}}{m_{\text{pycn. + water}} + m_{\text{dry sample}} - m_{\text{pycn. + water + sample}}} \qquad \text{[g/cm}^3\text{]} \quad (4.5)$$

Water content

The water content was determined by drying moist samples with known mass in an 105 °C oven. After 24 hours of drying, the weight of the dry sample was recorded and the water content w was calculated as:

$$w = \frac{m_{\text{container + moist sample}} - m_{\text{container + dry sample}}}{m_{\text{container + dry sample}} - m_{\text{container}}} \cdot 100 \qquad \text{[\%]} \quad (4.6)$$

Degree of saturation, porosity and void ratio

The measured average density $\gamma_a = \gamma$, grain density γ_s and water content w was used to calculate the degree of saturation, porosity and void ratio. The degree of saturation S_r is the ratio of volume of water V_{water} and total available pore volume $V_{\text{voids}} = V_{\text{air}} + V_{\text{solid particles}}$:

$$S_r = \frac{V_{\text{water}}}{V_{\text{voids}}} = \frac{w \cdot \gamma}{\gamma_w \cdot (1 + w - \frac{\gamma}{\gamma_s})} \qquad \text{[\%] or unitless} \quad (4.7)$$

Porosity n is the ratio of volume of voids and total volume of the sample:

$$n = \frac{V_{\text{voids}}}{V} = 1 - \frac{\gamma}{\gamma_s \cdot (1 + w)} \cdot 100\% \qquad \text{[\%]} \quad (4.8)$$

Void ratio e is the ratio of volume of voids and volume of solid particles:

$$e = \frac{V_{\text{voids}}}{V_{\text{solid particles}}} = \frac{\gamma_s \cdot (1 + w)}{\gamma} - 1 \qquad \text{[unitless]} \quad (4.9)$$

Atterberg limits

Depending on its water content, natural clay can appear in one of four states: plastic, liquid, crumbling or hard. Clay behaves differently in each state with varying engineering properties. The Atterberg limits represent the boundaries between each state. The liquid limit w_L is the water content at which clay changes from liquid to plastic state, and the plastic limit w_P is the water content when clay becomes more plastic when dried further. The shrinkage limit w_S is the boundary between the crumbling and hard state. Only the liquid limit and plastic limit were determined. The methodology followed ISO 17892-12:2018. First, approximately 200 g clay material was put in a bowl. The material was remoulded with a spatula until the remoulded paste was consistent. This remoulded paste was used for both liquid limit and plastic limit determination.

The Casagrande method was used for liquid limit testing. First, the remoulded clay paste was placed and spread out in a Casagrande cup (see Figure 4.8 (II)). Then, the grooving tool was used to cut a groove in the paste by a single stroke and the cam was rotated until the groove closed over a 10 mm length. The number of rotations were recorded. Thereafter, the paste was added to the remaining paste in the bowl and the cup was cleaned. The paste in the bowl was dried for 30 seconds using a heat gun. The procedure was repeated 4 times to obtain the required amount of measurements according to ISO 17892-12:2018.

The plastic limit was determined by rolling out the remoulded paste. A small portion of the paste was moulded into threads which were placed on a mixing plate. The threads were rolled backward and forward untill they crumbled at 3 mm diameter. Then, the threads were placed in a container with a lid and the water content was measured. Four containers were filled with crumbling threads.

(I) Remoulded paste.   (II) Casagrande cup.   (III) Plastic limit equipment.

FIGURE 4.8: Atterberg limit testing.

After the plastic limit and liquid limit was obtained, the plasticity index I_P and liquidity index I_L was calculated using the following equations:

$$I_P = w_L - w_p \quad [\%] \quad (4.10)$$

$$I_L = \frac{w - w_P}{w_L - w_p} \quad [\%] \quad (4.11)$$

Grain size distribution

The grain size distribution was obtained by the hydrometer method described in ISO 17892-4:2016. First, 47.16 g of moist clay from the top slice was brushed through the 0.063 mm sieve into a bowl by adding distilled water. Then, the material < 0.063 mm was poured into a 1 L cylindrical measuring jar. 20 mL dispersion agent was added to prevent flocculation of particles. The jar was filled with distilled water up to 1 L and a plug was placed on the top. Thereafter, the jar was turned end-over-end 60 times for 2 minutes to mix the suspension. Now, the hydrometer was placed in the jar and read for time step [1, 2, 5, 10, 20, 40, 80, 180, 240, 400, 1400] minute(s). For each time step, the hydrometer was read twice and the temperature was measured. The grain size distribution was calculated in Excel.

Salinity

Salinity can be estimated by measuring the electrical conductivity of expelled pore water. The electrical conductivity can be correlated with salt content by a diagram obtained by calibration tests of solutions with known salt concentration and measured conductivity. Starting out salinity testing, a small portion of clay was remoulded and four plastic containers were filled up to 45 mL. Then, the containers were placed in a centrifuge for 15 minutes. As shown in Figure 4.10, very little porewater expelled from the sample. This made it impossible to measure the electrical conductivity.
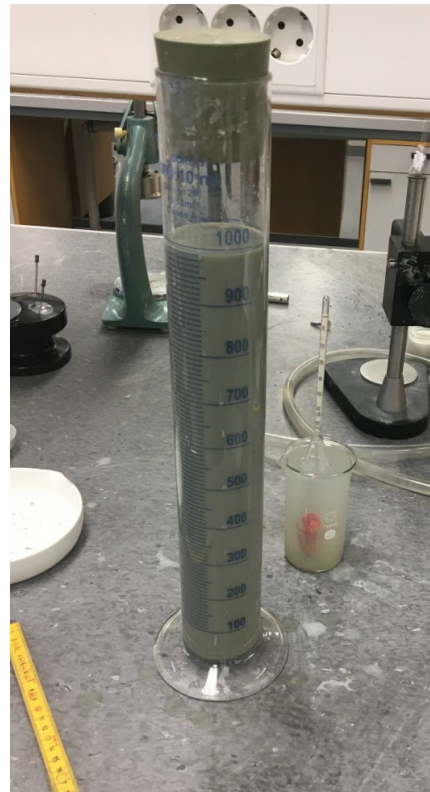
FIGURE 4.9: Hydrometer method. The cylindrical jar with clay suspension and top cap is shown in the front. The hydrometer was placed in a water filled cup in between the readings as seen in the background to the right.
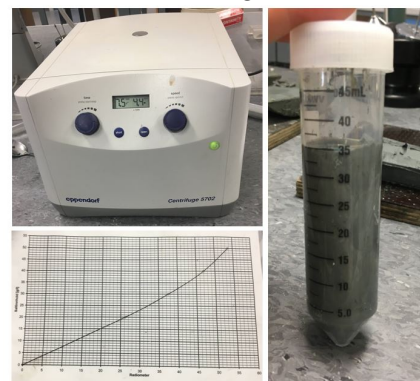
FIGURE 4.10: Salinity measurement. Top left: Centrifuge. Bottom left: Diagram correlating electrical conductivity and salinity. Right: Plastic container with remoulded sample after centrifuging.

Classification shear strength

Falling cone tests were performed to determine the classification undisturbed shear strength c_u and remoulded shear strength c_{ur}. With this, the sensitivity $S_t = c_u/c_{ur}$ was calculated. The test procedure is described in ISO 17892-6:2017.

A cone apparatus, a set of four falling cones and the two clay cubes (prepared in Figure 4.6) were used. Each of the two clay cubes were cut in half (on the height axis) resulting in four rectangular prisms of dimension $50 \times 50 \times 25$ mm^3. Each prism had 9 test points for undisturbed testing, distributed evenly across the surface as shown in Figure 4.11 (III). On each test point, the cone was dropped from the apparatus and the penetration was recorded. The chosen 100 g cone was too light for adequate penetration according to the standard for the first 9 measures. Thus, the 400 g cone was picked for the remaining measures. The recorded penetration and the mass of the cone was correlated with the undisturbed shear strength c_u by the following equation:

$$c_u \text{ (or } c_{ur}) = c \cdot g \cdot \frac{\text{mass of the cone}}{\text{average cone penetration}^2} \qquad \text{[kPa]} \quad (4.12)$$

The constant c is dependent on the cone mass and tip angle as seen in the Table below.

TABLE 4.2: Set of fall cones. Modified from ISO 17892-6:2017.

Mass [g]	10	60	100	400
Tip angle β [°]	60	60	30	30
Constant c	0.80	0.80	0.27	0.27

For measurement of the remoulded shear strength, the clay material was remoulded and placed in a cup using a spatula. Each cup had two test points. Four cups were prepared, giving 8 measurements. The remoulded shear strength c_{ur} was calculated by Equation (4.12).

| (I) | (II) | (III) |
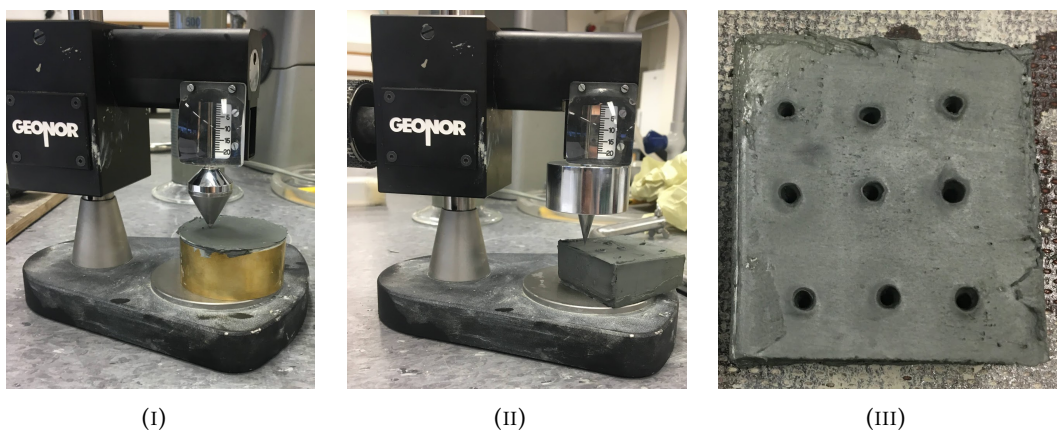
FIGURE 4.11: Falling cone tests. (I) Remoulded shear strength testing. (II) Undisturbed shear strength testing. (III) The 9 test points after undisturbed shear strength testing.

Chapter 5

Triaxial testing

The thermomechanical behavior of quick clay was investigated by temperature modified triaxial testing. A three-dimensional stress was applied on a cylindrical specimen before increasing σ_a untill it failed. For temperature elevated tests, the triaxial apparatus was wrapped with a self-produced removable heating sleeve. A schematic of the triaxial test principle is shown in Figure 5.1. The stress condition, temperature level and drainage conditions were varied to investigate shear strength parameters, pore pressure, volumetric deformation, stiffness and stress-strain behavior.
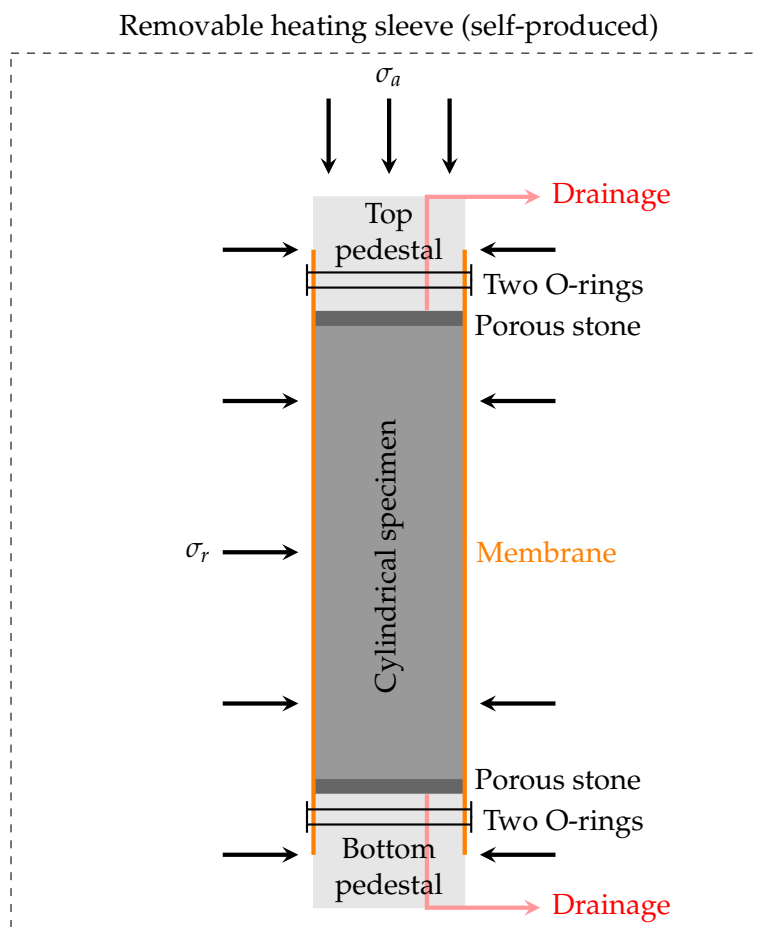
FIGURE 5.1: The setup and stress condition in a triaxial test. The apparatus was wrapped with a self-produced removable heating sleeve.

5.1 Test equipment

Two types of triaxial apparatuses are in common use at the NTNU soil mechanics laboratory, but none of them can control temperature. There were different suggestions to modify the apparatuses such as installing internal ring heaters, wrapping them with an electrical heating sleeve or feed the cells with warm water from the water system in the building. Due to cost and time limitations, a simple removable heating sleeve was made of a plastic bucket, tarpaulin, duct tape and water warmed by an immersion circulator. The heating sleeve was designed for the triaxial apparatus shown in Figure 5.2 with an internal load cell and unfortunately without the possibility of adding back pressure.
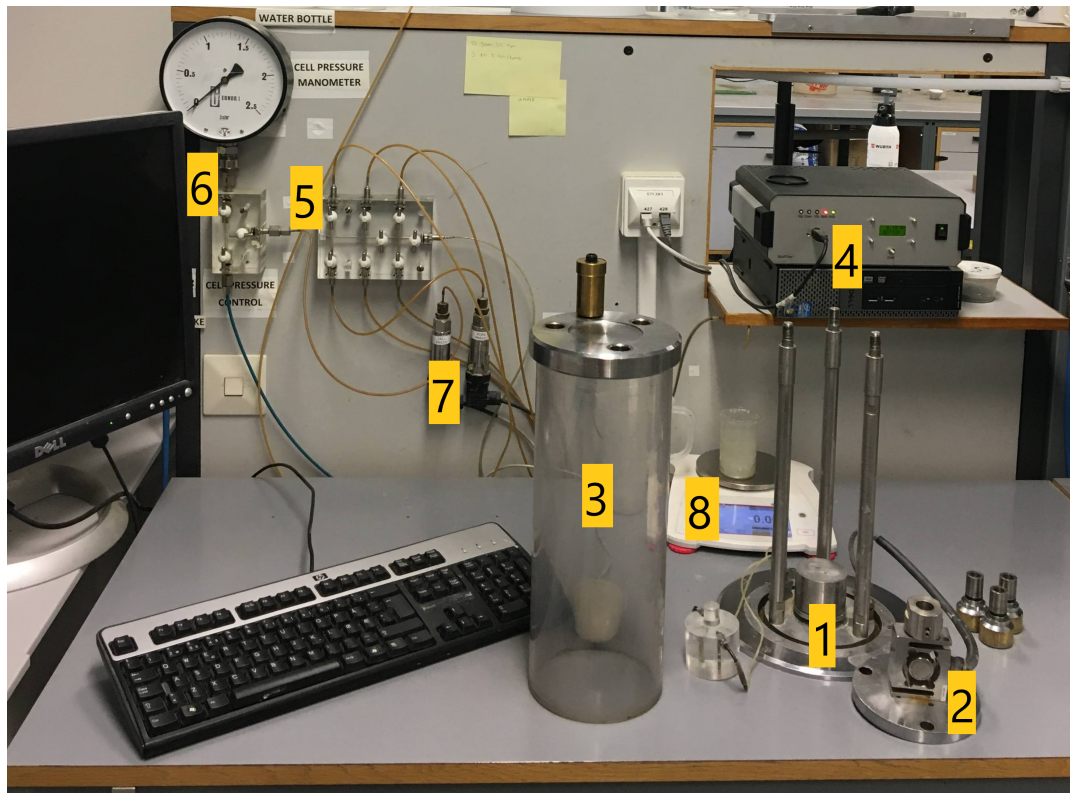
FIGURE 5.2: Front view of the triaxial apparatus. (1) Triaxial cell with base plate. (2) Loading unit for reading of required vertical load on the specimen. (3) Perspex glass with top cap. (4) Computer and loading unit recorder. (5) Valve block for control of the fluid flow from or into the specimen under various test conditions. (6) Constant - pressure cell, with acquisition and regulation system for the cell pressure. (7) Pore pressure acquisition system. (8) Scale for measurement of drained pore water.

The heating sleeve

The heating sleeve was based on the idea of surrounding the entire triaxial cell in a temperature elevated environment. Water was used as a heating medium, flowing in a circular motion around the cell. Steady flow was important to acquire even water temperature. The sombrero ($\sin x / x$) shaped tarpaulin placement was chosen to avoid joints, which minimized the potential of water leakages. Different water heating options such as using pre-heated water or fish tank heaters were thought of,

but the immersion circulator originally intended for Sous Vide cooking was picked due to the accurate temperature control. Due to the immersion circulator opposing fire hazard issues in becoming very hot at high temperatures, the water temperature was not raised any higher than 50 °C. The step wise procedure of making the heating sleeve was as following:

0. *Equipment*: Two 10 L plastic buckets, waterproof tarpaulin, immersion circulator (Sous Vide circulator 44-4253, Clas Ohlson), duct tape, scissors and a knife.

1. *Preparation*: The bottom of one plastic bucket was removed with a knife as illustrated in Figure 5.3 (I). A quadratic piece of waterproof tarpaulin sheet was folded onto the cylinder in a sombrero shape as shown in Figure 5.3 (II). To hold the tarpaulin in place, duct tape was wrapped around the cylinder multiple times. Figure 5.4 shows two views of the created tarpaulin bucket.

(I)   (II)
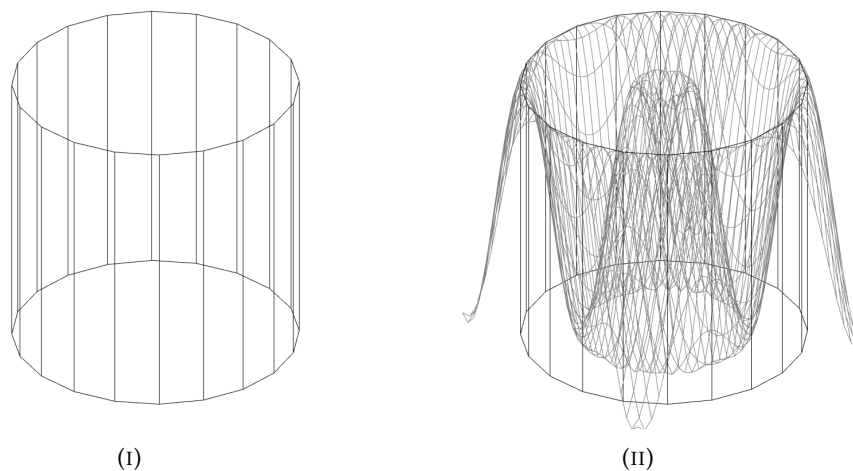
FIGURE 5.3: Heating sleeve preparation. (I) Illustration of a 10 L plastic bucket without bottom. (II) Schematic of the plastic bucket without bottom equipped with a quadratic waterproof tarpaulin sheet placed in a sombrero shape.

(I)   (II)
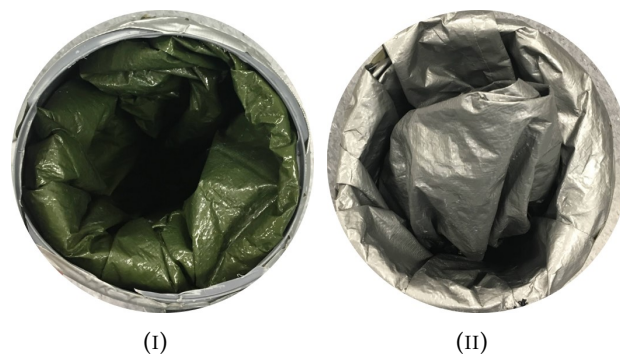
FIGURE 5.4: Bottom (I) and top (II) view of the tarpaulin bucket.

2. *Installation*: The tarpaulin bucket without bottom was put over the triaxial cell as shown in Figure 5.5.

(I) (II) (III)
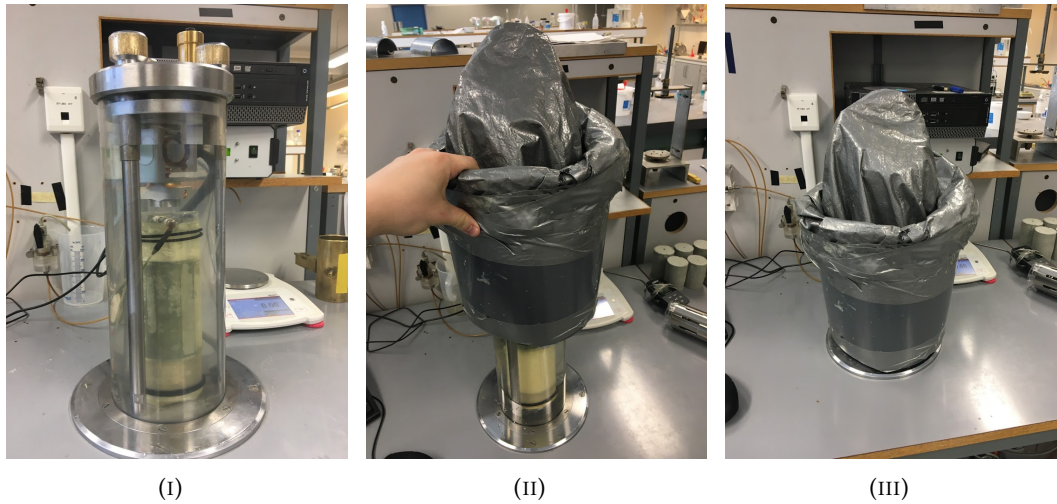
FIGURE 5.5: Heating sleeve installation. (I) The triaxial cell with a built-in specimen before installation of the heating sleeve. (II) Putting the heating sleeve over the triaxial cell. (III) The heating sleeve standing on the table top surrounding the triaxial cell.

3. *Operation*: Water was filled in another bucket (see Figure 5.6 (I)) and was poured from above into the tarpaulin bucket. Water was added up to 5 cm below the top. Now the immersion circulator (shown in black in Figure 5.6 (II) and (III)) was mounted and turned on. The immersion circulator is an electrically powered device employing a motorized impeller, a heating element and a thermometer to circulate and heat water to an accurate temperature. The adequate temperature and standby time was set on the immersion circulator touch pad.

(I) (II) (III)

FIGURE 5.6: Heating sleeve operation. (I) Pouring water from another bucket into the tarpaulin. (II) Mounting the immersion circulator and starting it by selecting temperature and time settings on the touch pad. (III) Full view of the triaxial apparatus wrapped with the heating sleeve.

5.2 General test procedure

The triaxial test procedure can be divided into the four following steps:

Build-in of specimen → Calibration and choice of test parameters → The consolidation phase → The shearing phase
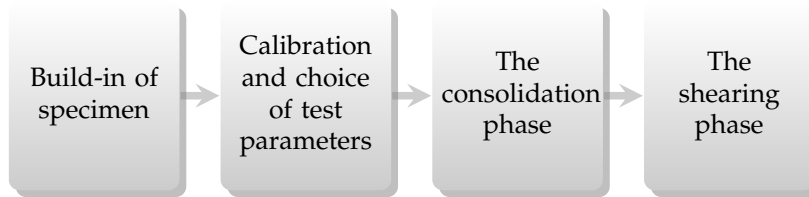
Build-in of specimen

Build-in of specimen comprises the step wise mounting procedure of cylindrical clay specimen, prepared as in Figure 4.7, in the triaxial cell. A photo series, with belonging explanations on next page, is shown in the following:

(I)   (II)

(III)   (IV)   (V)   (VI)

(VII)   (VIII)   (IX)   (X)   (XI)
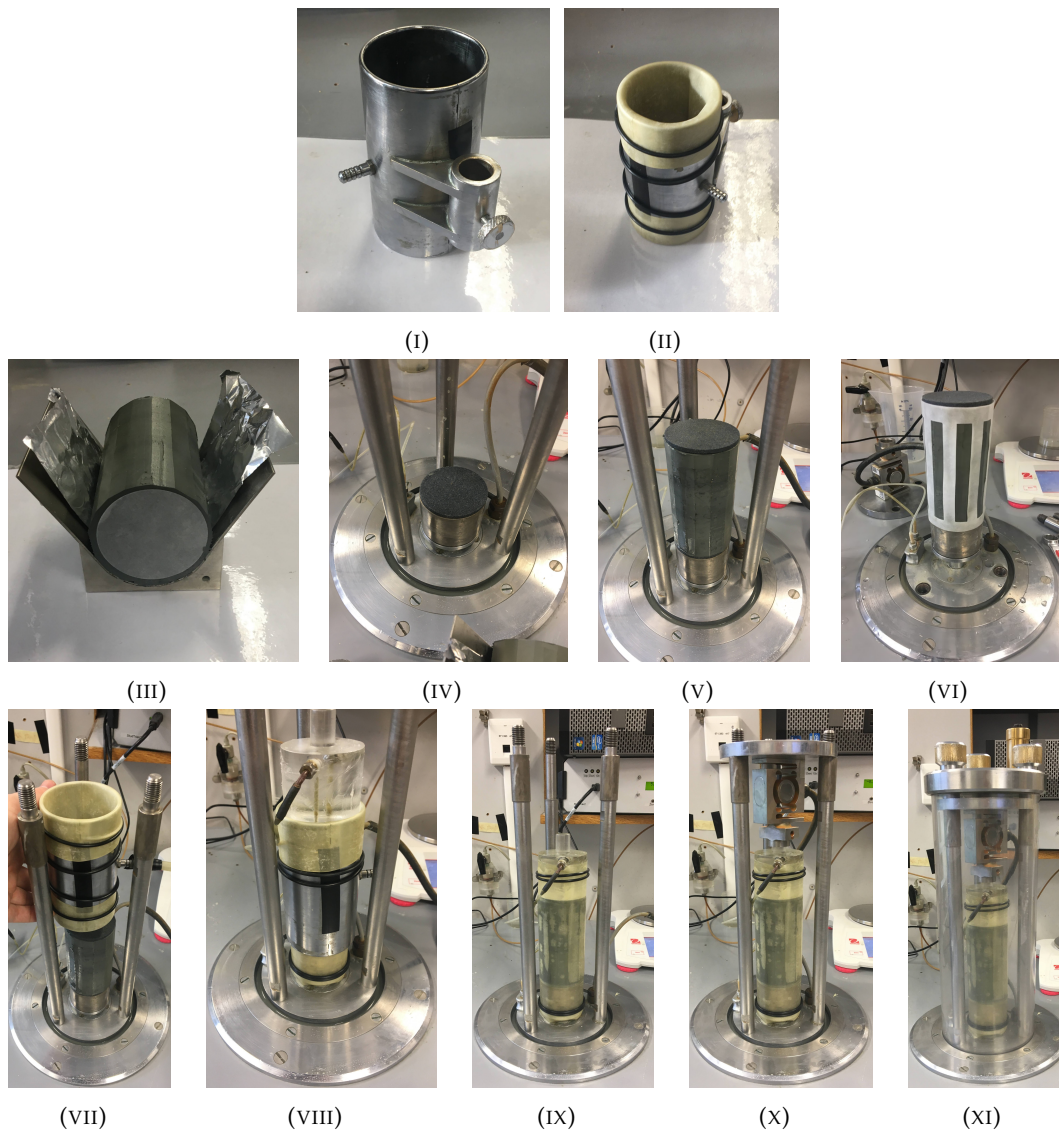
FIGURE 5.7: Photo series of the build-in procedure of cylindrical clay specimen in the triaxial apparatus.

(I) The two concave rubber membrane cylinder device sides were connected and secured by two black pieces of electrical tape.

(II) A rubber membrane was stretched through the cylinder and fastened by four O-rings.

(III) A circular piece of wet filter paper was placed on each specimen end.

(IV) A saturated porous stone was placed on the base pedestal to allow for even water distribution through the specimen.

(V) The specimen was put on the bottom porous stone and another porous stone was placed on the specimen top. The two porous stones were always kept in a vacuum desiccator for 15 minutes beforehand to remove excess air bubbles.

(VI) The three metal rods were removed for application of a special wet triaxial drainage filter paper shown in white.

(VII) A vacuum pump was connected to the rubber membrane cylinder causing the membrane to contract toward the cylinder walls making it possible to lower the device onto the specimen.

(VIII) The top pedestal was placed on the top porous stone.

(IX) The rubber membrane was stretched onto both pedestals and secured by O-rings.

(X) The loading unit was placed on the three metal rods making contact with the top pedestal.

(XI) The triaxial Perspex cell was placed and fastened by hand tightening of the three screws.

Calibration and choice of test parameters

After build-in of the specimen, the triaxial cell was filled slowly with water giving a cell pressure σ_c of approximately 5 kPa. The gap between loading unit and top pedestal was removed by a motorized raise of the bottom pedestal as shown in Figure 5.8.

(I)   (II)
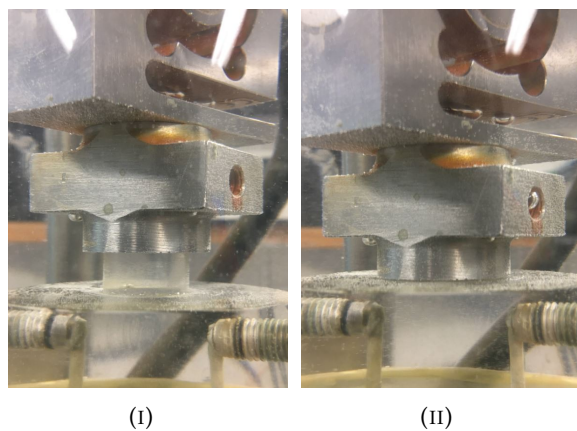
FIGURE 5.8: Go to contact procedure. (I) A visible gap between the top pedestal and loading unit. (II) Gap is removed by a motorized raise of the bottom pedestal.

Thereafter, the drainage and pressure systems were saturated with distilled water by flushing from a water reservoir through a valve block to remove air bubbles as shown in Figure 5.9 (II)). Flushing did last untill no more air bubbles were observed and with an applied cell pressure $\sigma_c = 10$ kPa.
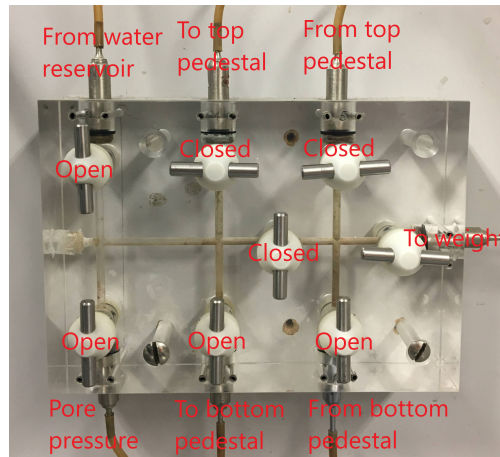
FIGURE 5.9: Valve block settings during bottom pedestal flushing. For top pedestal flushing, the top valves were opened and bottom valves closed.

Lastly, the test parameters were set depending on the test phase and program. The valve block configuration controlled the drainage conditions, cell pressure was added by increasing the flow rate from the water tank and possible additional vertical load was set in the LabVIEW 2018 software.

The consolidation phase

In the consolidation phase, an isotropic or anisotropic stress level was applied dependent on the selected test procedure. For isotropic consolidation $\sigma_1 = \sigma_2 = \sigma_3$ while an additional vertical stress $\sigma_1 > \sigma_2 = \sigma_3$ was added for anisotropic consolidation. During consolidation, pore water expelled from the specimen and flowed free through the filters, porous stones, drainage lines and into a plastic cup standing on a scale. The total weight of water at completed consolidation was measured as ΔV.

The shearing phase

In the shearing phase, the axial strain ε_a was increased at a given rate and the load required was measured (strain-controlled shearing). All shearing tests were undrained. The following data were recorded:

- ε_a: axial deformation
- P: vertical required load which can be correlated with σ_1
- σ_3: cell pressure
- u: pore pressure

5.3   Test programs

The triaxial specimen followed four different test programs with various consolidation, drainage and temperature conditions. The programs were named A, B, C

and D. Essentially, A and B comprised consolidated anisotropic undrained compression (CAU$_c$) tests at different temperatures, while C and D contained consolidated isotropic undrained compression (CIU$_c$) tests at unlike temperatures.

Test program A and B

Figure 5.10 shows a schematic of test program A and B which comprised 6 specimen divided into two groups of three named after their respective program. First, all specimen underwent anisotropic mechanical consolidation to represent the in-situ stress condition. Consolidation lasted for minimum 3 hours as recommended by NTNU Geotechnical division (2017). The anisotropic consolidation stresses were chosen in the range of (0.8, 1.0, 1.2) σ'_v and were calculated using the following equations:

$$\sigma'_v = \gamma \cdot z - u \quad \text{[kPa]} \quad (5.1) \qquad\qquad \sigma'_h = K'_0 \cdot \sigma'_v \quad \text{[kPa]} \quad (5.2)$$

where, γ is the unit weight of soil, u is the pore pressure, z is the depth below surface terrain and K'_0 is the effective at rest coefficient. The selected input parameters for each specimen is shown in Figure 5.1. Uncertainty was related to the calculation due to an unknown value of K'_0 which was set to be 0.7 (NTNU Geotechnical division, 2017). The groundwater level was 2 meter below surface. The chosen consolidation stresses for specimen B3 deviated because of an error in the calculation of density and an initial misunderstanding of the triaxial test software.

TABLE 5.1: Calculation of anisotropic consolidation stresses for test program A and B. The selected σ'_v for each specimen is highlighted in yellow. The chosen consolidation stresses for specimen B1 deviated from the calculation due to an error.

ID	z [m]	u [kPa]	γ [kN/m³]	K'_0	$0.8 \cdot \sigma'_v$ [kPa]	$1.0 \cdot \sigma'_v$ [kPa]	$1.2 \cdot \sigma'_v$ [kPa]	σ'_h [kPa]
A1	5.79	38	17.8	0.7	52	65	**78**	55
A2	5.94	39	18.2	0.7	**55**	69	82	38
A3	5.79	38	17.7	0.7	52	**65**	78	45
B1	5.79	58	17.8	0.7	52	65	**78**	55
B2	5.94	59	18.1	0.7	**55**	68	82	38
B3	7.70	58	18.5	0.7	69	86	103	60

After initial anisotropic mechanical consolidation, the test programs differed. The heating sleeve was applied for specimen A1 - A3 which raised the temperature. Hence, these specimen encountered a secondary consolidation named thermal consolidation. The consolidation stresses were unchanged during thermal consolidation. The temperature of specimen B1 - B3 was never increased.

Lastly, all specimen were sheared by increasing the strain and measuring the required load (strain-controlled shearing). The drainage lines were closed, and radial confining stress σ_r was unchanged. Strain rates were $\varepsilon_a = 1$ mm/hour. The temperature of specimen A1 - A3 was measured immediately after dismounting the cell using a thermometer.

Specimen ID	Anisotropic mechanical consolidation	Thermal consolidation	Undrained shearing
A1	R.T, 23 °C $\sigma_a = 78$ kPa $\sigma_r = 55$ kPa	Heater, 50 °C $\sigma_a = 78$ kPa $\sigma_r = 55$ kPa	Heater, 50 °C $\sigma_3 = \sigma_r = 55$ kPa
A2	R.T, 23 °C $\sigma_a = 55$ kPa $\sigma_r = 38$ kPa	Heater, 50 °C $\sigma_a = 55$ kPa $\sigma_r = 38$ kPa	Heater, 50 °C $\sigma_3 = \sigma_r = 38$ kPa
A3	R.T, 23 °C $\sigma_a = 65$ kPa $\sigma_r = 45$ kPa	Heater, 50 °C $\sigma_a = 65$ kPa $\sigma_r = 45$ kPa	Heater, 50 °C $\sigma_3 = \sigma_r = 45$ kPa
B1	R.T, 23 °C $\sigma_a = 78$ kPa $\sigma_r = 55$ kPa		R.T, 23 °C $\sigma_3 = \sigma_r = 55$ kPa
B2	R.T, 23 °C $\sigma_a = 55$ kPa $\sigma_r = 38$ kPa		R.T, 23 °C $\sigma_3 = \sigma_r = 38$ kPa
B3	R.T, 23 °C $\sigma_a = 138$ kPa $\sigma_r = 55$ kPa		R.T, 23 °C $\sigma_3 = \sigma_r = 55$ kPa

FIGURE 5.10: The test procedure of program A and B. All tests are essentially CAU$_c$ tests but at elevated temperature for program A and room temperature for B. R.T stands for room temperature. The heater temperature denotes the water temperature in the heating sleeve, and must not be confused with the specimen temperature.

Test program C and D

Figure 5.11 presents the schematic procedure of the eight specimen following test program C and D. Program C had 5 specimen and D possessed 3 specimen. The specimen were named after their respective program. The eight specimen experienced isotropic consolidation with similar comparable consolidation stresses, but with a difference in temperature. At the start of consolidation, the heating sleeve was applied for specimen C1 - C5 with a temperature of 50 °C. This temperature elevated consolidation was called thermomechanical consolidation. The temperature was never raised for specimen D1 - D3. The selected consolidation stress level, to 200 and 300 kPa, was based on the similar values being used by Abuel-Naga (2006). It should be noted that the drainage lines were closed for specimen C3 and D3 for measurement of pore pressures.

After isotropic thermomechanical and mechanical consolidation, the specimen were sheared at the similar temperature as during consolidation. Therefore, specimen C1 - C5 were sheared at 50 °C and D1 - D3 at room temperature $\approx$ 23 °C. The confining

stress σ_r was similar to the consolidation confining stress for specimen C1 - C3 and D1 - D3. σ_r was reduced to respectively 30 and 50 kPa for specimen C4 and C5. The temperature of C1 - C5 was measured immediately after dismounting the cell with a thermometer.
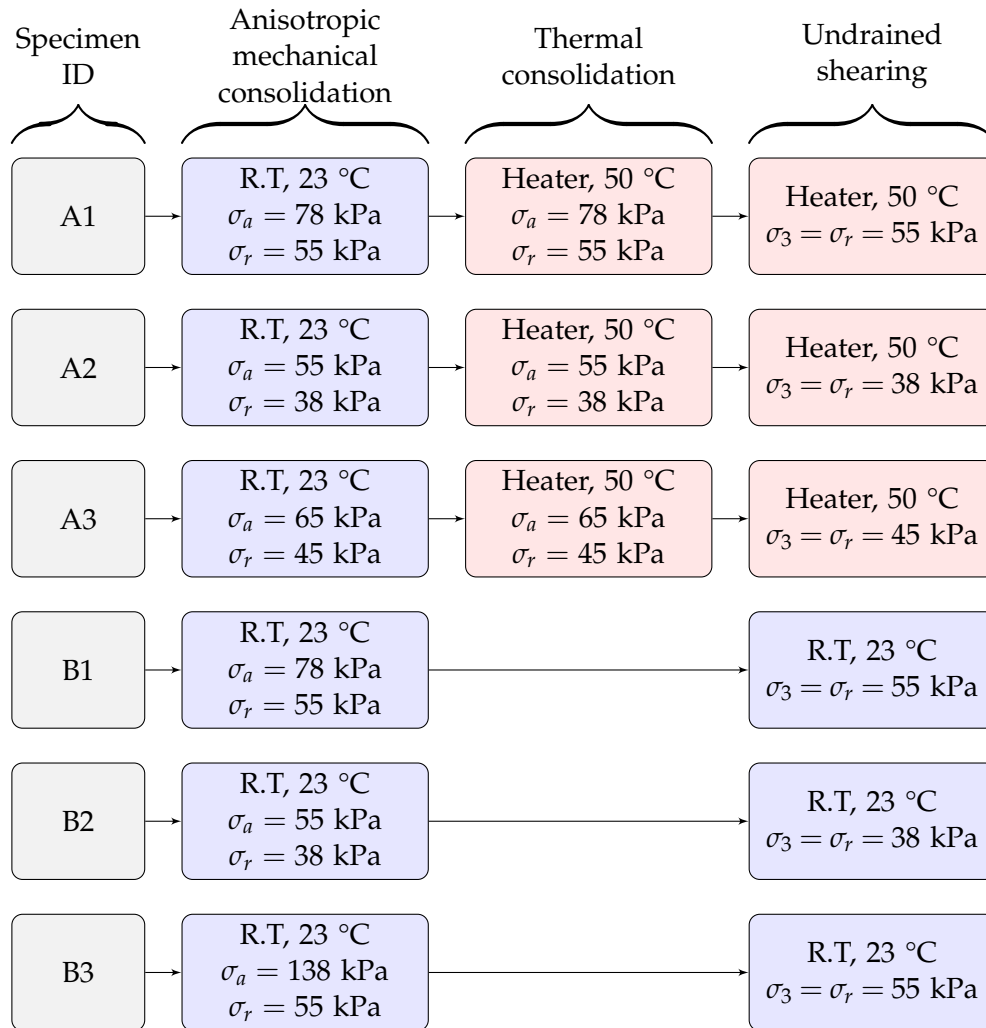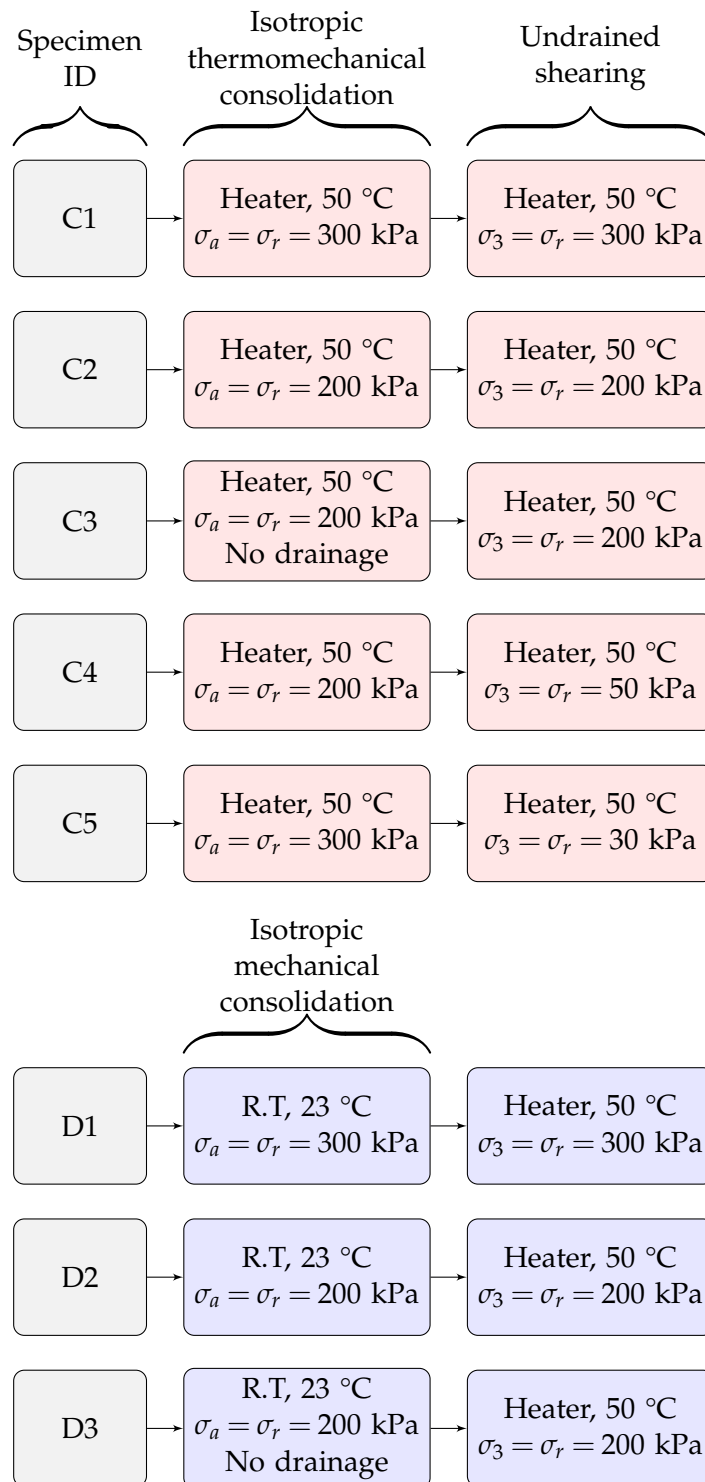

FIGURE 5.11: The test procedure of program C and D. All tests are essentially CIU$_c$ tests but at elevated temperature for program C and room temperature for D. R.T stands for room temperature. The heater temperature is the water temperature in the heating sleeve, and must not be confused with the specimen temperature.

5.4   Calibration tests

With the aim of determining the specimen temperature after application of the heating sleeve, a temperature calibration test was carried out. A triaxial test specimen was mounted in the cell following the build-in procedure in Section 5.2. Then, a thermometer originally intended for cooking was placed in the middle of the specimen. The thermometer wire was directed through the hole in the loading unit, screw hole and out of the cell. Next, the heating sleeve was applied with a water temperature of 50 °C and the temperature of the specimen was recorded with time. The thermometer readings had an accuracy of $\pm 1°C$.

| (I) | (II) | (III) | (IV) |
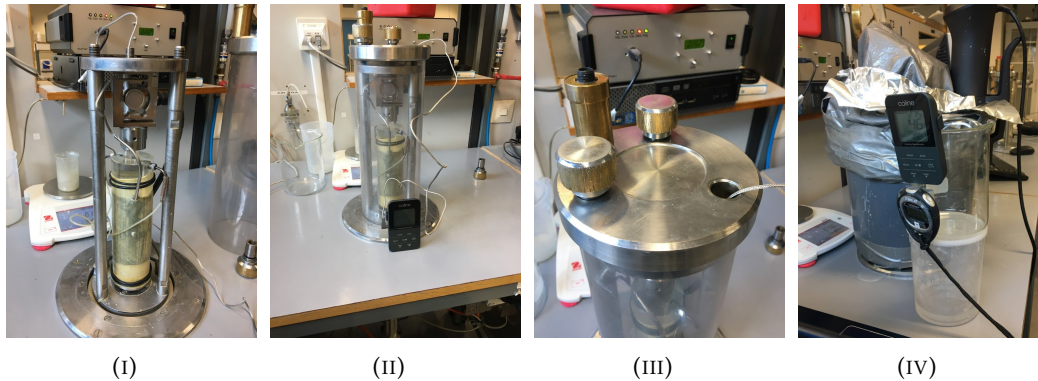
FIGURE 5.12: Temperature calibration test. (I) Thermometer placed inside specimen piercing the rubber membrane. (II) Thermometer placed inside triaxial cell. (III) Wire entrance to the triaxial cell through a screw hole. (IV) Final setup with thermometer and triaxial cell encapsulated by the heating sleeve.

As recommended by Abuel-Naga (2006), another calibration test was carried out to measure the temperature response of the triaxial cell during drained heating. A cylindrical plastic specimen was mounted in the triaxial cell and the temperature was raised by the heating sleeve (see Figure 5.13). Abuel-Naga (2006) used a metallic specimen, but a plastic specimen should give a similar result. The amount of drained pore water ΔV was measured.

| (I) | (II) | (III) |
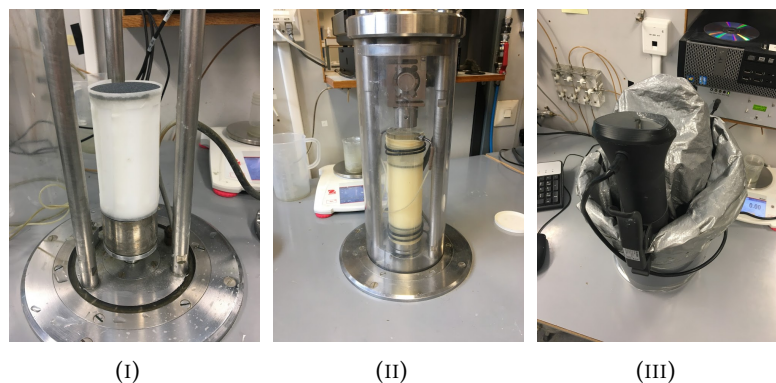
FIGURE 5.13: Temperature response of the triaxial cell. (I) Plastic specimen wrapped with filter paper. (II) Build-in of plastic specimen. (III) Heating sleeve surrounding the triaxial cell with plastic specimen.

5.5 Corrections

In order to evaluate the measured data, some corrections and calculations were needed. Raw data processing was done in MATLAB (see Appendix C) and plotting using the pgfplots package in LaTeX. Several corrections are mentioned in ISO 17892-9:2018 but only the practiced corrections by NTNU were carried out.

Area

As recommended by NTNU Geotechnical division (2017), the initial surface area A_0 was corrected by Equation 5.3 because consolidation leads to a small reduction of the specimen volume.

$$A_a = A_0 \cdot \frac{1 - \frac{\Delta V}{V_0}}{1 - \frac{\Delta V}{3V_0}} \qquad [\text{m}^2] \quad (5.3)$$

where A_a = specimen area after correction, V_0 = build-in specimen volume and ΔV = expelled pore water.

The axial confining stress during consolidation was calculated by the corrected area A_a, vertical required load P and cell pressure $\sigma_c = \sigma_3$ as:

$$\sigma_a = \frac{P}{A_a} + \sigma_3 \qquad [\text{kPa}] \quad (5.4)$$

During shearing, an additional area correction was recommended by NTNU considering the barrel shaped failure mode. The axial confining stress during shearing was calculated as:

$$\sigma_a = \frac{P(1 - \varepsilon_a)}{A_a} + \sigma_3 \qquad [\text{kPa}] \quad (5.5)$$

Drained pore water

A non-standard effect was seen in the ΔV measurements, in which the measured weight decreased for some time steps. This happened because of evaporation of the accumulated drained pore water located in the cup on the scale. Therefore, the measured ΔV was artificially low. For example, as seen in Table 5.2, the weight decreased by evaporation from 5.32 to 5.31 before increasing again. To correct for this evaporation effect, a MATLAB script was created to only select the measurements which were recorded after an increase in weight.

TABLE 5.2: Selected weight measurements for specimen A1.

Time	08:54	08:55	09:04	10:33	10:34	10:36	10:38
Weight [g]	0	0.59	4.23	5.28	5.32	5.31	5.35

Another ΔV correction was carried out due to a significant increase of drained water immediately after starting out consolidation (see Table 5.2). Most likely, this water originated from flushing right before consolidation and not from the specimen. To correct for these artificially high values, a correction was needed. Two approaches to the correction were considered:

1. Subtract the weight measurements for the first 2 minutes of each tests. This assumed that all flushing-induced water was drained during the first 2 minutes.

2. Subtract the weight measurements from a calibration test on a plastic specimen with similar test conditions.

Initially it was decided to use correction approach 2). However, since flushing took place over a different time span due it being stopped after no more air bubbles were seen, this approach would be heavily influenced by the flushing time in the calibration test. Put in other words, it was difficult to carry out a calibration test with exact similar test conditions as the triaxial tests on clay specimen. Therefore, approach 1) was selected and implemented in a MATLAB script.

Chapter 6

Micro-CT

6.1 Industrial micro-CT

Micro-CT is a non-destructive imaging technique for visualization of internal structures of objects. The technique is similar to medical CT scan imaging, but has an increased resolution. Figure 6.1 shows a typical industrial micro-CT setup. X-rays (wavelength from 0.01 to 10 nanometers) emit from decelerated electrons at the source, travels through the specimen and are recorded at the planar detector as a 2D projection image (Taina et al., 2008). The specimen is then rotated by a fraction of a degree, and a new 2D image is taken. This is repeated untill 360 degrees. The series of 2D projection images is then made into cross-sectional images (slices) by the mathematical process of reconstruction using a computer. These slices can be analyzed, processed and stacked into a 3D image.
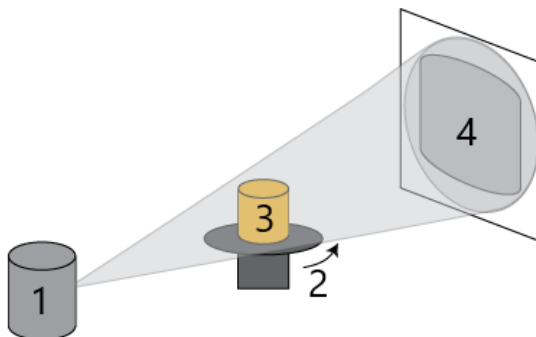
FIGURE 6.1: Typical industrial micro-CT setup showing the X-ray source (1), turntable (2), specimen (3) and planar detector (4). Modified from Ketcham (2018).

As a beam of X-ray radiation passes through the specimen, it experiences gradual attenuation due to interactions with atoms (Ketcham & Carlson, 2001; Taina et al., 2008). The amount of attenuation is dependent on the bulk density, effective atomic number and the energy of the X-ray beam (Denison et al., 1997). Consequently, different internal clay structures with unlike density and chemical composition will be characterized by distinct attenuation values. This will show as regions with contrasting brightness in a CT image. The attenuation of each voxel (volume element) in a CT image is described by the CT number. Dense structures give a high CT number (high attenuation) and opposite for low densities. Previous geotechnical applications have used this ability to differentiate high and low density structures in clay which can help visualize cracks, mini-fabrics and pores (Yang et al., 2010).

6.2 Procedure

A schematic overview of the procedure is shown in Figure 6.2. Detailed explanations are given in the next pages.
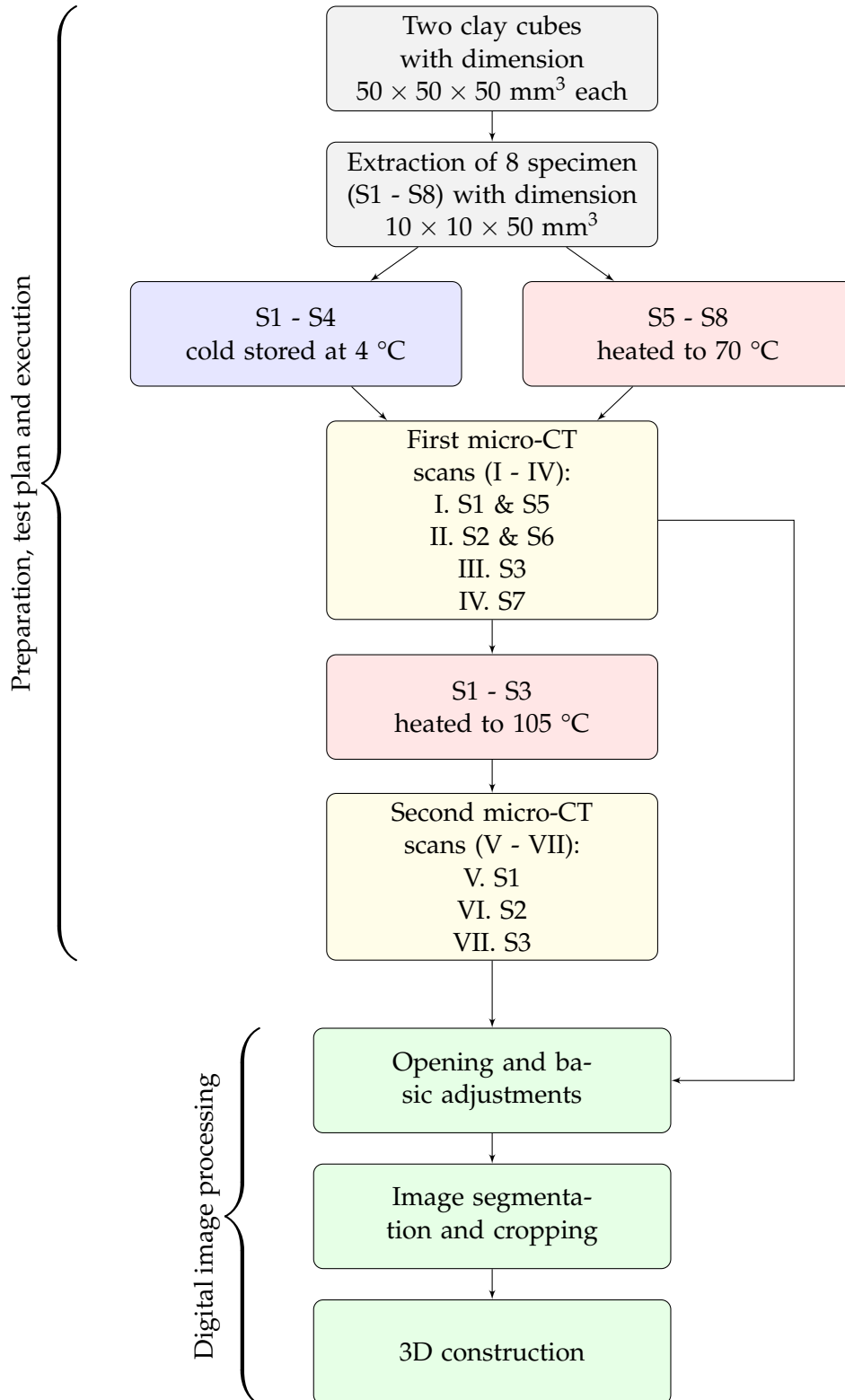
FIGURE 6.2: Schematic of the micro-CT procedure.

Preparation, test plan and execution

On the 25th of February 2021, the micro-CT specimen were cut out from the two cubes prepared as in Figure 4.6. Eight rectangular prisms with dimensions of approximately $10 \times 10 \times 50$ mm^3 were extracted using a wire saw. These specimen were numbered from 1 to 8 (hereby called S1 - S8) as shown in Figure 6.3. Immediately after extraction, S1 - S4 were wrapped in plastic foil and stored in a fridge to minimize moisture loss. S5 - S8 were heated in an oven to 70 °C for 24 hours before they were taken out, wrapped in plastic foil and stored at room temperature.

FIGURE 6.3: Photographs of the micro-CT specimen before the first scan. S1 - S4 were stored in a fridge, while S5 - S8 were heated to 70 °C before being stored at room temperature.

The first micro-CT scans took place 2th of March 2021, and was conducted by staff engineer Katharina Scheidl at the NTNU Department of Physics. A Nikon microfocus CT scanner equipped with a variety of transmission and reflection targets was used. Two specimen were scanned *simultaneously*, in which one cold-stored was placed above one pre-heated specimen inside a glass cylinder. The idea was that this would give a better basis of comparison because of similar scanning conditions (brightness and resolution). However, after the two first scans of S1 & S4 and S2 & S6, it was decided to scan specimen S3 and S7 *separately* for an attempt of better resolution. Due to time issues, specimen S4 & S8 were not scanned. After scanning, the specimen were stored at room temperature in the laboratory.

The initial idea was to only compare unlike cold-stored and heated specimen. With this, it was difficult to determine if the differences in results originated from initial specimen disturbance or heating. Thus, a decision was taken to do a second scan of S1 - S3 after being subjected to heating. S1 - S3 were heated in an oven to 105 °C from 9th of April 2021 untill taken out 30 minutes before the second micro-CT scans three days later. Plastic film was wrapped around the specimen to prevent spill in the micro-CT apparatus and for identification. The three specimen were scanned *separately*.

Digital image processing

Each micro-CT scan produced a series of 2000 cross-sectional slices which was processed in the open-source image software Fiji. Fiji is a distribution of ImageJ, containing various plugins which facilitate scientific image analysis. The step wise transformation from the sequence of 2D cross-sectional images to a 3D image was automated using the ImageJ Macro language (IJM). The IJM script for processing of

S1 is shown in Appendix B. Digital image processing was carried out in the following three steps:

1. *Opening and basic adjustments.* The 2D cross-sectional image sequence was imported from the folder location on the computer as shown in Figure 6.4 (I) and (II). Basic adjustments consisted of rotating, flipping or reversing the sequence for similar orientation of all 3D images. The adequate adjustments were customized for the separate specimen. The image sequence of S1, in Figure 6.4 (III), was reversed and rotated.

(I)   (II)   (III)
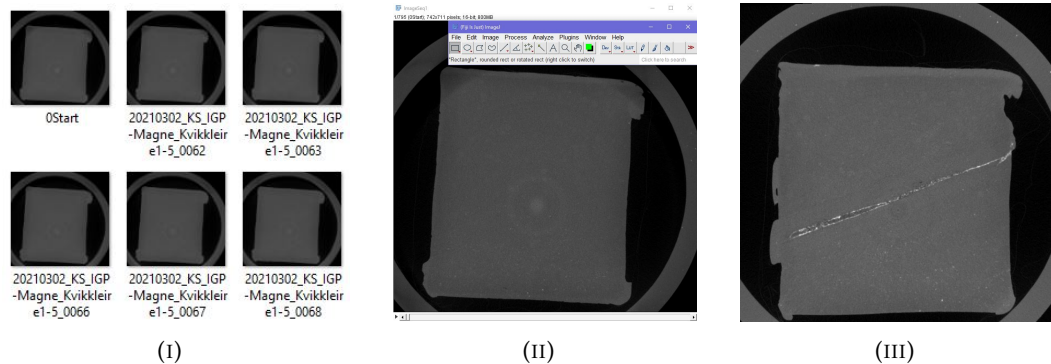
FIGURE 6.4: Opening and basic adjustments of S1. (I) Images in folder. (II) Imported image sequence in ImageJ. (III) Reversing the order and rotating the images.

2. *Image segmentation and cropping.* Each image was divided into two separate groups (black and white) based on the CT number. First, a Sobel edge detector was applied to highlight sharp changes in the CT number as shown in Figure 6.5 (I). Then, the automatic thresholding method "Intermodes" computed the threshold for each individual image. An image after performed thresholding is seen in Figure 6.5 (II). Next, the glass cylinder surrounding the specimen was removed using the polygon tool as in Figure 6.5 (III).

(I)   (II)   (III)
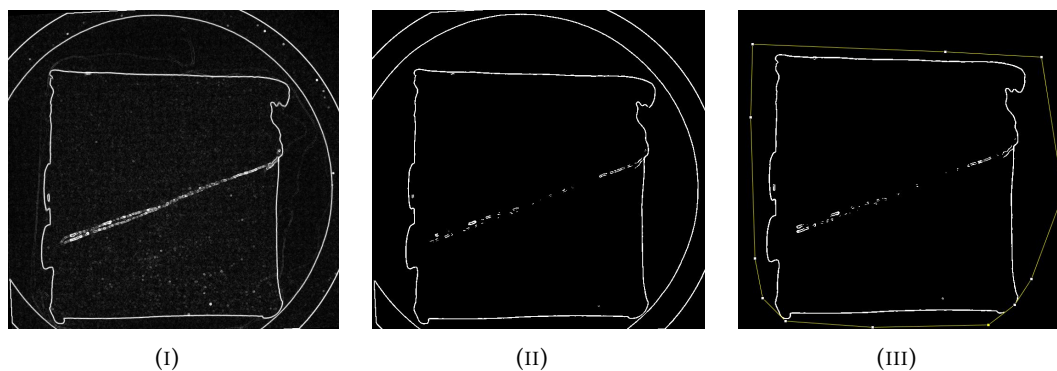
FIGURE 6.5: Image segmentation and cropping of S1. (I) Application of the Sobel edge detector. (II) Automatic thresholding by the "Intermodes" method. (III) Deleting excess structures using the polygon tool.

3. *3D construction*. The images were stacked together by the 3D viewer plugin. This created a 3D image as shown in Figure 6.6 (I). Lastly, the background was changed to white. The finalized processed 3D image is seen in Figure 6.6 (II).
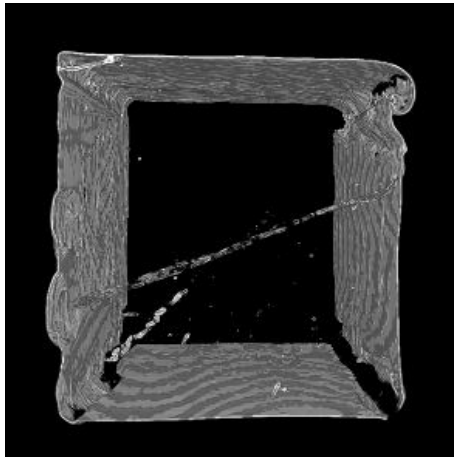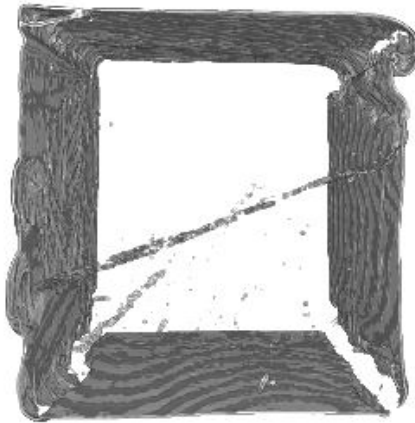
(I)   (II)

FIGURE 6.6: 3D construction of the image sequence of S1. (I) 3D image. (II) Finalized 3D image of S1 with white background.

Part III

Results

Chapter 7

Index testing

This chapter presents the results of the index tests which were performed to characterize the general properties of the quick clay at room temperature. Atterberg limit testing, the hydrometer method, falling cone tests, drying, salinity testing and density measurements were carried out. The median has been used as the selected index property for all the respective tests to eliminate outliers.

7.1 Test results

Atterberg limits and water content

Figure 7.1 shows a box plot comprising the results of water content, plastic and liquid limit testing. It is seen that the water content w > liquid limit w_L > plastic limit w_P. The median water content $w = 67\%$, median liquid limit $w_L = 42\%$ and median plastic limit $w_P = 30\%$.
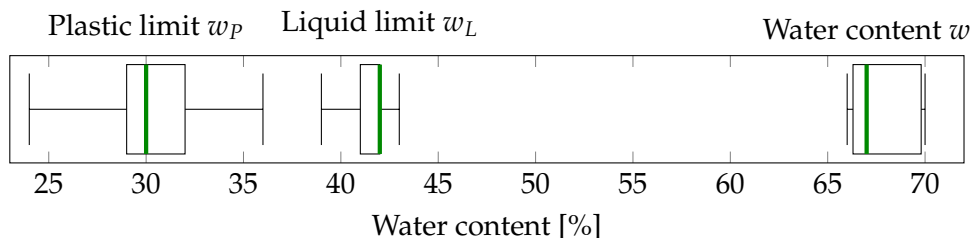
FIGURE 7.1: Results from water content (14 samples), plastic (4 samples) and liquid limit (4 samples) testing visualized in a box plot.

The liquidity index I_L and plasticity index I_P was calculated using the median values:

$$I_P = w_L - w_P = 42 - 30 = \underline{\underline{12\ \%}} \tag{7.1}$$

$$I_L = \frac{w - w_P}{w_L - w_P} = \frac{67 - 30}{12} = \underline{\underline{3\ \%}} \tag{7.2}$$

Density

The grain density ρ_s was estimated by the pycnometer test. Only one test was performed giving a grain density of 2.86 g/cm^3. It was calculated as in Equation (4.3) with the measured values:

$$\rho_s = \frac{16.69 \cdot 1}{144.42 + 16.69 - 155.28} = \underline{\underline{2.86 \, \text{g/cm}^3}} \tag{7.3}$$

Average density γ was calculated for all triaxial specimen by measuring the weight and volume. The results of the average unit weight are shown in the box plot below. The results varied between 18.1 and 18.9 kN/m^3, with a median of 18.5 kN/m^3.
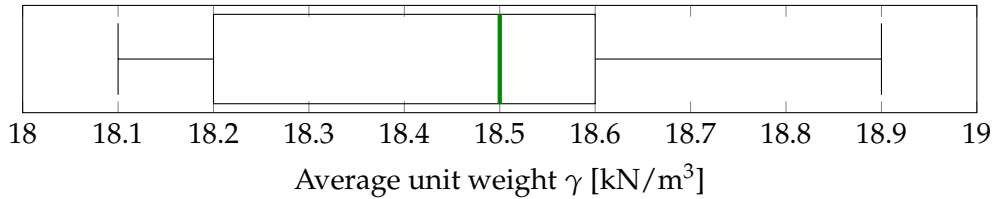
FIGURE 7.2: Results from the density measurements visualized in a box plot.

Degree of saturation, porosity and void ratio

The degree of saturation S_r, porosity n and void ratio e was calculated using the obtained median values in the following:

$$S_r = \frac{w \cdot \gamma}{\gamma_w \cdot (1 + w - \frac{\gamma}{\gamma_s})} = \frac{0.67 \cdot 1.85}{1 + 0.67 - \frac{1.85}{2.86}} = 0.86 = \underline{\underline{86 \, \%}} \tag{7.4}$$

$$n = 1 - \frac{\gamma}{\gamma_s \cdot (1 + w)} = \frac{1.85}{2.86 \cdot (1 + 0.67)} = 0.39 = \underline{\underline{39 \, \%}} \tag{7.5}$$

$$e = \frac{\gamma_s \cdot (1 + w)}{\gamma} - 1 = \frac{2.86 \cdot (1 + 0.67)}{1.85} - 1 = \underline{\underline{1.6}} \tag{7.6}$$

Classification shear strength

Figure 7.3 shows the results of the falling cone tests. The respective median values were 31 and 3 kPa which gave a sensitivity $S_t = 31/3 = 10.3$ kPa.
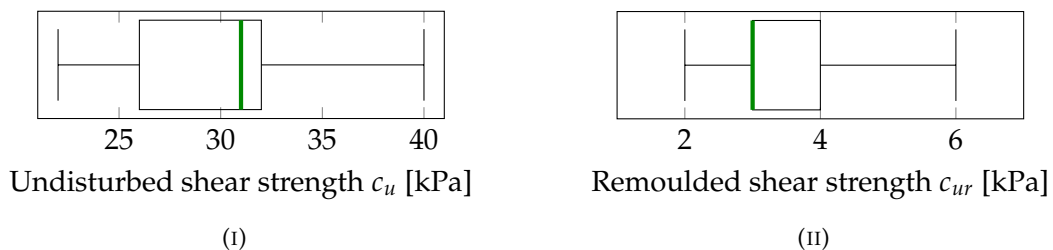
FIGURE 7.3: Classification shear strength measurements presented in box plots. Undisturbed testing consisted of 27 measurements, while remoulded testing comprised 9 measurements.

Salinity

As described in Section 4.3, not enough pore water expelled during centrifuging which made it impossible to measure the electrical conductivity (correlated with

salinity). Therefore, the salinity was determined based on previous results from salinity measurements performed by others on Norwegian quick clay.

Grain size distribution

Figure 7.4 shows the grain size distribution obtained by the hydrometer method. Approximately 60 % of the material is finer than 2 µm and therefore defined as clay. 40% is categorized as silt. Furthermore, the activity can be calculated as the ratio of the plasticity index I_P to the clay content; $12/60 = \underline{\underline{0.2}}$
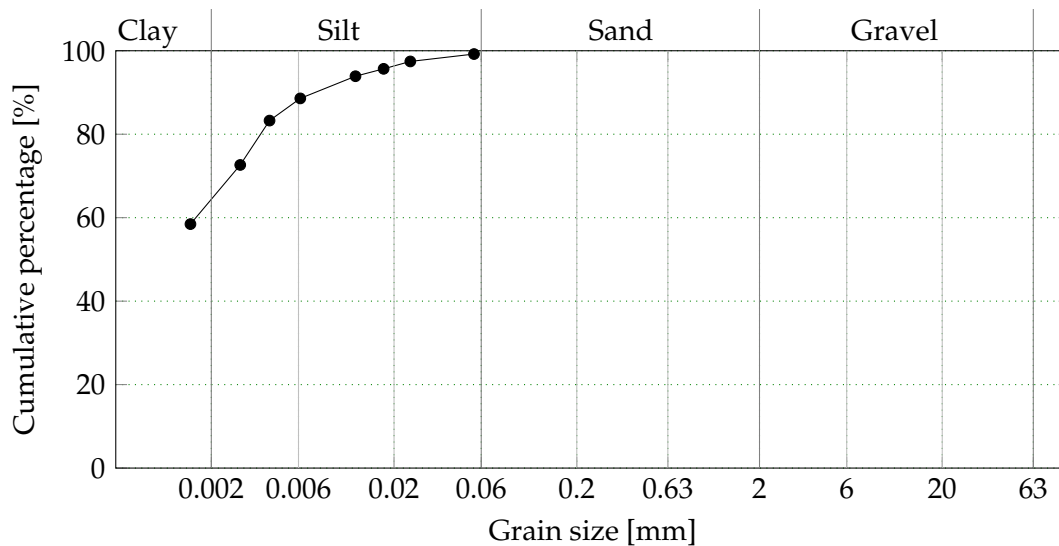
FIGURE 7.4: Grain size distribution obtained by the hydrometer method on a single sample.

7.2 Overview of test results

An overview of the measured index properties is shown in the Table below.

TABLE 7.1: Overview of measured index properties.

Water content w	Liquid limit w_L	Plastic limit w_P
67 %	42 %	30 %
Plasticity index I_P	Liquidity index I_L	Activity a
12 %	3 %	0.2
Average density ρ	Grain density ρ_s	Salinity
18.5 kN/m^3	2.86 g/cm^3	2 g/l
Undisturbed shear strength c_u	Remoulded shear strength c_{ur}	Sensitivity S$_t$
31 kPa	3 kPa	10
Saturation S_r	Porosity n	Void ratio e
86 %	39 %	1.6
Grain size distribution		
60% clay and 40% silt		

Chapter 8

Triaxial testing

8.1 Overview of test procedures

This chapter presents the results of triaxial test program A, B, C and D as well as calibration tests of the triaxial apparatus. For the sake of clarity, a schematic of the four triaxial test programs is shown in Figure 8.1. Detailed explanations of the programs are given in Section 5.3.
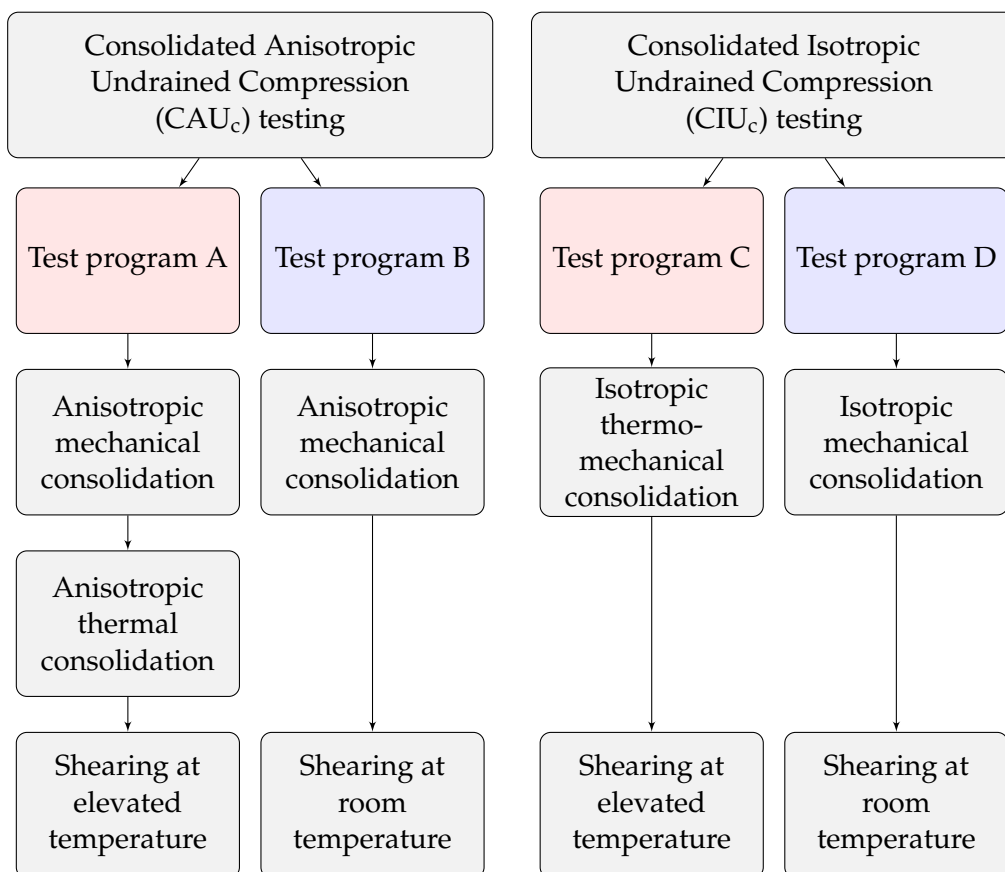
FIGURE 8.1: Schematic of the four triaxial test programs. The programs marked in red color contains phases with temperature elevation. All test phases in the blue colored programs were at room temperature.

8.2 Calibration tests

The results from the temperature calibration test and additional temperature data which was measured immediately after shearing at 50 °C for specimen A1 - A3 and C1 - C5 are shown in Figure 8.2. A polynomial function was fitted to establish a relationship between time and specimen temperature. The heating sleeve was turned on at time = 0 holding a steady water temperature of 50 °C. It is seen that the time - specimen temperature curve is linear from 25 to 40 °C before it flattens out and diverges toward 45 °C. The necessary time to reach maximum specimen temperature was about 5 - 10 hours.
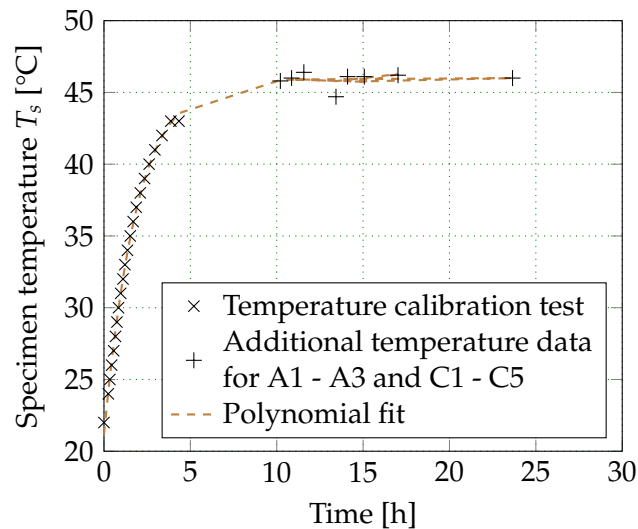
FIGURE 8.2: Specimen temperature inside the triaxial cell with heating device temperature = 50 °C.

Figure 8.3 shows the results of the amount of water ΔV expelled during heating of a plastic specimen. This was performed to measure the triaxial cell response to the application of the heating sleeve at 50 °C. No drained water was measured with time.
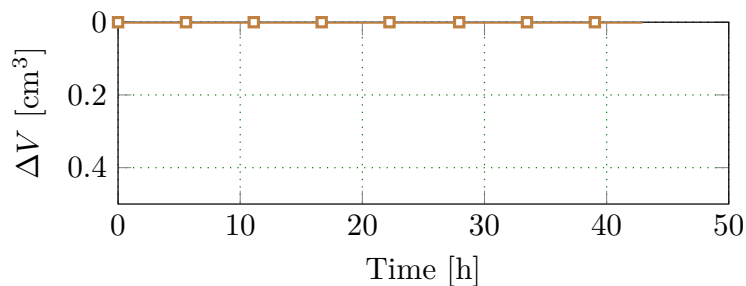
FIGURE 8.3: Triaxial cell response to application of the heating sleeve measured by heating a plastic specimen.

8.3 Consolidated Anisotropic Undrained Compression tests - program A and B

The results of the Consolidated Anisotropic Undrained Compression (CIU$_c$) tests in program A (specimen A1 - A3) and B (specimen B1 - B3) are given in the following section. Detailed explanations of the test programs are in Section 5.3.

Anisotropic mechanical and thermal consolidation

Test conditions

Figure 8.4 illustrates the stress and temperature conditions during mechanical and thermal consolidation. Test program A featured mechanical consolidation *followed by* thermal consolidation, while test program B contained *only* mechanical consolidation. Expelled pore water ΔV and axial required load P were measued.

$$\sigma_1 = \sigma_3 + P/A_a \approx \sigma_v'$$
$$\sigma_3 = \sigma_c \approx \sigma_h'$$
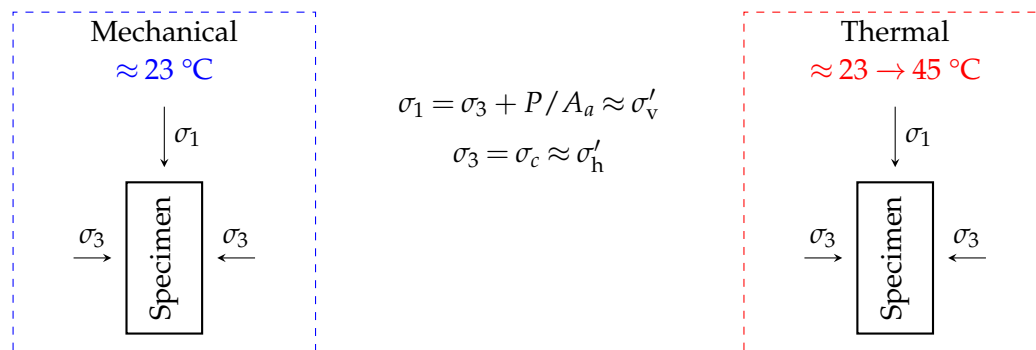
FIGURE 8.4: Simple sketches of the stress and temperature conditions during mechanical anisotropic consolidation to the left and thermal anisotropic consolidation to the right.

Drained pore water ΔV and axial deformation ε_a

Figure 8.5 shows the time - ΔV and time - ε_a plots obtained by test program A and B. The plots revealed that:

- Pore water expelled during heating of A1 - A3, reflecting on a temperature-induced compression effect. The temperature effect is as important as the mechanical effect since fairly alike amounts of water expelled by both consolidation types. However, there is uncertainty related to the mechanical measurements because of the correction of flushing.

- More water expelled by a higher consolidation stress for both types of consolidation. The effect of stress level seem to be minor for the thermal measurements since they follow rather similar curves.

- Most of the mechanically-induced water expelled during the first hour as seen by the initial steep slope of the curves. The thermal measurements had a more gentle slope.

- The necessary mechanical consolidation time, indicated by the flattening of the curves, varied between a few hours for A2, A3, B1 and B3 up to approximately 10 hours for A1. The measurements for B2 were stopped before full flattening of the curve. The necessary thermal consolidation time was longer, whereas the curves of A2 and A3 never flattened fully.

- The axial deformation increased with higher stress level for all specimen.

- The final axial deformation $\varepsilon_{a_{\max}}$ stabilized between 1 and 2 mm for all specimen except B3. No increase in axial deformation was measured during thermal consolidation.

	ID	$\sigma_1 \approx \sigma_v'$	$\sigma_3 \approx \sigma_h'$	(I) $\Delta V_{\max}$	(II) $\Delta V_{\max}$	(III,IV) $\varepsilon_{a_{\max}}$
		[kPa]	[kPa]	[cm^3]	[cm^3]	[mm]
■	A1	78	55	3.0	1.5	1.3
●	A2	55	38	1.4	1.4	1.0
◆	A3	65	45	1.4	1.6	1.1
□	B1	78	54	1.3	-	1.8
○	B2	55	38	1.0	-	1.4
◇	B3	138	56	2.4	-	4.7
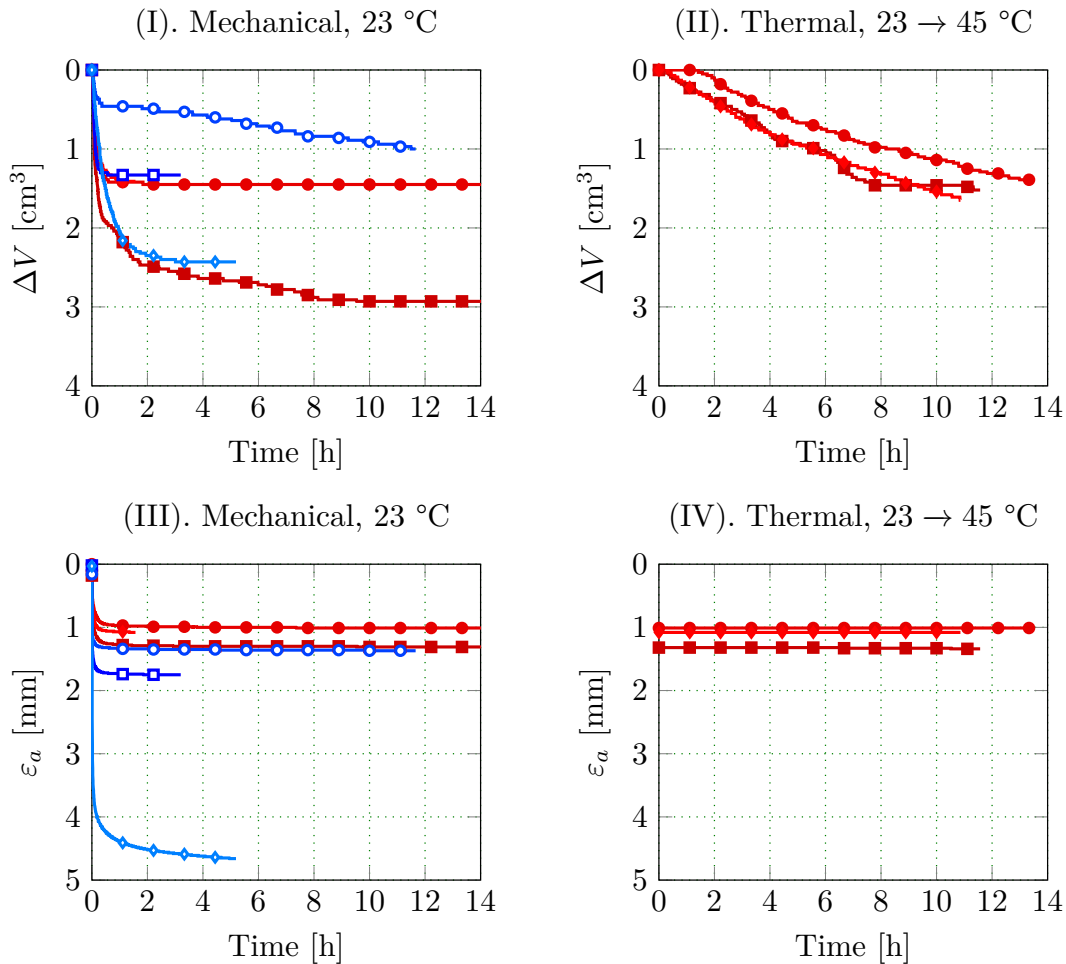
FIGURE 8.5: Anisotropic consolidation measurements for specimen following test program A and B. (I, II) displays the time - ΔV plots and (III, IV) shows the time - ε_a plots. The thermally-consolidated specimen in program A are shown in red color, while specimen at room temperature following program B are colored in blue.

Undrained shearing at different temperatures

Test conditions

After no more water expelled from the specimen during consolidation, the shearing phase was initiated. The drainage lines were closed, and the bottom pedestal was lifted with a motorized rate of $\varepsilon_a = 1$ mm/hour untill $\varepsilon_a = 14$ mm. The required load P and σ_3 were recorded every 10th second. The temperature was held at room temperature ≈ 23 °C for program B, while the temperature ≈ 45 °C for the thermally-consolidated specimen in program A. The temperature and stress conditions are shown in Figure 8.6.

$$\sigma_1 = \sigma_3 + P(1 - \varepsilon_a)/A_a$$
$$\sigma_3 = \sigma_c$$
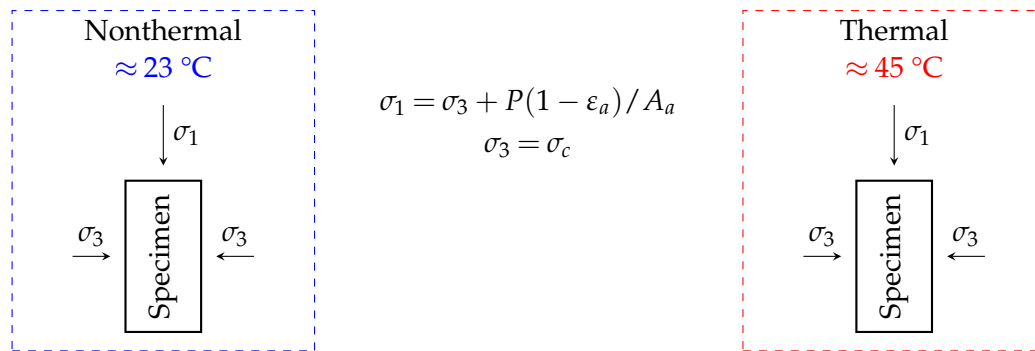
FIGURE 8.6: Simple sketches of the stress and temperature conditions during nonthermal undrained shearing for test program B to the left and thermal undrained shearing for test program A.

Deviatoric stress q and pore pressure u

Figure 8.7 shows the results of deviatoric stress $q = \sigma_1 - \sigma_3$ and pore pressure u with increased axial deformation ε_a during nonthermal and thermal undrained shearing. The following was expressed:

- The peak deviatoric stress q_{max} is rather similar despite the change in temperature.

- A significant difference is seen in the post-failure behavior, in which the room tempered deviatoric stress tend to drop faster and with an increased downward incline. For example, A2 and B2 had approximately the same q_{max}, but at finished deformation the A2 deviatoric stress > B2 deviatoric stress.

- A higher radial consolidation stress σ_3 corresponds with a higher deviatoric stress q for all specimen. Examining A1 and A3, the behavior is very similar despite the change in σ_1.

- The axial deformation at failure ε_{a_f} is rather similar despite the change in temperature. B3 deviated from this, but had slightly different consolidation stresses than the other specimen due to a previously mentioned error.

- The thermally-sheared specimen exhibit lower pore pressures than the room tempered specimen. Generally, the pore pressure increases up to failure before flattening out and increasing again some time after.

- The pore pressure response seem to be dependent on σ_1. Higher σ_1 caused an increase in pore pressure during shearing.

- Specimen A3 did not develop pore pressures.

- Young's modulus at 50 % of q_{max} were relatively equal, but A3 had a higher value.

	ID	$\sigma_3 = \sigma_c$	(I,II) q_{max}	(I,II) ε_{a_f}	(I,II) E_{50}	(III,IV) u_{max}
		[kPa]	[kPa]	[mm]	[MPa]	[kPa]
■	A1	55	111	1.8	97	32
●	A2	38	98	1.8	83	18
◆	A3	45	110	1.4	159	1
□	B1	54	119	1.6	66	33
○	B2	38	101	2.1	87	21
◆	B3	56	105	0.4	-	38

(I). Nonthermal, 23 °C

(II). Thermal, 45 °C

(III). Nonthermal, 23 °C

(IV). Thermal, 45 °C
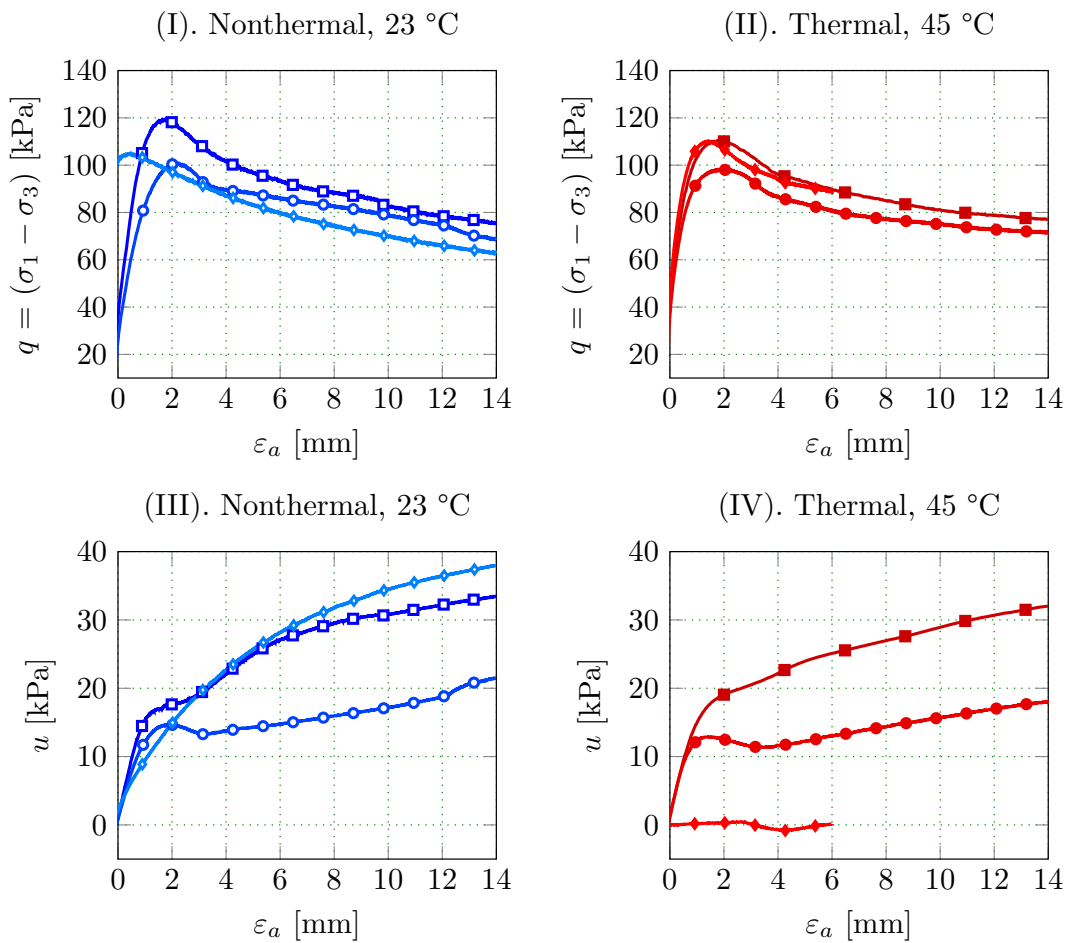
FIGURE 8.7: Deviatoric stress and pore pressure measurements during undrained shearing of anisotropic mechanically (+ thermally for program A) consolidated specimen. (I, II) shows the $\varepsilon_a - q$ plots and (III, IV) displays the $\varepsilon_a - u$ plots. The thermally-consolidated specimen in program A are shown in red color, while specimen at room temperature following program B are colored in blue.

Stress path and Mohr's circles

Figure 8.8 presents the stress path in the widely used $p' - q$ plot, where the mean effective stress $p' = \sigma_1' + 2 \cdot \sigma_3'$ and deviatoric stress $q = \sigma_1' - \sigma_3'$ in a triaxial compression test. The critical state line (CSL) had similar slope $M = 1.5$ for both test programs. Specimen A3 deviated from this because no pore pressures were measured. The frictional angle at critical state ϕ_{cs}' was:

$$M = \frac{6 \sin \phi_{cs}'}{3 - \sin \phi_{cs}'} \Rightarrow 1.5 = \frac{6 \sin \phi_{cs}'}{3 - \sin \phi_{cs}'} \Rightarrow \arcsin \phi_{cs}' = \frac{4.5}{7.5} \Rightarrow \phi_{cs}' = \underline{\underline{37°}} \quad (8.1)$$

ID	A1	A2	A3	B1	B2	B3
$\sigma_3 = \sigma_c$	55	38	45	54	38	56
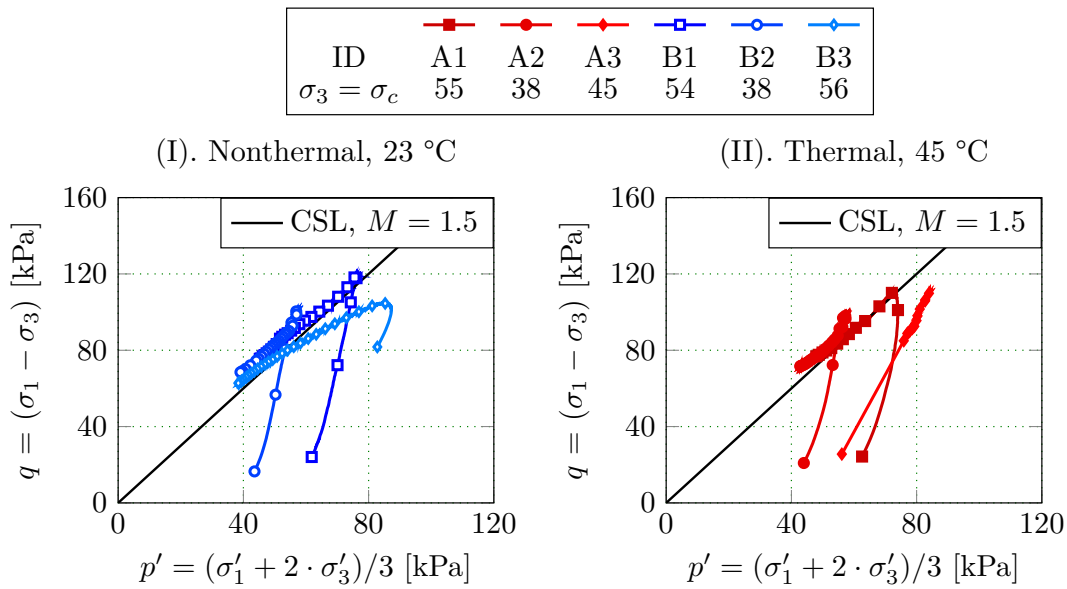
FIGURE 8.8: Stress paths of specimen A1 - A3 (I) and B1 - B3 (II) in the $p' - q$ plot.

The maximum shear stress $\tau = q_{max}/2$ and corresponding effective stress σ_1' & σ_3' were used to construct Mohr's circles shown in Figure 8.9. The linear failure envelope, known as the Mohr-Coulomb criterion $\tau = c' + \sigma_n' \tan \phi'$, was fitted to the results. Test program A obtained a frictional angle $\phi' = 20°$ and cohesion $c' = 25$ kPa. The room-tempered specimen in program B had a slightly lower cohesion $c' = 22$ kPa and a higher friction angle $\phi' = 24°$.
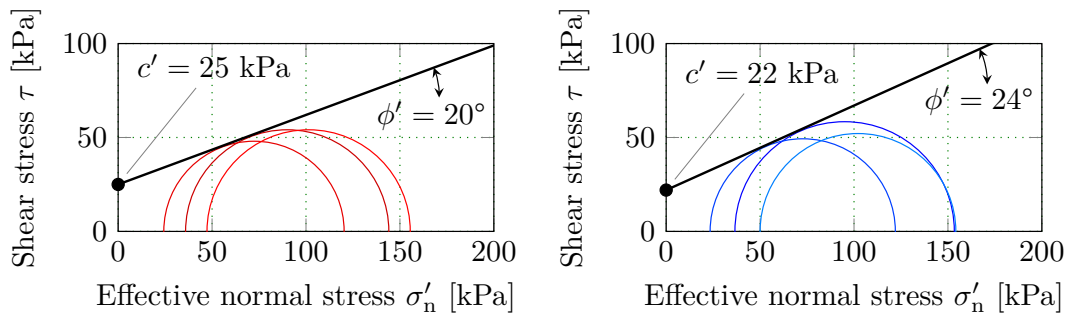
FIGURE 8.9: Mohr's circles with fitted Mohr-Coulomb failure criterion of specimen A1 - A3 (I) and specimen B1 - B3 (II).

8.4 Consolidated Isotropic Undrained Compression tests - program C and D

The results of the Consolidated Isotropic Undrained Compression (CIU$_c$) tests in program C (specimen C1 - C5) and D (specimen D1 - D3) are given in the following section. Detailed descriptions of the methodology of the test programs are in Section 5.3.

Isotropic mechanical and thermomechanical consolidation

Test conditions

Figure 8.10 illustrates the stress and temperature condition during mechanical and thermomechanical consolidation. Test program C featured mechanical consolidation at room temperature, while program D contained temperature elevated mechanical consolidation called thermomechanical consolidation. The temperature raise and consolidation stresses were applied *simultaneously* in program D (in contrast to program A). Expelled pore water ΔV and axial required load P were measured.
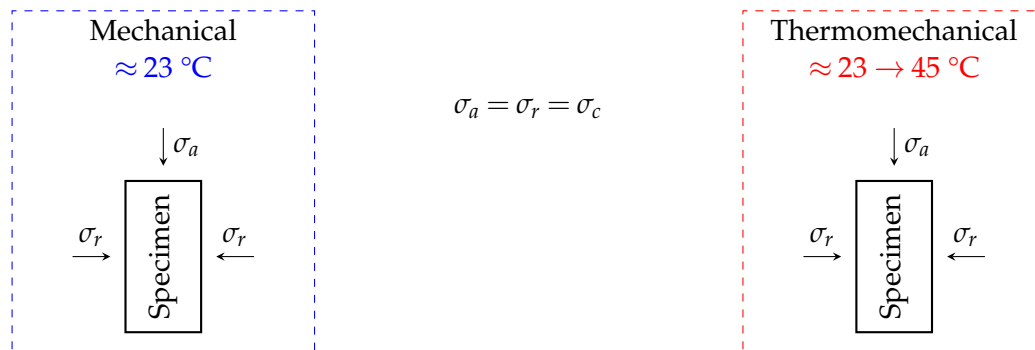
FIGURE 8.10: Simple sketches of the stress and temperature conditions during mechanical isotropic consolidation to the left and thermomechanical isotropic consolidation to the right.

Drained pore water ΔV and axial deformation ε_a

Figure 8.11 shows the time - ΔV and time - ε_a plots obtained by the CIUc tests in program C and D. They showed that:

- The thermomechanically expelled pore water increased with higher consolidation stress level. It seems that the opposite behavior is valid for the nonthermal program D, but too few measurements were carried out.

- Specimen D2 expressed deviating behavior from the rest of the specimen. The specimen did never stop expelling pore water. This could be explained by the isotropic pressure contributing to water flowing into the drainage lines via a fracture in the membrane.

- It is difficult to compare the mechanically- and thermomechanically-induced pore water because of lacking acceptable results in program D.

- The axial deformation decreased with higher isotropic consolidation stresses.

- Specimen consolidated with similar isotropic pressure but different temperature (e.g. C1 & D1 and C2 & D2) show unlike axial deformation behavior. The

thermomechanically-induced axial deformation exceeds the mechanical measurements.

- The necessary time for completed axial deformation $\varepsilon_{a_{\max}}$ was rather similar but seemed to be longer for thermomechanical specimen. More nonthermal tests are needed to ensure this behavior.

	ID	$\sigma_a = \sigma_r = \sigma_c$	(I,II) $\Delta V_{\max}$	(III,IV) $\varepsilon_{a_{\max}}$
		[kPa]	[cm^3]	[mm]
■	C1	300	18.4	1.9
●	C2	200	13.5	2.1
◆	C4	200	12.5	2.6
▲	C5	300	23.9	1.6
□	D1	300	19.7	1.0
◇	D2	200	148.3	1.6
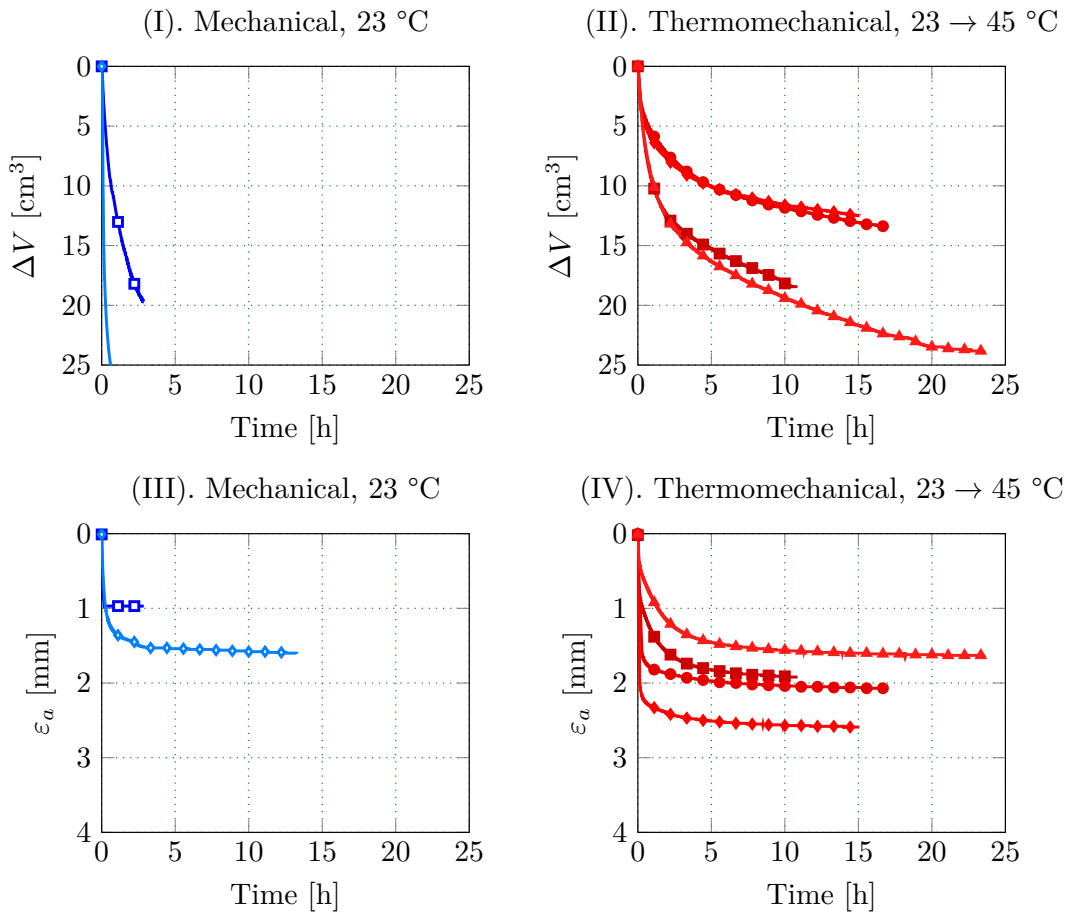
FIGURE 8.11: Isotropic consolidation for specimen following test program C and D. (I, II) displays the time - ΔV plots and (III, IV) shows the time - ε_a plots. The thermally-consolidated specimen in program C are shown in red color, while specimen at room temperature following program D are colored in blue.

Pore pressure u and axial deformation ε_a

The results of the specimen which were consolidated isotropic mechanically (D3) and isotropic thermomechanically (C3) with *closed* drainage lines are shown in Figure 8.12. The axial deformation ε_a and pore pressure u was measured in the test. The following can be deduced from the results:

- The nonthermal specimen D3 deformed more axially than C3. Also, D3 used longer time to reach peak axial deformation.

- The peak and initial pore pressure was higher for C3 than D3. C3 used longer time to reach peak pore pressure than D3.

ID	$\sigma_a = \sigma_r = \sigma_c$ [kPa]	(I) u_0 [kPa]	(I) u_{max} [kPa]	(II) $\varepsilon_{a_{max}}$ [mm]
C3	200	122	202	0.6
D3	200	40	136	1.1
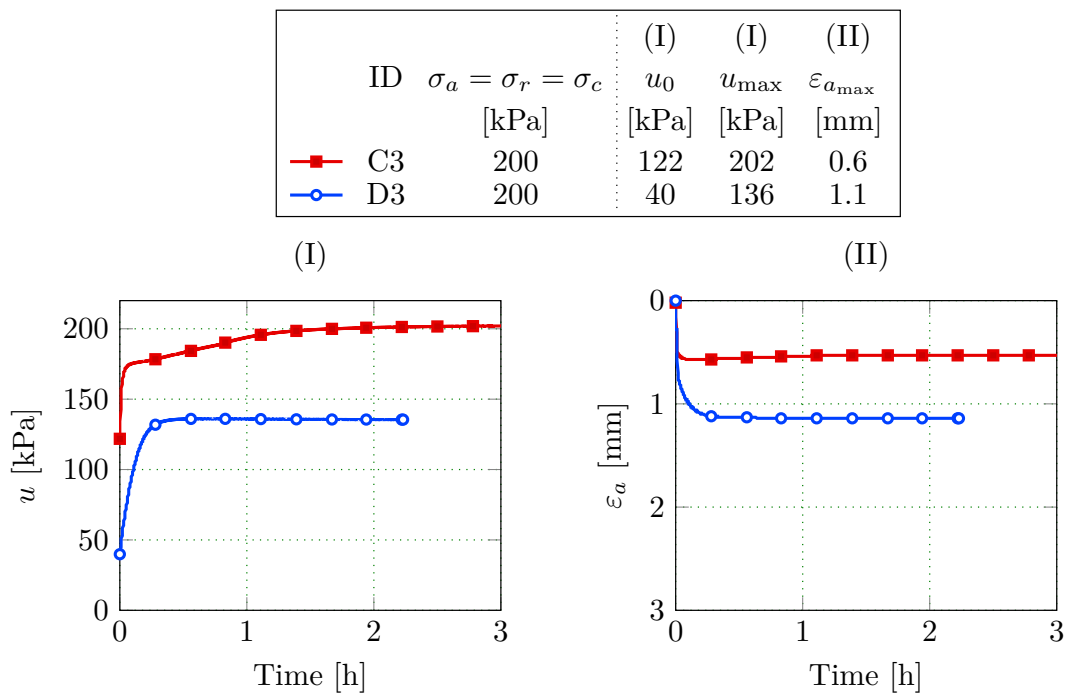
FIGURE 8.12: Undrained isotropic consolidation measurements for specimen following test program C and D. The thermally-consolidated specimen in C are shown in red color, while D at room temperature are colored in blue.

Undrained shearing at different temperatures

Test conditions

The temperature was held at the elevated temperature $\approx 45\,°C$ for program C, while room temperature $\approx 23\,°C$ applied for the mechanically consolidated specimen in D. It should be noted that C4 and C5 were unloaded to respectively 30 (OCR 10) and 50 (OCR 4) kPa before shearing. The temperature and stress conditions during shearing are shown in Figure 8.13.
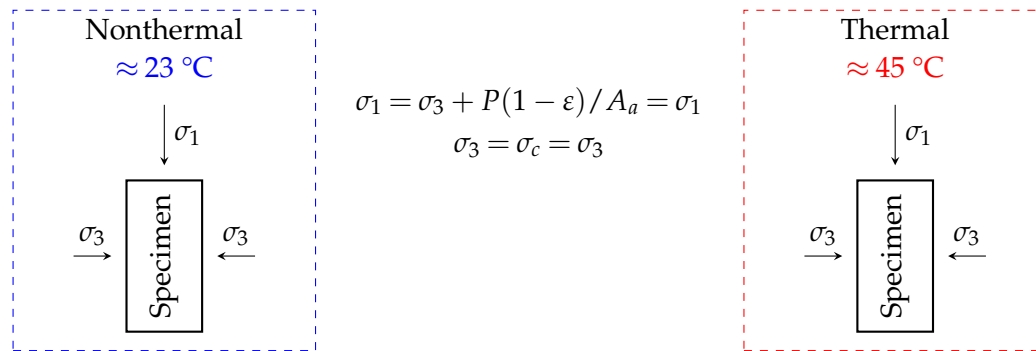
FIGURE 8.13: Simple sketches of the stress and temperature conditions during nonthermal undrained shearing for test program C to the left and thermal undrained shearing for test program D.

Deviatoric stress q and pore pressure u

Figure 8.14 shows the $\varepsilon_a - q$ and $\varepsilon_a - u$ plots obtained by nonthermal and thermal undrained shearing. The plots revealed that:

- The peak pore pressure was generally lower for thermal shearing.

- A clear difference in post-failure behavior is seen, in which the thermal deviatoric stress tend to drop less and with a decreased downward incline compared to the nonthermal specimen.

- The peak deviatoric stress was higher for the thermally sheared specimen as seen by comparison of C1 & D1 and C2 & D2.

- An increased confining stress σ_3 resulted in an increased peak deviatoric stress, pore pressure and axial deformation at failure for all specimen except C3.

- The unloaded specimen C4 and C5 exhibited low pore pressures.

- Young's modulus is rather similar despite the change in temperature.

	ID	$\sigma_3 = \sigma_c$	(I,II) $q_{\max}$	(I,II) ε_{a_f}	(I,II) E_{50}	(III,IV) $u_{\max}$
		[kPa]	[kPa]	[mm]	[MPa]	[kPa]
■	C1	300	228	5.6	99	221
●	C2	200	159	2.8	167	157
◆	C3 (U)	200	1	0.3	-	37
▲	C4	50	117	2.3	148	24
✕	C5	30	85	1.6	170	15
□	D1	300	160	3.9	195	258
○	D2	200	140	2.5	191	174
◇	D3 (U)	200	131	2.1	166	173

(I). Nonthermal, 23 °C

(II). Thermal, 45 °C

(III). Nonthermal, 23 °C

(IV). Thermal, 45 °C
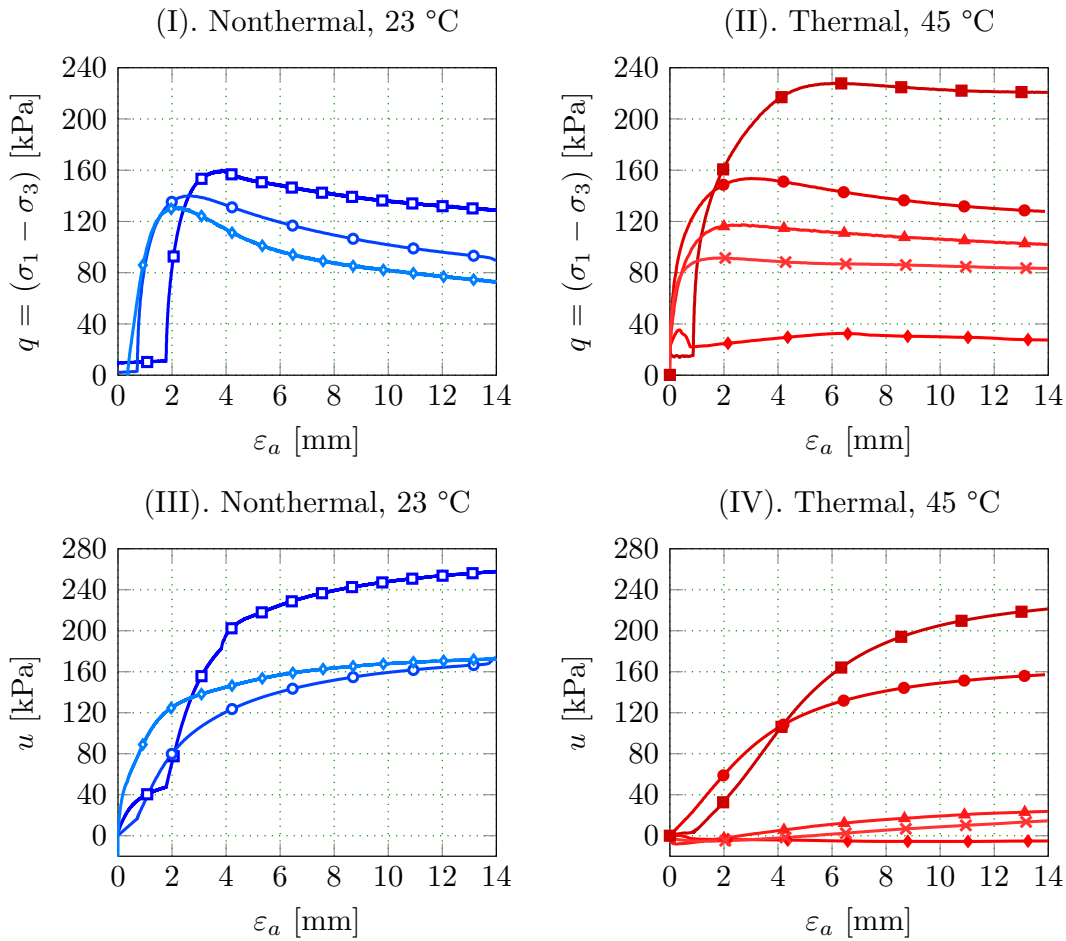
FIGURE 8.14: Deviatoric stress and pore pressure measurements during undrained shearing of isotropic mechanically consolidated specimen (+ thermomechanically for program C. (I, II) shows the $\varepsilon_a - q$ plots and (III, IV) displays the $\varepsilon_a - u$ plots. The thermally-consolidated specimen in program C are shown in red color, while specimen at room temperature following program D are colored in blue.

Stress path and Mohr's circles

Figure 8.15 presents the stress path in the $p' - q$ plot. The critical state line (CSL) had similar slope $M = 1.5$ for test program C and D. The frictional angle at critical state ϕ'_{cs} was:

$$M = \frac{6\sin\phi'_{cs}}{3 - \sin\phi'_{cs}} \Rightarrow 1.5 = \frac{6\sin\phi'_{cs}}{3 - \sin\phi'_{cs}} \Rightarrow \arcsin\phi'_{cs} = \frac{4.5}{7.5} \Rightarrow \phi'_{cs} = \underline{\underline{37°}} \quad (8.2)$$

ID	C1	C2	C3 (U)	C4	C5	D1	D2	D3 (U)
$\sigma_3 = \sigma_c$	300	200	200	50	30	300	200	200

(I). Nonthermal, 23 °C   (II). Thermal, 45 °C
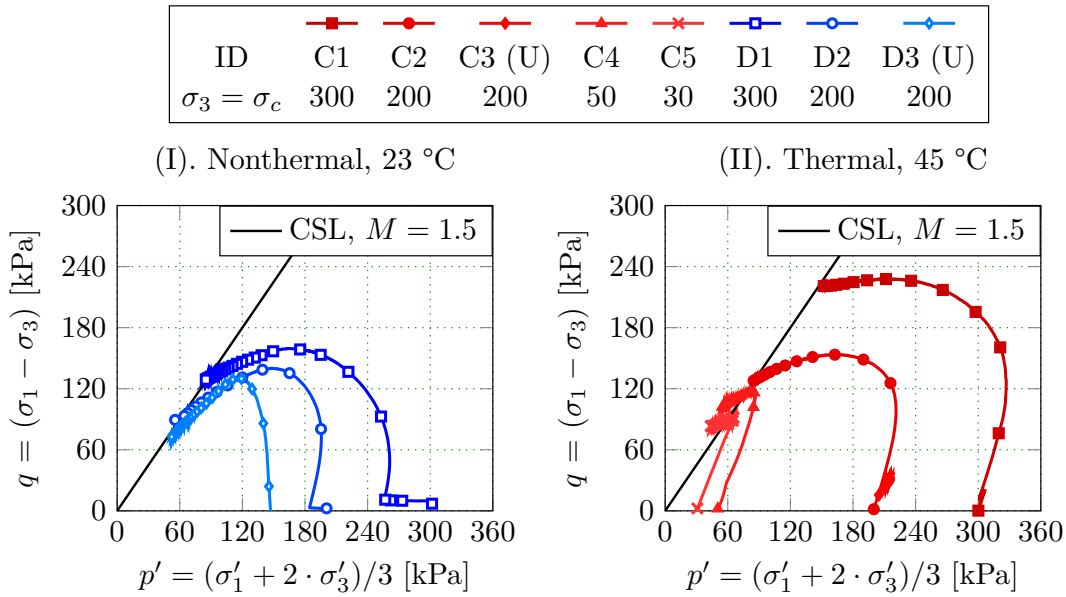
FIGURE 8.15: Stress paths of specimen C1 - C5 (I) and D1 - D3 (II) in the $p' - q$ plot.

The maximum shear stress $\tau = q_{max}/2$ and corresponding effective stress σ'_1 & σ'_3 were used to construct Mohr's circles shown in Figure 8.16. The Mohr-Coulomb criterion $\tau = c' + \sigma'_n \tan\phi'$ was fitted to the results. Test program C obtained a frictional angle $\phi' = 19°$ and cohesion $c' = 25$ kPa. The room-tempered specimen in program D had a higher cohesion $c' = 32$ kPa and a lower friction angle $\phi' = 14°$.
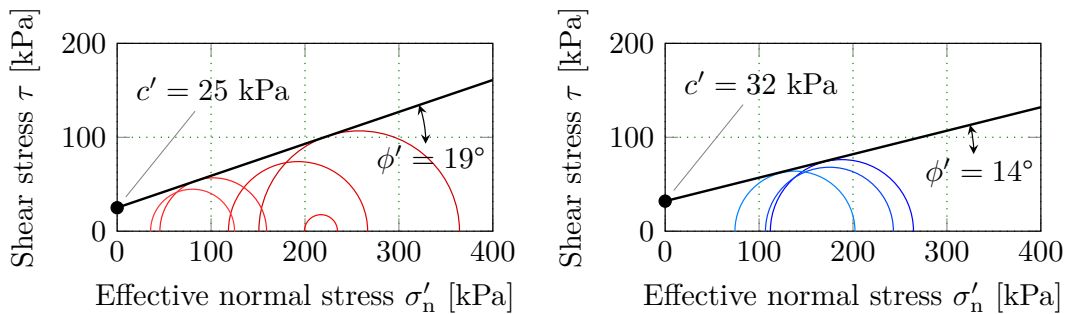
FIGURE 8.16: Mohr's circles and fitted Mohr-Coulomb failure criterion of specimen C1 - C5 (I) and specimen D1 - D3 (II).

..

Chapter 9

Micro-CT

The 3D images of the micro-CT specimen (S1 - S3 and S5 - S7) are presented in this chapter. The quadratic frame in all Figures defines the edge of the respective specimen while the internal red or blue colored structures are low density areas which represent cracks or cavities. All non-heated specimen are visualized in blue color while all heated specimen have red color.

9.1 Specimen 1

Figure 9.1 shows the 3D model of specimen 1 before heating. Two cracks are seen, in which one is more significant than the other. This significant crack is directed north west - south east and is located near the top of the specimen. The small dots, especially visible in Figure 9.1 (I), reflect on minor cavities.

(I) Top view. (II) 3D view.
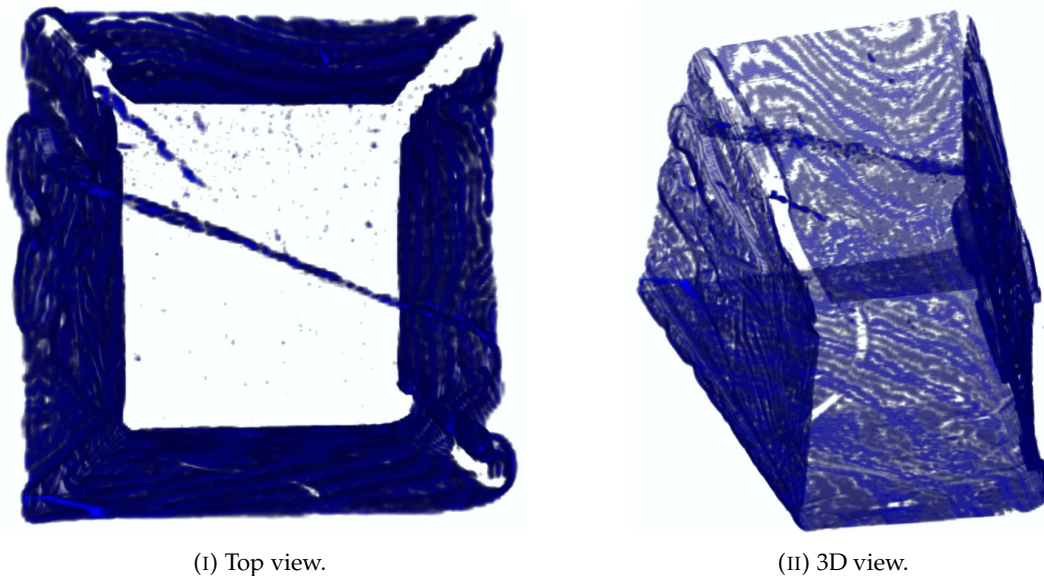
FIGURE 9.1: Specimen 1 (S1) visualized before heating.

The 3D model after the specimen was heated to 105 °C is presented in Figure 9.2. Three dominant cracks are seen with a similar north west - south east direction. One crack is located near the top and two at the bottom of the specimen. Contrary to the pre-existing cracks, these cracks are different in shape with distinct mini cracks showing perpendicular to the main direction. Also, more minor cavities are seen.

(I) Top view.   (II) 3D view.
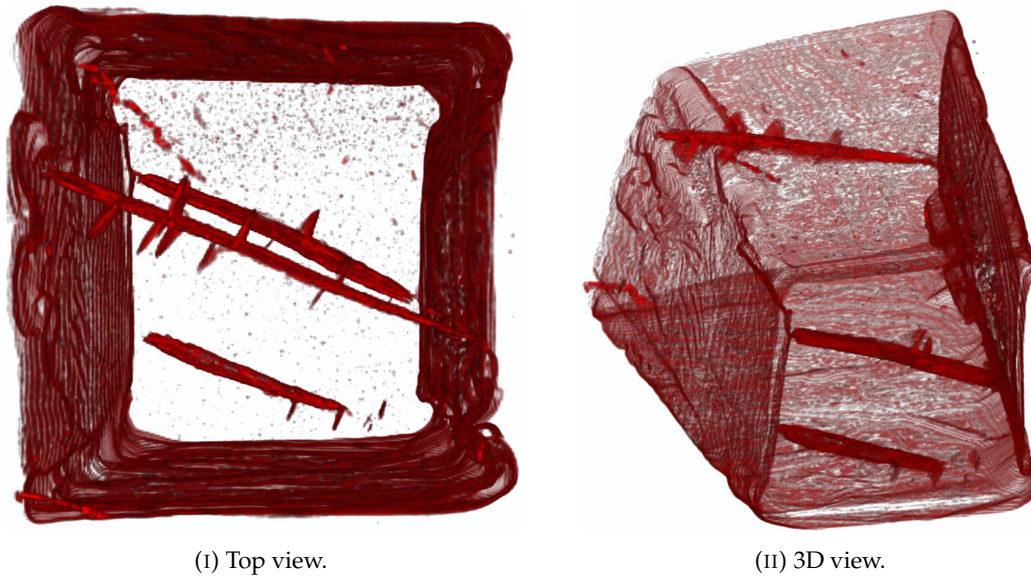
FIGURE 9.2: Specimen 1 (S1) visualized after heating to 105 °C.

9.2   Specimen 2

Figure 9.3 shows the 3D model of specimen 2 before heating. Various internal structures are seen including one significant crack directed north west - south east (most visible in Figure 9.3 (II)). The other internal structures indicate a notable amount of pre-existing cavities.

(I) Top view.   (II) 3D view.
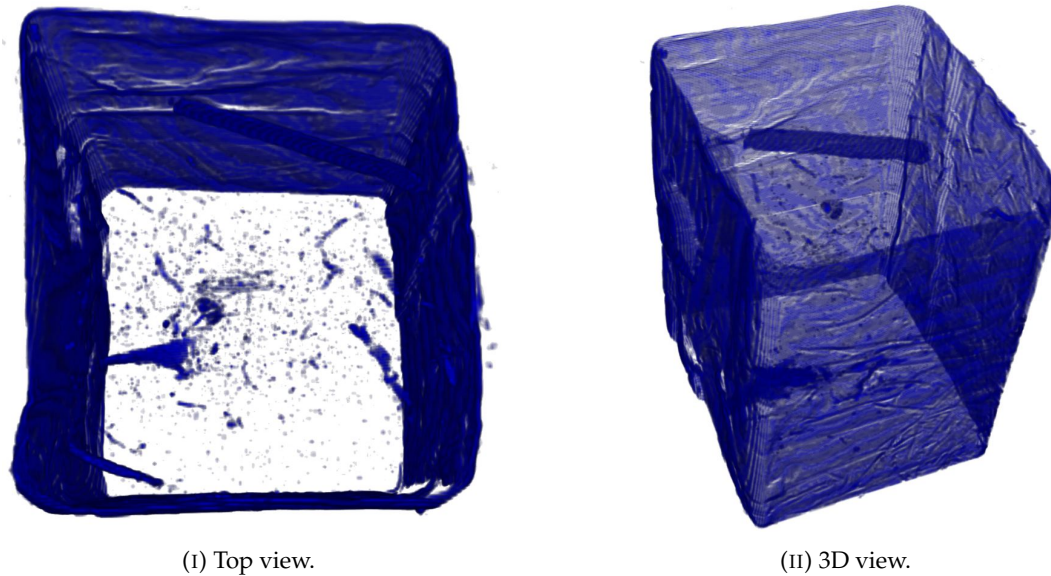
FIGURE 9.3: Specimen 2 (S2) visualized before heating.

Post heating, the specimen is visualized in Figure 9.4. Examining the pre-existing crack, it is seen that three mini cracks were developed perpendicular to the main direction. Also two more cracks were generated in addition to two ellipse-shaped cavities located in the middle of the specimen. The new cracks had similar direction as the pre-existing.

(I) Top view.   (II) 3D view.
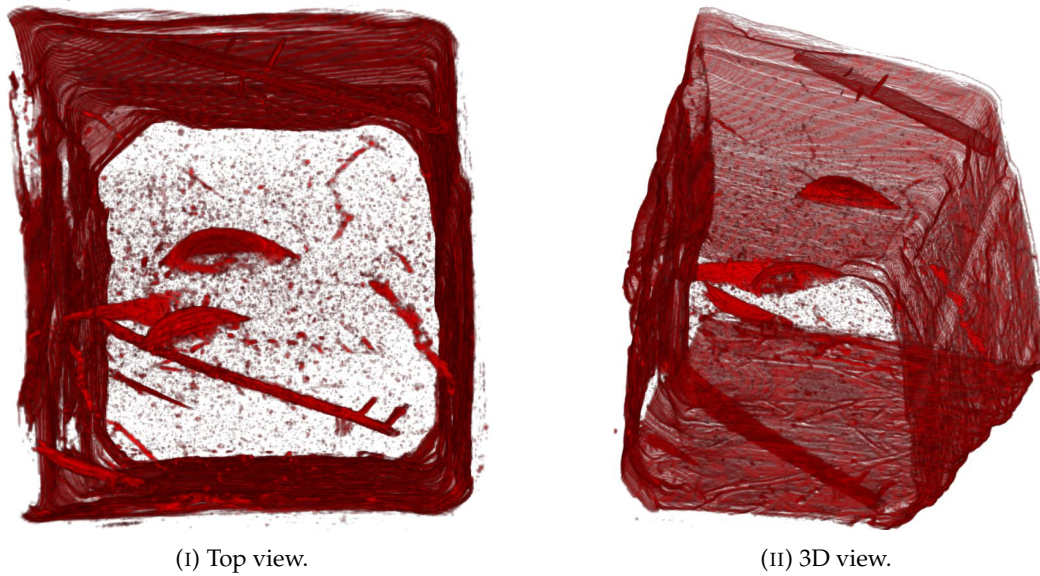
FIGURE 9.4: Specimen 2 (S2) visualized after heating to 105 °C.

9.3 Specimen 3

The micro-CT results of specimen 3 before heating is shown in Figure 9.5. Two major cracks are seen with a north west - south east direction (with unlike angles). The cracks are especially visible in Figure 9.5 (II). Furthermore, two ellipse-shaped cavities are showing in between the two cracks. The many small dots reflects on minor cavities.

(I) Top view.   (II) 3D view.
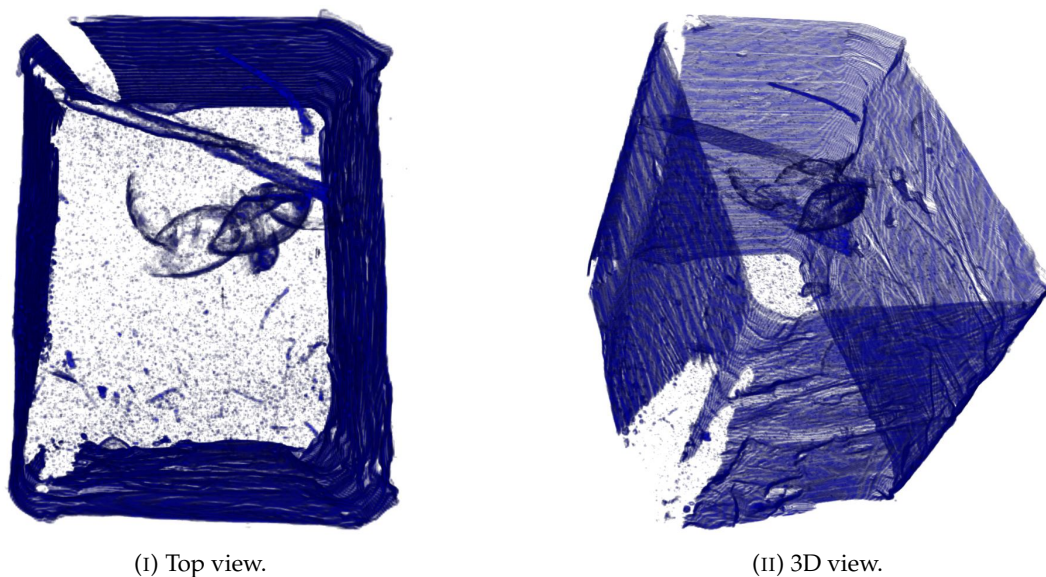
FIGURE 9.5: Specimen 3 (S3) visualized before heating.

After heating to 105 °C, the pre-existing cracks and cavities were expanded as seen in Figure 9.6. Heating extended pre-existing structures in the *z* direction. Only one minor crack was generated near the bottom of the specimen.

(I) Top view.

(II) 3D view.
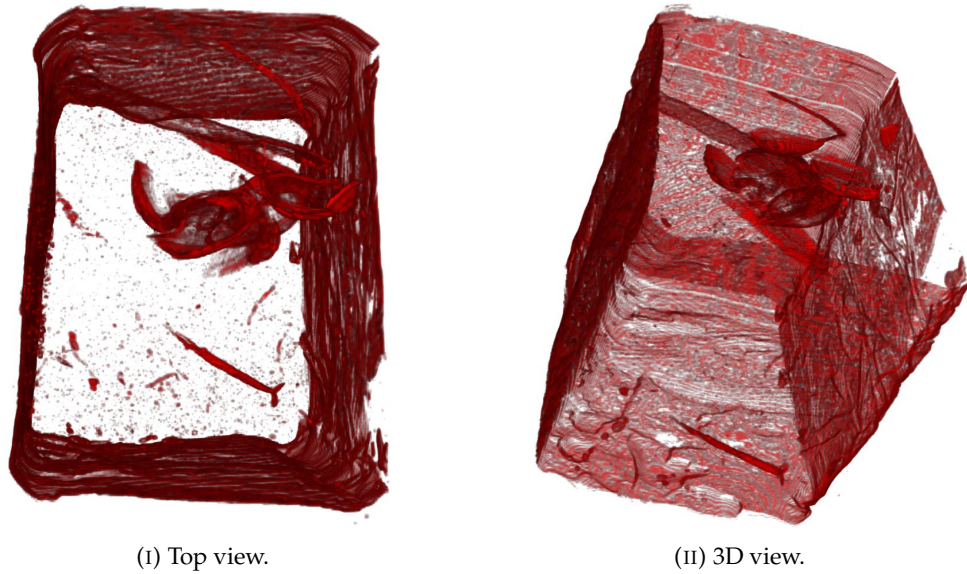
FIGURE 9.6: Specimen 3 (S3) visualized after heating to 105 °C.

9.4 Specimen 5 - 7

The results of the specimen which were heated to 70 °C and scanned only once are shown in Figure 9.7. Since the specimen were not scanned before heating, these results are less emphasized due to the fact that it is unclear if the obtained cracks and cavities were temperature-induced or already existing. However, all specimen show cracks shaped like the temperature-induced cracks for S1 and S2 which reflects on a temperature effect.

(I) Top view of S5.

(II) Top view of S6.

(III) Top view of S7.

(IV) 3D view S5.

(V) 3D view of S6.

(VI) 3D view of S7.

FIGURE 9.7: Specimen 5 - 7 (S5 - S7) visualized after heating to 70 °C.

Chapter 10

Discussions

This chapter discusses the experimental results in light of the findings from the literature review. The effects of elevated temperature on volumetric deformation (thermal consolidation), pore pressure, shear strength parameters, stress-strain behavior and Young's modulus are discussed.

10.1   Thermal consolidation

As discussed in the literature review, a temperature-induced compression effect called thermal consolidation was expected during heating. The effect was proven in drained heating tests in triaxial test program A, whereas specimen A1 - A3 expelled additional pore water. The amount of mechanically- and thermally-induced pore water was rather similar. This indicates a significant consolidation effect caused by temperature. It must be noted that the mechanical measurements were influenced by remains of water in the drainage lines on beforehand originating from flushing. An assumption was made that the measurements during the first 2 minutes of all mechanical (and thermomechanical) consolidation tests were influenced, and they were consequently subtracted. This correction may have caused artificially low measurements of ΔV. Furthermore, water expelled more slowly during thermal consolidation which reflects on a slower consolidation process. This can be caused by the thermal consolidation actually being slower or because of the gradual increase of specimen temperature. Also, no increase in axial deformation ε_a was measured during thermal consolidation, indicating that the specimen deformed radially.

The calculated thermal strain $\varepsilon_v{}^T$ for specimen A1 - A3 by the Campanella & Mitchell (1968) relationship (see Appendix D) can be added to the $I_P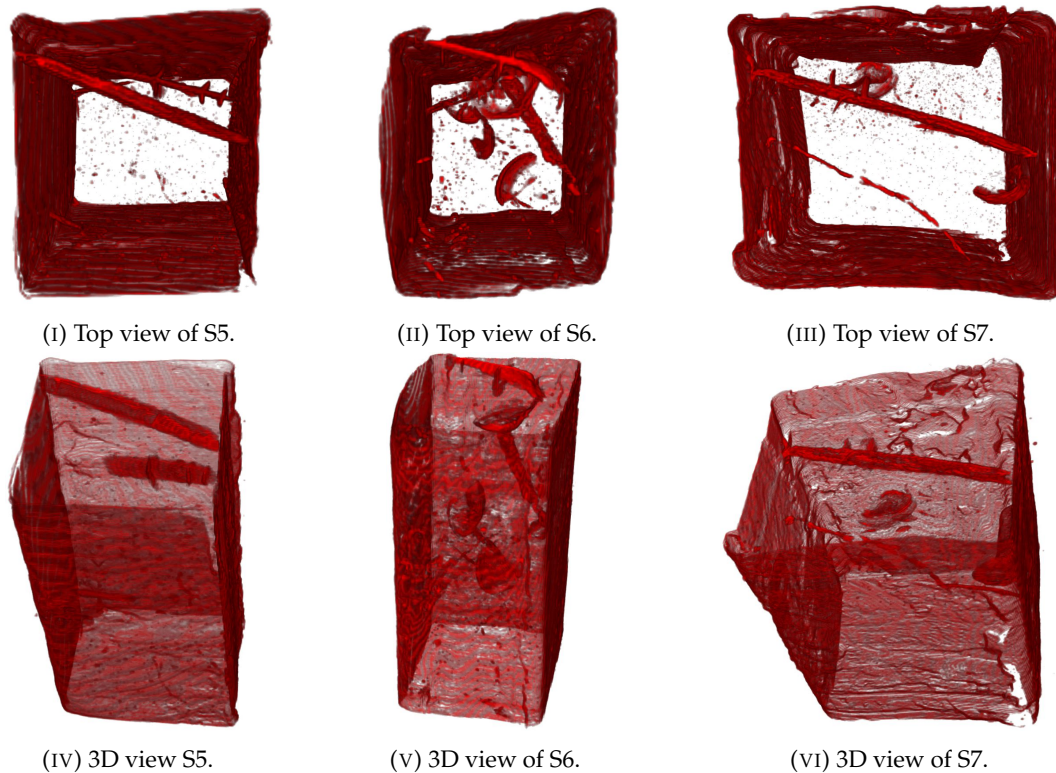$ - $\varepsilon_v{}^T$ plot shown in Figure 3.2. The results including quick clay are replotted in Figure 10.1. As seen in the revised plot, the obtained thermal strain has an expected value in relation to the other clay types in which a higher plasticity index gives more thermal strain. The plasticity index relates to the intensity of the physio-chemical interactions as discussed in the literature review.

The isotropic thermomechanical consolidation results were harder to interpret due to uncertainty related to what effects that were actually initiated by elevated temperature because of lacking results in the comparable program, and the fact that mechanical and thermomechanical consolidation happened *simultaneously*. Ideally, more specimen should have been added to test program D for a better basis of comparison. Regardless, there was a clear trend in the thermomechanical plots that a higher stress level corresponded to more expelled water and less axial deformation.

Since the general trend was that the thermomechanically-induced axial deformation exceeded the mechanically-induced axial deformation for specimen consolidated with similar stress condition, it can be argued from the former inverse relation that the thermomechanical specimen expelled less water. This can also be interpreted by comparison of D1 and C1 in Figure 8.11. An explanation to this can be that the additional temperature-induced axial deformation contributed to a more compact structure with decreased permeability resulting in less water flow.

No tests were performed to investigate the effect of stress history. It would have been interesting to consolidate the specimen in two steps with a reduction of pre-consolidation pressure followed by drained heating and compare the results with Figure 3.3.

□ MC (Towhata et al., 1993)	○ Boom (Del Olmo et al., 1996)
△ Illite (Graham et al., 2001)	◇ Boom (Sultan et al., 2002)
× MC (Laloui & Cekerevac, 2003)	⋆ Bangkok (Abuel-Naga, 2006)
⬟ Quick clay (this study)	
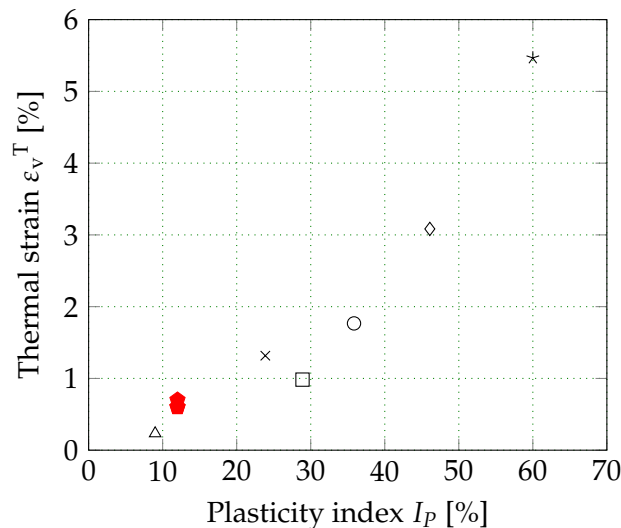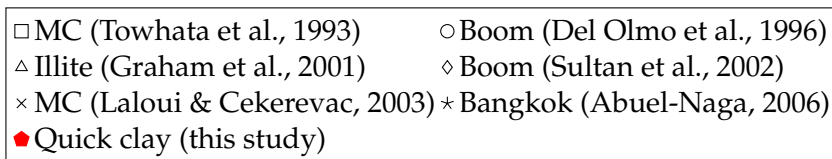
FIGURE 10.1: Plasticity index and temperature induced volumetric strain of some normally consolidated clays reported in literature ($\Delta T \approx 70\ °C$ and $T_0 \approx 20\ °C$). Modified from Abuel-Naga (2006). Calculated thermal strain for quick clay is marked in red color.

10.2 Pore pressure generation

The two undrained heating tests, in Figure 8.12, showed that the peak temperature-induced pore pressure was higher. This was in accordance to the theory explaining that heating induces pore pressure due to the differential expansion of water and solids. There is uncertainty related to the initial pore pressure measurement due to it being influenced by the remains of water in the drainage lines from flushing. As seen in Table 10.1 there is large variation in the values of u_0. Nevertheless, an attempt of adding the excess pore pressure Δu for C3 in the pore pressure - temperature plot by Ghaaowd et al. (2015) is shown in Figure 10.2. Compared to other clay types with similar change in temperature, quick clay exhibited slightly more excess pore pressure than the average value.

TABLE 10.1: Varying values of the initial pore pressure u_0 during consolidation.

ID	D1	D2	D3	C1	C2	C3	C4	C5
u_0 [kPa]	23	18	40	30	184	121	116	22

□ Remoulded Illite (σ_3 = 196 kPa) ○ Smectite (σ_3 = 98 kPa)
△ Illite (σ_3 = 98 kPa) ◇ Illite (σ_3 = 29 kPa)
× Bangkok (σ_3 = 200 kPa) ⋆ Bangkok (σ_3 = 300 kPa)
⊗ Bangkok (σ_3 = 400 kPa) ✳ Todi (σ_3 = 196 kPa)
⊕ Flumicino (σ_3 = 147 kPa) + Newfield (σ_3 = 275 kPa)
⬟ Quick clay (σ_3 = 200 kPa)
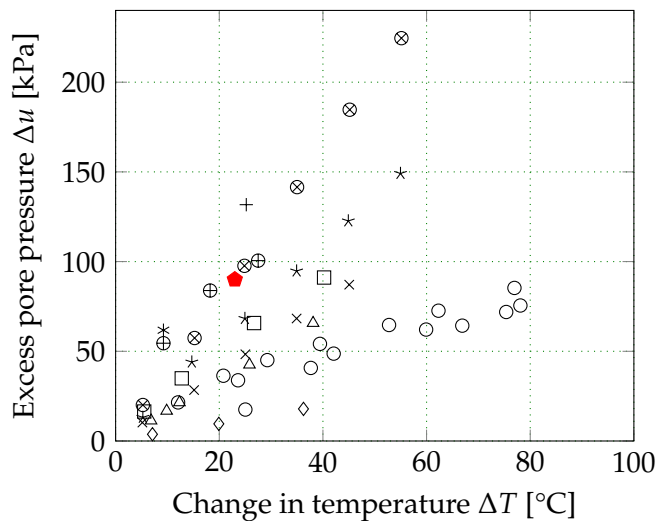
FIGURE 10.2: Effect of temperature on the change in pore water pressure for soil specimen. Modified from (Ghaaowd et al., 2015). Quick clay is added in red color.

The results of the micro-CT scans showed that more internal cracks and cavities were induced by heating. An explanation to this can be that higher pore pressures induce more water flow which contributes to creation and expansion of cracks. The fact that most cracks were similarly directed reflects upon the specimen being weaker in that direction.

10.3 Shear strength

For comparison with the results obtained by Abuel-Naga (2006), the undrained shear strength behavior of isotropic consolidated quick clay to 200 and 300 kPa is plotted in Figure 10.3. The measurements are normalized with the respective consolidation stresses as carried out in Figure 3.6. Comparing Figure 3.6 and 10.3, the similar trend is seen in which the peak deviatoric stress increases with elevated temperature. As proposed by Abuel-Naga (2006) this happens because of the occurrence of more thermal consolidation which makes the specimen more compact and thus raising the shear strength. During thermal consolidation more pore pressures have dissipated which shows on the lowered pore pressure measurements during shearing.

The effective shear strength parameters c' and ϕ' varied between the test programs. The obtained values by thermal shearing (program A and C) are very similar as $c' = 25$ kPa and $\phi' = 19°$ and $20°$. Contrary, the results of program B and D are unlike. There was uncertainty related to the line fitting of program D due to lacking measurements. Therefore, the obtained parameters by program B ($c' = 22$ kPa and $\phi' = 24°$) are emphasized. By comparison of the results of program B and A & C, the cohesion c' increases and frictional angle ϕ' decreases with an increased temperature. However, more tests are needed to validate these results.
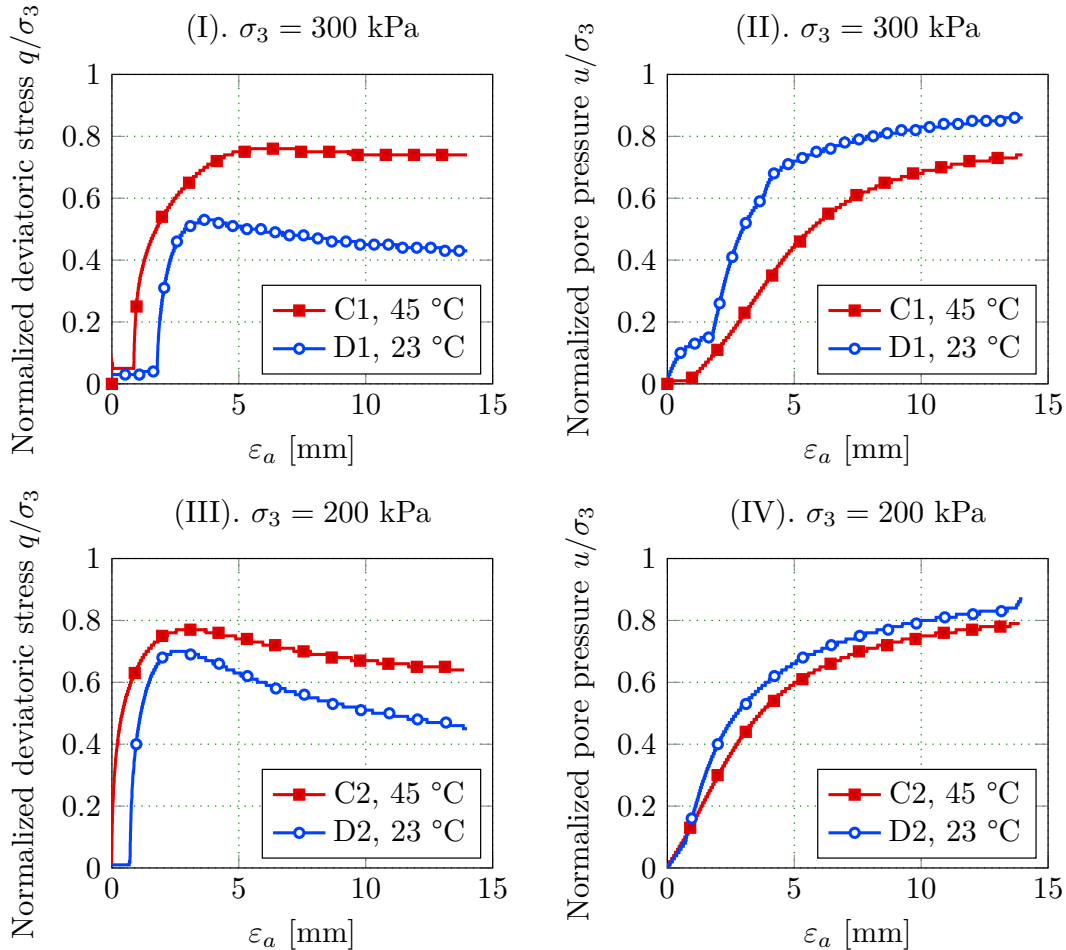
FIGURE 10.3: Normalized deviatoric stress (I,III) and normalized pore pressure (II,IV) plots of the specimen with similar consolidation conditions - C1 & D1 and C2 & D2.

The clear difference in post-failure behavior by temperature was shown by both comparison of program A & B and C & D. The thermally-sheared specimen exhibited a higher shear strength at post-failure strains, showing a more ductile mechanical behavior. Also, the effect was more important for thermally-sheared specimen consolidated to higher stress levels. At large strains, when the critical state is reached, the deviatoric stress seems to drop to a rather similar residual strength level. Therefore, the similar slope of the critical state line (CSL) was obtained for all test programs despite the change in temperature, indicating that the CSL is independent of temperature. This correlates with the results obtained by previous research in Figure 3.8. The CSL of quick clay is added to the former plot, and replotted in Figure 10.4. It should be mentioned that uncertainty is related to the line fitting because no drained

shearing tests were carried out for plotting in the (v, p') space. Therefore, it is unclear if the term $\partial v / \partial \varepsilon_s$ is satisfied. Also, tests should be carried out at strains larger than 14 mm to ensure the behavior.
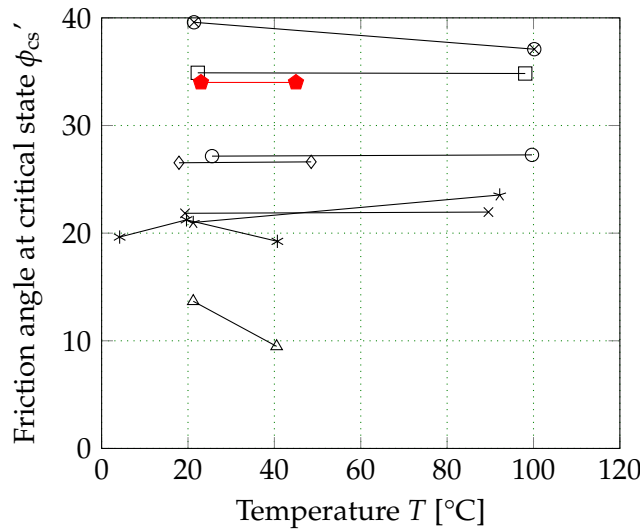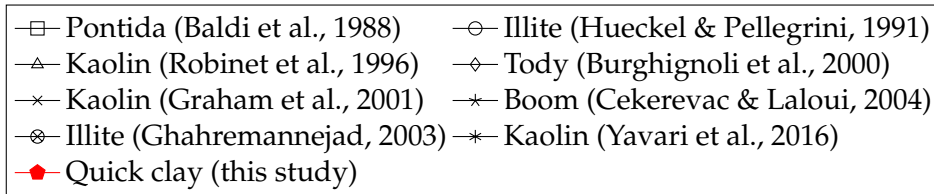
FIGURE 10.4: Change in frictional angle at critical state ϕ'_{cs} with temperature for some clay types. Modified from (Wang et al., 2020). Quick clay is added in red color.

Young's modulus

The mean value, standard deviation and number of issues for the Young's modulus E_{50} are shown in Table 10.2. Only the comparable specimen with similar stress conditions but different temperature are included in this analysis (A1 & B1, A2 & B2, C1 & D1, C2 & D2). A statistical two-tailed t test can be used to test the difference of means.

TABLE 10.2: Input parameters for the two-tailed t test.

	Mean x	Standard deviation	n
Young's modulus E_{50} at 45 °C [MPa]	111.5	37.7	4
Young's modulus E_{50} at 23 °C [MPa]	117.8	49.2	4

The difference between the two data sets is considered to be statistically insignificant (two-tailed P value = 0.85). Therefore, no difference in Young's modulus E_{50} has been observed despite the change in temperature.

Chapter 11

Conclusions

The goal of this master's thesis work was to obtain knowledge on how the thermo-mechanical properties of Norwegian quick clay are affected by increased temperature. Nearly all objectives were met through the construction of a temperature-modified cell using a self-produced heating sleeve, triaxial tests carried out in this apparatus and the performed micro-CT scans. Drained shearing was not carried out due to limited time. Based on the results of the laboratory investigations, the following conclusions were drawn:

- Volumetric deformation occurs upon heating. The low plasticity of quick clay decreases the intensity of physico-chemical reactions which lower the amount of thermal volumetric deformation compared to other clay types.

- Excess pore pressure is generated by increased temperature. This pore pressure contributes to formation of new cracks as well as expanding pre-existing cracks. All cracks were similarly orientated. The temperature-induced cracks had minor protrusions occuring perpendicular to the main crack direction.

- Peak shear strength increases with elevated temperature. This happens because of the occurrence of thermal consolidation which makes the specimen more compact by dissipation of pore pressures and accordingly raising the shear strength.

- Higher temperatures induce a more ductile mechanical behavior.

- The critical state line, expressing the remoulded shear stress state at large strains, is independent of temperature.

- No change in Young's modulus E was observed despite the change in temperature.

- More tests are needed to clarify the effect of temperature on the effective cohesion c' and effective frictional angle ϕ'.

Chapter 12

Future recommendations

Future investigations are needed to validate the conclusions that were drawn in this study. In addition to carrying out more tests with similar methodologies, temperatures should be increased to higher levels for the triaxial tests. This requires the development of a new and better temperature-modified triaxial apparatus. It should be designed for better control of the specimen temperature, include the possibility of adding back pressure and allow application of temperatures all the way up to 100 °C. Also, future research could:

- Study the effect of stress history (OCR) on thermal consolidation and how the drained shear strength parameters change with temperature. Both tests can be performed in a temperature-modified triaxial apparatus.

- Investigate the temperature effect on the preconsolidation pressure using a temperature-modified oedometer apparatus. To achieve this, a such apparatus needs to be designed.

- Develop a thermomechanical constitutive model of quick clay.

- Apply the results for engineering purposes such as design of future Borehole Thermal Energy Systems (BTES).

- Study the thermo-hydro-mechanical properties of quick clay.

References

Abuel-Naga, H. M. 2006: Thermo-mechanical behavior of soft Bangkok clay : Experimental results and constitutive modeling. Ph.D. dissertation, Asian Institute of Technology.

Abuel-Naga, H. M., **Bergado, D. T.** & **Bouazza, A. 2007**: Thermally induced volume change and excess pore water pressure of soft Bangkok clay. In: *Engineering Geology*, 1(89) pp. 144–154.

Ashrafi, M. & **Hamidi, A. 2020**: Application of a thermo-elastoplastic constitutive model for numerical modeling of thermal triaxial tests on saturated clays. In: *Innovative Infrastructure Solutions*, 5(81).

Baldi, G., **Hueckel, T.** & **Pellegrini, R. 1988**: Thermal volume changes of mineral-water system in low-porosity clay soil. In: *Canadian Geotechnical Journal*, 25(4) pp. 807–825.

Brattli, B. 2018: Ingeniørgeologi Løsmasser Kompendium. NTNU, Institutt for geovitenskap og petroleum.

Bryhni, I. & **Hagen, J. O. 2020**: Siste istid. Store norske leksikon. Available at: `https://snl.no/siste_istid`.

Burghignoli, A., **Desideri, A.** & **Miliziano, S. 2000**: A laboratory study on the thermomechanical behaviour of clayey soils. In: *Canadian Geotechnical Journal*, 37(4) pp. 764–780.

Campanella, R. G. & **Mitchell, J. K. 1968**: Influence of Temperature Variations on Soil Behavior. In: *Journal of the Soil Mechanics and Foundations Division*, 94(3) pp. 709–734.

Cekerevac, C. & **Laloui, L. 2004**: Experimental study of thermal effects on the mechanical behaviour of a clay. In: *International Journal for Numerical and Analytical Methods in Geomechanics*, 28(3) pp. 209–228.

Cheng, W., **Hong, P.-Y.**, **Pereira, J.-M.**, **Cui, Y.-J.**, **Tang, A. M.** & **Chen, R.-P. 2020**: Thermo-elasto-plastic modeling of saturated clays under undrained conditions. In: *Computers and Geotechnics*, 125(103688).

Del Olmo, C., **Fioravante, V.**, **Gera, F.**, **Hueckel, T.**, **Mayor, J.** & **Pellegrini, R. 1996**: Thermomechanical properties of deep argillaceous formations. In: *Engineering Geology*, 41(1) pp. 87–102.

Demars, K. & **Charles, D. 1982**: Soil volume changes induced by temperature cycling. In: *Canadian Geotechnical Journal*, 19 pp. 188–194.

Denison, C., **Carlson, W. D.** & **Ketcham, R. A. 1997**: Three-dimensional quantitative textural analysis of metamorphic rocks using high-resolution computed X-ray

tomography: Part I. Methods and techniques. In: *Journal of Metamorphic Geology*, 15(1) pp. 29–44.

Di Donna, A. & **Laloui, L. 2015**: Response of soil subjected to thermal cyclic loading: Experimental and constitutive study. In: *Engineering Geology*, 190 pp. 65–76.

Emdal, A., **Gylland, A.**, **Amundsen, H. A.**, **Kåsin, K.** & **Long, M. 2016**: Mini-block sampler. In: *Canadian Geotechnical Journal*, 53(8) pp. 1235–1245.

Geological Survey of Norway: Superficial deposits - National Database. Available at: `https://geo.ngu.no/kart/losmasse/`.

Ghaaowd, I., **Takai, A.**, **Katsumi, T.** & **McCartney, J. 2015**: Pore water pressure prediction for undrained heating of soils. In: *Environmental Geotechnics*, 4(2) pp. 70–78.

Ghahremannejad, B. 2003: Thermo-Mechanical Behaviour of Two Reconstituted Clays. Ph.D. dissertation, University of Sydney.

Graham, J., **Tanaka, N.**, **Crilly, T.** & **Alfaro, M. 2001**: Modified Cam-Clay modeling of temperature effects in clays. In: *Canadian Geotechnical Journal*, 38(3) pp. 608–621.

Houston, S. L., **Houston, W. N.** & **Williams, N. D. 1985**: Thermo-Mechanical Behavior of Seafloor Sediments. In: *Journal of Geotechnical Engineering*, 111(11) pp. 1249–1263.

Hueckel, T. & **Borsetto, M. 1990**: Thermoplasticity of Saturated Soils and Shales: Constitutive Equations. In: *Journal of Geotechnical Engineering*, 116(12) pp. 1765–1777.

Hueckel, T. & **Pellegrini, R. 1991**: Thermoplastic Modeling of Undrained Failure of Saturated Clay Due to Heating. In: *Soils and Foundations*, 31(3) pp. 1–16.

ISO 17892-1:2014: Geotechnical investigation and testing — Laboratory testing of soil — Part 1: Determination of water content. Standard, International Organization for Standardization.

ISO 17892-12:2018: Geotechnical investigation and testing — Laboratory testing of soil — Part 12: Determination of liquid and plastic limits. Standard, International Organization for Standardization.

ISO 17892-4:2016: Geotechnical investigation and testing — Laboratory testing of soil — Part 4: Determination of particle size distribution. Standard, International Organization for Standardization.

ISO 17892-6:2017: Geotechnical investigation and testing — Laboratory testing of soil — Part 6: Fall cone test. Standard, International Organization for Standardization.

ISO 17892-9:2018: Geotechnical investigation and testing — Laboratory testing of soil — Part 9: Consolidated triaxial compression tests on water saturated soils. Standard, International Organization for Standardization.

Ketcham, R. A. 2018: X-ray Computed Tomography (CT). Available at: `https://serc.carleton.edu/msu_nanotech/methods/CT.html`.

Ketcham, R. A. & **Carlson, W. D. 2001**: Acquisition, optimization and interpretation of X-ray computed tomographic imagery: applications to the geosciences. In: *Computers & Geosciences*, 27(4) pp. 381–400.

Kuntiwattanakul, P., **Towhata, I.**, **Ohishi, K.** & **Seko, I. 1995**: Temperature Effects on Undrained Shear Characteristics of Clay. In: *Soils and Foundations*, 35(1) pp. 147–162.

Laloui, L. & **Cekerevac, C. 2003**: Thermo-plasticity of clays: An isotropic yield mechanism. In: *Computers and Geotechnics*, 30(8) pp. 649–660.

Laloui, L. & **François, B. 2009**: ACMEG-T: Soil Thermoplasticity Model. In: *Journal of Engineering Mechanics*, 135(9).

Li, Y. 2019: On the impact of temperature perturbations on the creep of sensitive clay. Ph.D. dissertation, Chalmers University of Technology.

Moritz, L. 1995: Geotechnical properties of clay at elevated temperatures. Tech. Rep. 47, Swedish Geotechnical Institute. Available at: `https://www.sgi.se/globalassets/publikationer/rapporter/pdf/sgi-r47.pdf`.

Moritz, L. & **Gabrielsson, A. 2001**: Temperature Effect on the Properties of Clay. In: Soft Ground Technology Conference. pp. 304–314. Noordwijkerhout, The Netherlands, May 28 - June 2, 2000.

NTNU Geotechnical division 2017: Geotechnics compendium - Field and Laboratory Investigations. NTNU.

Plum, R. L. & **Esrig, M. I. 1969**: Some Temperature Effects on Soil Compressibility And Pore Water Pressure. In: *Special Report - Highway Research Board*, 101. Available at: `https://onlinepubs.trb.org/Onlinepubs/sr/sr103/103-022.pdf`.

Ramstad, R. K., **Holmberg, H.**, **Bugge, L.** & **Riise, M. H. 2017**: Sluttrapport Fjell2020 konseptutredning miljøløsninger. Tech. rep., Asplan Viak. Rapport utført for Drammen Eiendom KF.

Robinet, J.-C., **Rahbaoui, A.**, **Plas, F.** & **Lebon, P. 1996**: A constitutive thermomechanical model for saturated clays. In: *Engineering Geology*, 41(1) pp. 145–169.

Schofield, A. & **Wroth, C. 1968**: Critical State Soil Mechanics. McGraw Hill. ISBN 978-0641940484.

Sultan, N., **Delage, P.** & **Cui, Y. 2002**: Temperature effects on the volume change behaviour of Boom clay. In: *Engineering Geology*, 64 pp. 135–145.

Taina, I. A., **Heck, R. J.** & **Elliot, T. R. 2008**: Application of X-ray computed tomography to soil science: A literature review. In: *Canadian Journal of Soil Science*, 88(1) pp. 1–19.

Towhata, I., **Kuntiwattanaku, P.**, **Seko, I.** & **Ohishi, K. 1993**: Volume Change of Clays Induced by Heating as Observed in Consolidation Tests. In: *Soils and Foundations*, 33(4) pp. 170–183.

Trani, L., **Bergado, D.** & **Abuel-Naga, H. 2010**: Thermo-mechanical behavior of normally consolidated soft Bangkok clay. In: *International Journal of Geotechnical Engineering*, 4(1) pp. 31–44.

Wang, L. Z., **Wang, K. J.** & **Hong, Y. 2016**: Modeling Temperature-Dependent Behavior of Soft Clay. In: *Journal of Engineering Mechanics*, 142(8).

Wang, S., **Zhang, K.**, **Wang, S.**, **Wu, W.**, **Zhang, D.** & **Kim, J. 2020**: Thermal-mechanical Behaviour of Saturated Soil: A Review Study. In: 26th European Young

Geotechnical Engineers Conference. pp. 29–40. Graz, Austria, September 11 - 14, 2018.

Xiong, Y., **Ye, G.-l.**, **Zhua, H.**, **Zhang, S.** & **Zhang, F. 2016**: Thermo-elastoplastic Constitutive Model for Unsaturated Soils. In: *Acta Geotechnica*, 11 p. 1287–1302.

Yang, S., **Schjetne, K.** & **Kvalstad, T. 2010**: Thermal-mechanical Behaviour of Saturated Soil: A Review Study. In: Proceedings of the Twentieth International Offshore and Polar Engineering Conference, vol. 2. pp. 493–499. Beijing, China, June 20 - 25, 2010.

Yao, Y. & **Zhou, A. 2013**: Non-isothermal unified hardening model: a thermo-elastoplastic model for clays. In: *Géotechnique*, 63(15) pp. 1328–1345.

Yavari, N., **Tang, A.-M.**, **Pereira, J.-M.** & **Hassen, G. 2016**: Effect of temperature on the shear strength of soils and soil/structure interface. In: *Canadian Geotechnical Journal*, 53(7).

Appendix A

Clay types

TABLE A.1: Index properties of some saturated clay types in literature.

Clay type	e_0	w [%]	LL	PI	λ	Main minerals	σ_3 [kPa]	Reference
Remoulded Illite	0.90	34	94	62	0.39	Illite	196	Campanella & Mitchell (1968)
Pacific Spectite	3.70	138	186	109	0.52	Smectite Illite	98	Houston et al. (1985)
Illite	2.90	111	88	47	0.43	Quartz Illite	98	=
Illite	=	=	=	=	=	=	29	=
Bangkok	2.50	93	103	60	0.46	Smectite Kaolinite	200	Abuel-Naga et al. (2007)
Bangkok	=	=	=	=	=	Mica	300	=
Bangkok	=	=	=	=	=	Mont-morillonite	400	=
Todi	0.89	40	52	30	0.1	Illite Kaolinite Calcite Quartz	196	Burghignoli et al. (2000)
Fiumicino	0.81	30	55	32	0.09	Not reported	147	=
Newfield	0.50	18	25	11	0.09	Quartz Chlorite Mica	275	=

Appendix B

ImageJ macro

```
run("Image Sequence...",
"open=C:/CT/1_Cold/0Start.tif increment=1 convert sort");
rename("ImageSeq1");
selectWindow("ImageSeq1");

run("Reverse");
run("Rotate...", "angle=−3 grid=1
interpolation=Bilinear stack");

run("Find Edges", "stack");
setAutoThreshold("Intermodes");
//run("Threshold...");
setOption("BlackBackground", false);
run("Convert to Mask",
"method=Intermodes background=Light calculate");

//setTool("polygon");
makePolygon(571,708,607,671,652,615,695,521,710,
427,704,333,637,190,595,141,520,91,286,67,150,100,
76,143,18,227,1,293,13,552,53,646,95,688,143,709,
324,706,435,705);
setBackgroundColor(0, 0, 0);
run("Clear Outside", "stack");

run("3D Viewer");
call("ij3d.ImageJ3DViewer.setCoordinateSystem", "false");
call("ij3d.ImageJ3DViewer.add", "ImageSeq1", "None",
"ImageSeq1", "0", "true", "true", "true", "2", "0");
```

Appendix C

Triaxial data processing

A simple flowchart showing the step wise procedure from raw data to plotting is shown below:

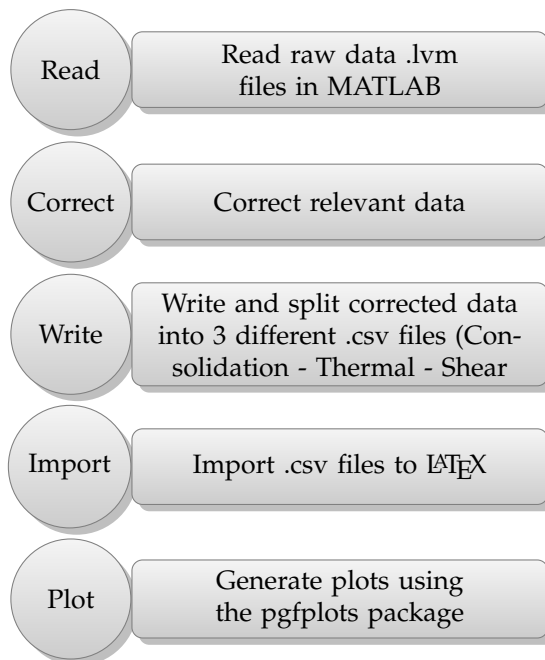| Read | Read raw data .lvm files in MATLAB |
Correct	Correct relevant data
Write	Write and split corrected data into 3 different .csv files (Consolidation - Thermal - Shear
Import	Import .csv files to LaTeX
Plot	Generate plots using the pgfplots package

FIGURE C.1: A simple flowchart showing the data required data processing for creating plots from the triaxial test raw data.

Appendix D

Thermal strain calculation

The Campanella & Mitchell (1968) relationship:

$$\varepsilon_{\mathrm{v}}{}^{\mathrm{T}} = \frac{\Delta V_{\mathrm{corr}} - (\alpha_w V_w + \alpha_s V_s)\Delta T}{V_0} \tag{D.1}$$

Constants:

- $a_w = 20.7 \cdot 10^{-5}$, from literature review (Li, 2019)
- $a_s = 3 \cdot 10^{-5}$, from literature review (Li, 2019)
- $V_s = 0.61$, from index testing
- $V_w = 0.39$, from index testing

Specimen A1:

$$\varepsilon_{\mathrm{v}}{}^{\mathrm{T}} = \frac{(1.5 - 0) - (20.7 \cdot 10^{-5} \cdot 0.39 + 3 \cdot 10^{-5} \cdot 0.61) \cdot (45 - 23)}{229.9} = \underline{\underline{0.6}} \tag{D.2}$$

Specimen A2:

$$\varepsilon_{\mathrm{v}}{}^{\mathrm{T}} = \frac{(1.4 - 0) - (20.7 \cdot 10^{-5} \cdot 0.39 + 3 \cdot 10^{-5} \cdot 0.61) \cdot (45 - 23)}{231.0} = \underline{\underline{0.6}} \tag{D.3}$$

Specimen A3:

$$\varepsilon_{\mathrm{v}}{}^{\mathrm{T}} = \frac{(1.6 - 0) - (20.7 \cdot 10^{-5} \cdot 0.39 + 3 \cdot 10^{-5} \cdot 0.61) \cdot (45 - 23)}{231.1} = \underline{\underline{0.7}} \tag{D.4}$$